Electrostatically Self-Assembled Nanoparticles Based on Biomolecules

DISSERTATION

Zur Erlangung des Grades

"Doktor der Naturwissenschaften"

am Fachbereich Chemie, Pharmazie und Geowissenschaften

der Johannes Gutenberg-Universität Mainz

vorgelegt von

M.Sc. **Li Yi**

Born in Nanjing, P. R. China

Mainz, 2009

Content

Chapter 1. Introduction and Motivation 1

Chapter 2. Background 5

2.1 Association of DNA with Counterions 5

2.2 Association of Oligolysine/Polylysine with DNA 8

2.3 Diffusion Behavior of Polyelectrolytes 10

Chapter 3. Characterization Methods 12

3.1 Light Scattering 12

3.1.1 Static Light Scattering 13

3.1.2 Dynamic Light Scattering 17

3.2 Atomic Force Microscopy 21

3.3 Gel Electrophoresis 25

3.4 Zeta Potential 27

Chapter 4. Association of DNA with Organic Counterions 29

4.1 Introduction 29

4.2 Characterization of DNA 31

4.3 Association of DNA with Divalent Counterions 44

4.4 Association of DNA with Tetravalent Counterions 63

4.4.1 Association of DNA with $C6T^{4+}$ 63

4.4.2 Association of DNA with PSPDI 69

4.5 Conclusions 88

Chapter 5. Association of Sodium Polystyrene Sulfonate with Oligolysines…… 91

5.1 Introduction 91
5.2 Characterization of the Components 93
5.3 Association of NaPSS with Trilysine 97
5.4 Association of NaPSS with Different Oligolysines 118
5.4.1 Association of NaPSS with Dilysine 118
5.4.2 Association of NaPSS with Tetralysine 119
5.4.3 Association of NaPSS with Pentalysine 121
5.5 Conclusions 126

Chapter 6. Polyelectrolyte Assemblies in AFM 128
6.1 Introduction 128
6.2 Influence of Surface Charge 130
6.3 Influence of Preparation Method 135
6.4 Influence of Added Salt 136
6.5 Conclusion 138

Chapter 7. Summary 140

Chapter 8. Experimental Section 145

List of Abbreviations 151

References and Notes 153

CHAPTER 1. INTRODUCTION AND MOTIVATION

Self-assembly is driven by nonconvalent interactions and the association of subunits leads to supramolecular oligomers, aggregates or materials.[1,2,3,4] Compared to synthetic macromolecules which contain covalent bonds, the aggregates formed by self-assembly exhibit two major advantages:[5] (1) it is much simpler to produce supramolecular structures and adjust physical, chemical and/or biological properties. (2) The noncovalent interactions in the assembly give the possibility of rearrangement of the components upon external stimuli, which may lead to further applications of the assemblies. The bilayer structure of the cell membrane and the double helix structure of the DNA are perfect examples of supramolecular structures formed by self-assembly in nature. Thereby, inspired from that, it has attracted tremendous attention and interest to fundamentally understand and practically design self-assembled nanoparticles and supramolecular structures.

The noncovalent interactions in the self-assembly can involve hydrophobic interaction, hydrogen bonding, metal coordination, electrostatic interaction or a combination of these. The hydrogen bond represents a bridge between a hydrogen atom which is covalently bound to an electronegative atom like oxygen or fluorine and an electronegative atom with at least one lone pair of electrons. The “hydrophobic effect” causes the formation of clusters of hydrophobic or amphiphilic molecules in aqueous solution. It releases water molecules from the hydrophobic molecule surfaces into the bulk solvent. This yields an entropy gain, which is the origin of the hydrophobic interaction in water. The electrostatic interaction is raised from the force between two charged molecules (either

repulsive or attractive), which is also known as Coulomb force. While the hydrophobic effect is the origin for the formation of classical micelles[6,7] and the assembly of many other amphiphilic molecules,[8, 9,10,11,12] also hydrogen bonding and metal coordination lead to supramolecular materials.[13,14,15] Assemblies and materials with supramolecular architectures based on the mentioned interaction forces can combine certain properties of two different components or exhibit special properties and thus open the possibility for numerous applications that cannot be achieved by the individual components. The formation of supramolecular structures through self-assembly can be either kinetically or thermodynamically controlled.[16,17] In a kinetically controlled aggregate, a frozen irreversible structure is obtained and usually dependents on the way of preparation. For the complexes formed thermodynamically, the resulting structure is in thermodynamic equilibrium due to the possible rearrangement of the building blocks. While it is of fundamental interest how the structure found is controlled, both structural types may be of interest for certain properties and functions.

Polyelectrolytes represent a promising candidate for self-assembly because they exhibit both polymeric and electrolytic properties. A self-assembly process involving polyelectrolytes is normally based on electrostatic interaction due to the existence of charges when dissolving polyelectrolyte in the solution. The assembly of polyelectrolytes with oppositely charged components is also specified as “electrostatic self-assembly”.[18,19,20,21,22,23,24] Various building blocks have been combined with polyelectrolytes: oppositely charged polyelectrolytes, metal ions, surfactants or small organic counterions with certain geometry. In the polyelectrolyte-polyelectrolyte complexes, resulting structures can be described predominately by one of two models: the ladderlike structure or the scrambled egg structure.[25] These however usually represent aggregates with a broad size distribution and little structural control. Depending on composition and concentration, also precipitation occurs. A way to organize polyelectrolyte-polyelectrolyte systems is the layer-by-layer deposition, yielding films, capsules

or solid materials.[26,27,28] A similar scenario as for inter-polyelectrolye complexes exists when combing polyelectrolytes with multivalent metal counterions. Due to the large conformational freedom of the polyelectrolyte and the small unstructured counterion, aggregates usually do not exhibit a certain structure. At some amount of multivalent counterions, complexes also precipitate.[29,30,31,32] In contrast, polyelectrolyte-surfactant complexes usually generate solid structured materials. The assembly structure is more defined and versatile than that of polyelectrolyte-polyelectrolyte complexes mainly due to the secondary hydrophobic interaction in-between surfactant tails, which can direct the association into more ordered nanostructures.[33,34] However, neither of the above states can yield aggregates with well-defined supramolecular structures that are stable in solution. A recent branch of self-assembled polyelectrolyte systems involves small organic counterions with certain structural properties. The geometry of the counterion together with π-π interaction between the counterions gives the possibility to control the resulting structures. Recent studies on the association of various polyelectrolytes and multivalent stiff organic counterions (especially dye molecules) demonstrated this concept and yielded water soluble aggregates with well-defined supramolecular structures. [22,35,36]

The interest of this study also focuses on polyelectrolyte-organic counterion assemblies. In particular, the goal of this study is to investigate whether defined supramolecular structures in solution can be built in an electrostatic self-assembly process without secondary π-π interaction. As in previous studies, the importance of a certain geometry of at least one of the components was shown. Therefore, in one system, it is investigated whether only electrostatics and geometric factors can direct the structure formation. In a second system, electrostatic interaction is combined with the possibility for mutual hydrogen bonding in-between counterions. This is in difference to the system allowing for mutual π-π interaction of the counterions investigated so far[37,38] and thus has the potential to establish the concept of electrostatic self-assembly for the formation of supramolecular assemblies in solution on a much broader basis.

DNA is used as the polyelectrolyte in the one model system. Counterions of different valence and stiffness are applied. The goal is to relate the results to the recent findings on electrostatic self-assembly on the one hand and to numerous, but less systematic studies on DNA aggregation on the other hand. As it was postulated previously that it is the charged nature that stabilizes electrostatically self-assembled complexes in solution,[24,39] the hypothesis of this study is that such stabilized charge can also be caused by geometric effects during the electrostatic association (with no π-π stacking present). In the second system, a flexible common polyelectrolyte (NaPSS) is combined with counterions that bear the possibility for mutual hydrogen bonding. The concept is in analogy to the association of a flexible polyelectrolyte with π-stacking counterions,[40] but would open the approach for a variety of further building blocks, potentially with functionalities. Usually, few hydrogen bonds are not sufficient to provide stability of supramolecular structures in solution. Many such bonds are present in biologic assemblies, while artificial systems normally are investigated in organic solvent.[41,42] To provide a fundamental initial study on electrostatic self-assembly with hydrogen bonding counterions, a set of oligolysine with different chain length is applied as model system here. The influencing factors, such as the characteristics of the polyelectrolytes (conformation and molecular weight) and counterions (valency and geometry) and the mixing conditions (charge ratio, polymer concentration), will be investigated in details. Assemblies will be analyzed by dynamic and static light scattering, atomic force microscopy, UV-Vis spectroscopy, analytical ultracentrifugation, gel electrophoresis, ATR-IR spectroscopy and zeta potential measurements.

CHAPTER 2. BACKGROUND

2.1 Association of DNA with Counterions

Deoxyribonucleic acid (DNA) is well known as the carrier of genetic information in all living organisms. In its unpackaged form, DNA is described as a wormlike chain with a persistence length of approximately 50 nm.[43] However, when DNA is packed inside viruses and cells, it is highly concentrated into a configuration where helices are approximately parallel to each other with a surface-to-surface separation of roughly 0.5 nm. The tightly packaged state typically is only 10^{-4} ~ 10^{-6} of the volume of the unpackaged DNA coil.[44] It has been suggested that many bacteriophages use multivalent cations pack their DNA.[45,46,47] Therefore, association of DNA with different multivalent counterions has attracted lot of attention, both with the aim to understand the mechanism of DNA packing inside viruses and cells and for possible applications with regard to interesting supramoecular structures.[48,49,50]

Assemblies of DNA with multivalent ions were first observed with the naturally occurring polyamine spermidine: a well-defined toroid structure was observed in transmission electron microscopy.[44] Later toroidal and rodlike structures were also found for other counterions, for example spermidine derivatives,[51,52] spermine,[53] hexamine cobalt[54] and chitosan.[55] Although rodlike and toroid structures are well known, the formation process is not completely understood yet. Fang et al. reported the formation of flower-like and disc-like DNA aggregates with spermidine and suggested they represent intermediate stages of complexes on the pathway to the final rod or toroid structure, however, this could not be proven.[56]

In difference to higher multivalent ions, it was predicted that divalent counterions cannot induce aggregation of DNA according to Manning's counterion condensation theory.[57,58] As a consequence, the studies of DNA association with divalent counterions attract less attention. Kelly et al. demonstrated the different interaction behavior of divalent ruthenium coordination compounds with DNA.[59] They found that depending on the molecular structure, $Ru(phen)_3^{2+}$ (phen = 1,10-phenanthroline) binds intercalatively to DNA, while $Ru(bipy)_3^{2+}$ (bipy = 2,2'-bipyridyl) and $Ru(terpy)_3^{2+}$ (terpy = 2,2',2"-terpyridyl) binds to DNA externally. Yoshikawa et al. presented a coil-globule transition of DNA molecules complexed with diaminoalkanes.[60,61] The group of Baro investigated the topographic changes of DNA induced by divalent metal ions.[62] The AFM measurements revealed fully reversible DNA condensates mediated by Co^{2+} and Ni^{2+}, where the DNA molecules showed significant reduction in length and increment in height. Nevertheless, there was no study on the formation of nanostructure by association of DNA with divalent structural organic counterions.

A further branch of intensively investigated DNA-probe systems are DNA-dye complexes, with the chromophores being porphyrin,[63,64] acridine orange[65,66] and many others. These are of particular interest as they can be used for DNA detection. Krauß et al. investigated the morphology of DNA complexes induced by a perylene bisimid with 16 positive charges and observed flower-like aggregates by atomic force microscopy.[67] However, most of the studies of this subject focused on the spectroscopic properties of the DNA-dye aggregates. While it is evident that the assembly of DNA with different small ionic molecules can result in different structures and a variety of results have been reported, it is difficult to relate them.

Usually three main binding modes in the interaction of small molecules with the DNA double helix are distinguished.[68,69,70,71] They are external binding, groove binding and intercalation (Figure 2.1.1). In the external binding, the counterion interacts with the phosphate group via electrostatic interaction and stays outside

the DNA strand at its surface. In the groove binding, the probe molecule is either in the deep major groove or the shallow minor groove of the DNA helix, interacting with nucleic acid bases due to hydrophobicity and/or with the phosphate group via hydrogen bonds. In the intercalation mode, the molecule causes the double helix to unwind and slides between the base pairs to interact with them by π-π stacking. A planar structure of the probe molecule is a requirement for this binding mode. It needs to be emphasized that in the intercalation the DNA double helix structure is somewhat distorted. The selection of counterions for this work is limited to the non-intercalation ions in order to study a possible connection of multiple undistorted DNA molecules into supramolecular structures.

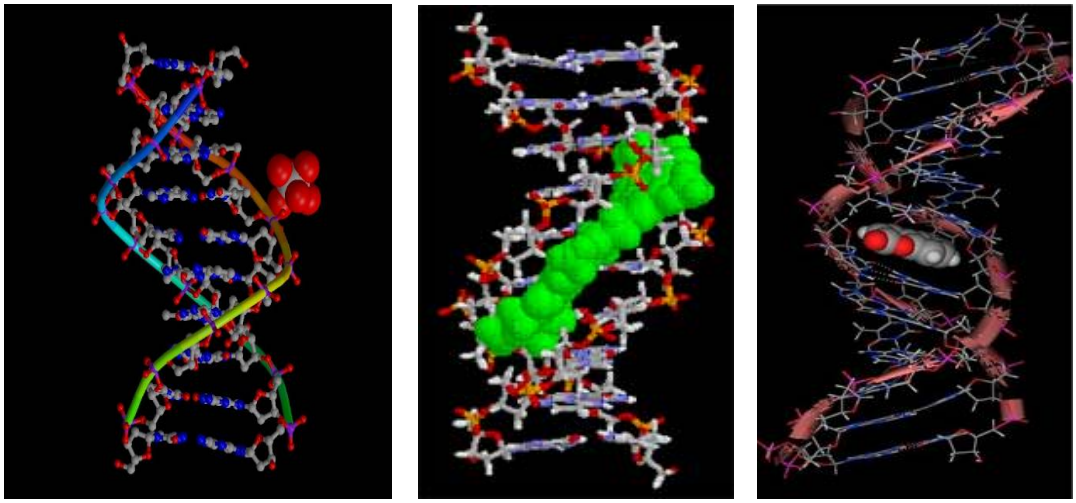

Figure 2.1.1. Illustration of different binding modes with DNA: external binding (left),[72] groove binding (middle)[73] and intercalation (right)[74]

2.2 Association of Oligolysine/Polylysine with DNA

Proteins are one of the most important type of biological macromolecules and essential parts of the organism. They play a crucial role in every process within a cell, e.g. catalyzing biochemical reactions, metabolic control, mechanical functions in the muscle, cell signaling. In the most important gene replication process, the expression of genetic information involves the interaction of regulatory proteins and of RNA polymerase with specific and nonspecific site on DNA.[75] Therefore, the complexation mechanism of protein to DNA is of great interest, not only for revealing the biological process, but also for the development of nonviral gene delivery system.[76,77,78]

Among various peptides, oligolysine and polylysine are the most commonly used molecules for studying the association properties with DNA as a model system due to their positive charges and relatively simple molecular structures. The morphology of the complexes formed with polylysine has been extensively investigated.[79,80,81] The polyelectrolytes involved in those studies varied from biopolymers to synthetic polyelectrolytes and the size of the polylysine was in a broad range. For example, Liu et al. described a structure transition of complexes induced by polylysine (repeat unit n = 256) and plasmid DNA, from spheres to rods or toroids, under various salt concentrations.[82] Müller et al. presented solid particles produced by high molecular weight polylysine (repeat unit n = 1688) with either poly(maleic acid-*co*-α-propylene) or poly(maleic acid-*co*-α-methyl-styrene).[83,84] The aggregates of polylysine and poly(maleic acid-*co*-α-methyl-styrene) exhibited spherical shape on a Si wafer, while that with poly(maleic acid-*co*-α-propylene) showed needlelike structure.

Compared to polylysine, investigations on the complexation of oligolysine so far has been limited to DNA and its analogs as the only polyelectrolyte. Early studies of DNA/oligolysine interaction were mainly in the area of binding energies. Latt et

al. demonstrated the binding behavior of oligolysine (n = 3 ~ 8) to polynucleotides by equilibrium dialysis measurements.[85] The results revealed that both the total binding energy and the difference between the binding energies to poly (I + C) and poly (A + U) increase linearly with oligolysine chain length. The group of Crescenzi reported the thermodynamic characterization of DNA/trilysine system.[86] Calorimetric data suggested that the formation of DNA/trilysine complex is driven by entropy gain, which might arise from a loss of water from the hydration sheaths of interacting species. Although there have been many studies on the DNA/oligolysine system, only few of them focused on the structure of the complexes and contradictory results were received with respect to the early studies. Wadhwa et al. attempted to build DNA assemblies with short peptide molecules, which contained various lengths of lysine segment at the end.[87] Their results showed that the alkylated peptide chain with trilysine unit (Cys-Trp-$(Lys)_3$) failed to bind to DNA, while the other alkylated peptides with longer lysine segments (Cys-Trp-$(Lys)_8$, Cys-Trp-$(Lys)_{13}$ and Cys-Trp-$(Lys)_{18}$) could induce condensation of DNA into globular structure. Similar results were obtained by Thomas et al.. In their study, oligolysine with repeat unit n = 4 or 5 could form aggregates with λ-DNA and resulted in mostly spherical and very few rodlike structure. In contrast, trilysine did not provoke DNA condensation even up to very high concentration.[88] Thus, it is of interest to test the concepts of electrostatic self-assembly of oligolysine in combination with normal synthetic polyelectrolytes and investigate the influence of the length of the oligolysine on the association behavior, especially for the very short oligolysine molecules i.e. repeat unit n = 2 ~ 5.

2.3 Diffusion Behavior of Polyelectrolytes

Polyelectrolytes exhibit more complicated dynamic behavior in solution than uncharged polymers.[25] In dynamic light scattering, the electric field autocorrelation function of a polyelectrolyte solution normally yields a bimodal distribution in the absence of low molecular mass salt. The two characteristic decay times obtained from the bimodal distribution can be 2 or 3 orders of magnitudes apart from each other, which are known as fast mode and slow mode. The fast mode is explained to represent the coupled diffusion of polyelectrolytes and counterions. The slow mode represents the formation of large multichain "domains". The origin of the slow mode is not completely understood yet. However, it is a consequence of electrostatic interactions between polyelectrolyte molecules and counterions.

Polyelectrolyte effects can be eliminated by screening the charges with sufficient amount of added low molecular mass salt, such as NaCl.[89,90,91,92,93] The typical diffusion behavior of polyelectrolyte with additional salt is illustrated in Figure 2.3.1. Here the characteristic parameter λ is defined as:

$$\lambda \propto \frac{c_p}{c_s} \qquad [2.1]$$

where c_p and c_s represents the molar concentration of polyelectrolyte and salt, respectively.

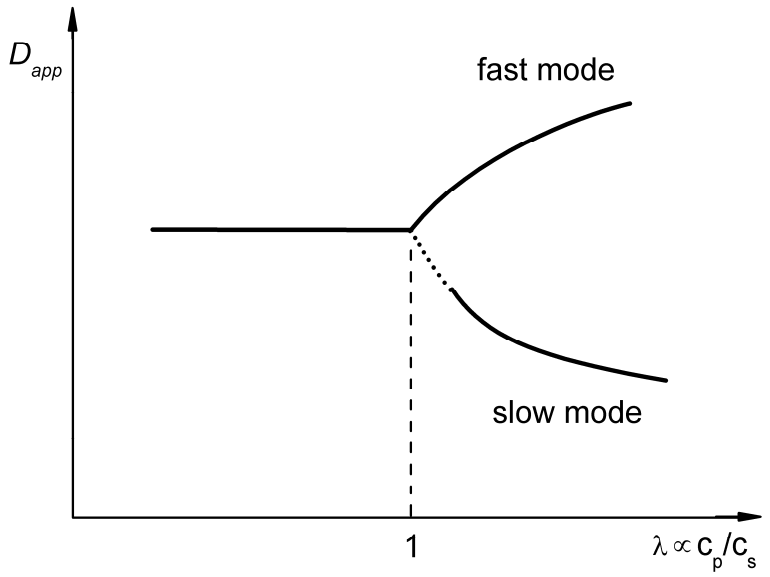

Figure 2.3.1. Illustration of polyelectrolyte effects in presence of salt

It is observed from the plot that the polyelectrolyte effects exist when $\lambda >> 1$. The polyelectrolyte solution always exhibits bimodal behavior in this region. In the more diluted regime where $\lambda << 1$, only a monomodal process is observed. The distribution in this area reflects the diffusion behavior of single polyelectrolyte molecule. In the transition regime $\lambda \approx 1$, the two modes merge into one distribution. Increasing the salt concentration c_s or decreasing the polyelectrolyte concentration c_p is able to achieve $\lambda << 1$ and eliminate the polyelectrolyte effects.

CHAPTER 3. CHARACTERIZATION METHODS

3.1 Light Scattering[94,95,96,97,98]

Interaction of electromagnetic radiation with matter results in scattering of this radiation. If the incident radiation has a wavelength in the range of light, the scattering phenomenon is referred to as light scattering. Light scattering is one of the most universal and versatile absolute method for molar mass determination of macromolecules. Moreover, light scattering can yield information on second viral coefficient, radius of gyration, diffusion coefficient and particle shape. There are two different methods in the light scattering techniques, which are known as static light scattering (SLS) and dynamic light scattering (DLS). In dynamic light scattering, the scattering intensity as a function of time is recorded. In static light scattering, the angular dependent average scattering intensity is measured.

Both dynamic and static light scattering require essentially the same experimental setup, which is shown in Figure 3.1.1. A monochromatic laser beam is designed for measurements. The primary beam with most of the intensity passes through the sample cell without hindering. The light scattered in a certain angle θ is collected by a detector, e.g. a photodiode. The detector is fixed on a goniometer which enables measurements in an angular range of about 30° to 150°. In DLS, the signals of the scattered intensity are sent to a correlator for correlation.

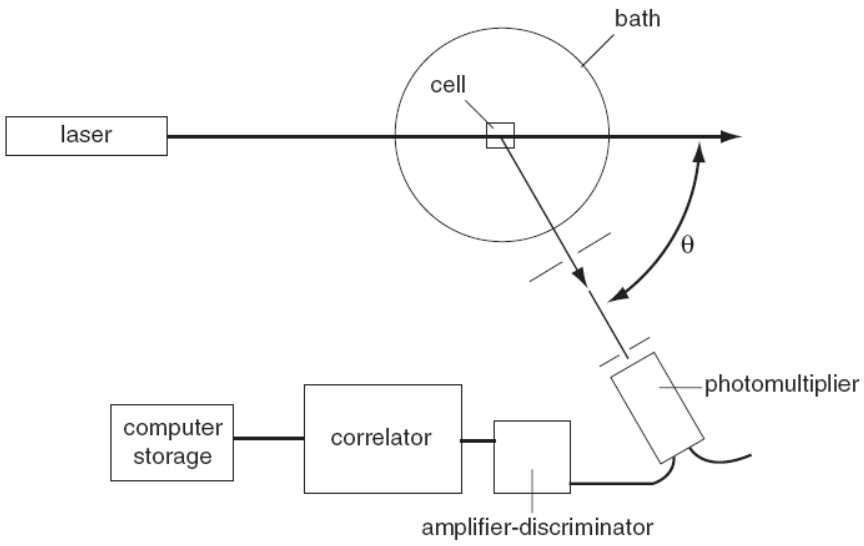

Figure 3.1.1. Schematic illustration of light scattering set-up[99]

3.1.1 Static Light Scattering

When light hits a particle, a dipole is induced as a consequence of interaction of incident electric field and charge distribution of the particle. This dipole, so called Hertz dipole, oscillates and itself irradiates electromagnetic waves, which appears as scattered radiation. The induced dipole moment $\vec{p}$ is given by:

$$\vec{p} = \alpha \cdot \vec{E}_i \qquad [3.1]$$

where $\vec{E}_i$ is the strength of the incoming electric field and α is the polarizability of the particle. The angular dependence of the electric field strength irradiated by a Hertz dipole can be calculated from the Maxwell equations:

$$E_s = \frac{1}{c^2}\frac{\partial^2 p}{\partial t^2}\frac{\sin\phi}{r} \qquad [3.2]$$

where c is the velocity of light, p is the dipole moment, r is the distance between the oscillating dipole and the observer, while ϕ is the angle between the dipole

axis and the direction from dipole center to the observer. The amplitude of an electric field of the scattered electromagnetic wave E_s and the relationship between scattering intensity I and the electric field E are given by:

$$E_s = E_0 \cos(\omega t - kx) \quad [3.3]$$

$$I_0 = |E_0|^2 \quad [3.4]$$

where ω is the angular frequency, x is the propagation direction, k is the magnitude of the wave vector (wave number, $k = \frac{2\pi}{\lambda}$). Combining the formulae above and with $\frac{\omega^4}{c^4} = \left(\frac{2\pi}{\lambda}\right)^4$, the scattering intensity contributed from multiple molecules N can be written as:

$$\frac{I_s}{I_0} = N \frac{\sin^2(\phi)}{r^2} \frac{16\pi^4}{\lambda^4} \alpha^2 \quad [3.5]$$

According to the “fluctuation theory”, light scattering arises from the fluctuation of polarizability α of the scattering medium. The fluctuation is caused by both density and concentration fluctuations and thus the polarizability is given by:

$$\alpha = \alpha_0 + \delta\alpha \quad \text{with} \quad \delta\alpha = \left(\frac{\partial\alpha}{\partial\rho}\right)_{p,T} \delta\rho + \left(\frac{\partial\alpha}{\partial c}\right)_{p,T} \delta c \quad [3.6]$$

where α_0 is the average polarizability over time and equals to zero since positive and negative deviation from the average have the same probability. $\delta\alpha$ is the polarizability due to local fluctuations. In experiments with macromolecules, the solvent scattering intensity is always subtracted from the solution scattering intensity. Therefore, the contribution of the density fluctuations is essentially eliminated, only the polarizability fluctuation arisen from the concentration fluctuations is considered:

$$\left\langle \delta\alpha^2 \right\rangle = \left(\frac{\partial\alpha}{\partial c}\right)^2_{p,T} \left\langle (\delta c)^2 \right\rangle \quad [3.7]$$

The change in polarizability can be replaced by the change in refractive index n and chemical potential, yielding the fundamental equation for light scattering of small particles ($R < \lambda/20$):

$$\frac{Kc_2}{R(\theta)} = \frac{1}{M_2} + 2A_2c_2 + 3A_3c_2^2 + \ldots$$

With $R(\theta) = \left(\frac{I_{solution} - I_{solvent}}{I_0}\right) \cdot \frac{r^2}{V \sin^2(\theta)}$ and $K = \frac{4\pi^2 n_0^{\,2}}{N_A \lambda_0^{\,4}} \left(\frac{\partial n}{\partial c}\right)^2$ [3.8]

where $R(\theta)$ is called Rayleigh Ratio and K is known as optical constant. n_0 denotes the refractive index of the medium, λ_0 is the wavelength of the primary beam in vacuum and N_A is the Avogadro constant. It needs to be noted that equation 3.8 is valid for small particles (point scatters). For larger particles ($\lambda/20 < R < \lambda$) where multiple scattering centers are within one particle, the scattering equation becomes:

$$R(\theta) = Kc_2 \left(\frac{1}{M_w} + 2A_2c_2 + 3A_3c_2^2 + \ldots\right)^{-1} \cdot P(q) \qquad [3.9]$$

where $P(q)$ is the form factor. It relates to the shape of the particles. For small particles $P(q)$ = 1. The form factor is related to the radius of gyration R_G of a small particle by Guinier approximation for qR_G << 1:

$$P(q) = 1 - \frac{1}{3} q^2 \left\langle R_G^2 \right\rangle \qquad [3.10]$$

here q is defined as scattering vector, which is illustrated in Figure 3.1.1.1.

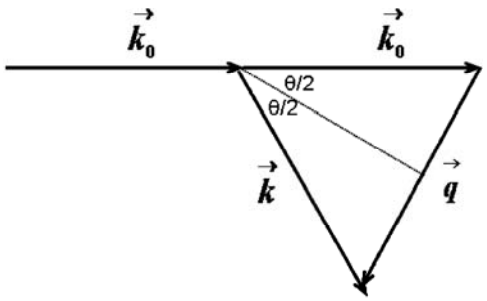

$$|\vec{q}| = \left|\vec{k} - \vec{k}_0\right| = \frac{4\pi n}{\lambda} \sin\left(\frac{\theta}{2}\right) \qquad [3.11]$$

Figure 3.1.1.1. Schematic illustration of scattering vector

In solution, both intramolecular and intermolecular interference are possible. The form factor $P(q)$ describes the scattering intensity resulting from intramolecular correlations, while the scattering intensity from intermolecular interference is called the structure factor $S(q)$. They are defined as:

$$P(q) = \frac{1}{z^2} \sum_{i=1}^{z} \sum_{j=1}^{z} \left\langle \exp(-i\vec{q}\vec{r}_{ij} \right\rangle_{or,r} \quad [3.12]$$

$$S(q) = \frac{1}{z^2} \sum_{i=1}^{z} \sum_{j=1}^{z} \left\langle \exp(-i\vec{q}\vec{r}_{ij} \right\rangle_{or,r} \quad [3.13]$$

The total scattering intensity is the sum of both correlations

$$\frac{I(q)}{Nb^2} = z^2 P(q) + Nz^2 S(q) \quad [3.14]$$

where N is the number of molecules in a system, z is the number of scattering centers and b is the contrast factor. For dilute solution, which means $N \rightarrow 0$, the second term becomes zero and the total expression yields the particle form factor only. However, it is not possible to calculate the particle shape from the measured scattering intensity due to the fact that the phase information is lost during the transferring of scattering intensity into scattering amplitude (square root). This is known as the “phase problem” in scattering.

Combination of equations 3.9 and 3.10 gives the Zimm equation:

$$\frac{Kc_2}{R(\theta)} = \frac{1}{M_w}\left(1 + \frac{1}{3} q^2 \left\langle R_G^2 \right\rangle\right) + 2A_2 c_2 + \ldots \quad [3.15]$$

plotting $\frac{Kc_2}{R(\theta)}$ versus $(q^2 + kc_2)$ yields so-called Zimm plot (k is a suitable constant). In this plot, angular dependent light scattering data can be analyzed by extrapolating $\frac{Kc_2}{R(\theta)}$ to zero concentration and zero scattering vector (Figure 3.1.1.2). The y-intercept yields the inverse weight average molecular

mass ($1/M_w$) of the dissolved particles. From the slope of the concentration dependence, the second virial coefficient A_2 is obtained and the slope of the angular dependence generates the radius of gyration R_G.

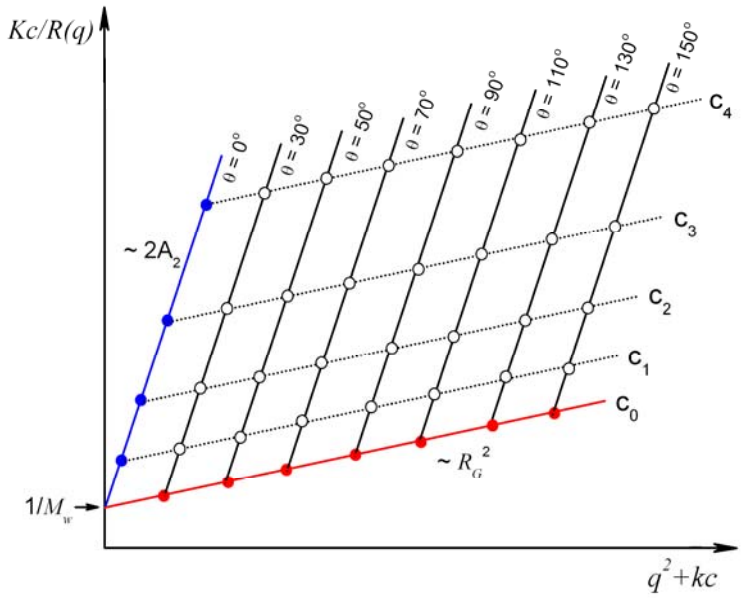

Figure 3.1.1.2. Typical Zimm plot in static light scattering

3.1.2 Dynamic Light Scattering

In dynamic light scattering the scattered intensity is detected as a function of time and results in time-dependent fluctuations which are mostly due to the concentration fluctuations. Two different types of motion mainly contribute to the scattered signal: one is the translational motion of the centre of mass of the individual particles, which is known as Brownian motion. The other one is the internal motion of segments with respect to their centers of mass. Both types can be distinguished in experiments by the angular dependence. The internal motion is independent of the scattering angle. The intensity fluctuations are converted into a time correlation function of the scattering intensity:

$$\langle I(q,0)I(q,\tau)\rangle = \lim_{T\to\infty}\frac{1}{T}\int_0^T I(q,t)I(q,t+\tau)dt \qquad [3.16]$$

The boundary conditions generate the following results:

$$\lim_{\tau\to 0}\langle I(q,0)I(q,\tau)dt\rangle = \langle I(q)^2\rangle \qquad [3.17]$$

$$\lim_{\tau\to\infty}\langle I(q,0)I(q,\infty)dt\rangle = \langle I(q)\rangle^2 \qquad [3.18]$$

It shows that at τ = 0, these two signals are completely in phase with each other and $\langle I(q)^2\rangle$ is the maximum. As τ increases to large time, the signals get out of phase with each other and the correlation function decay to the minimum value $\langle I(q)\rangle^2$, as demonstrated in Figure 3.1.2.1.

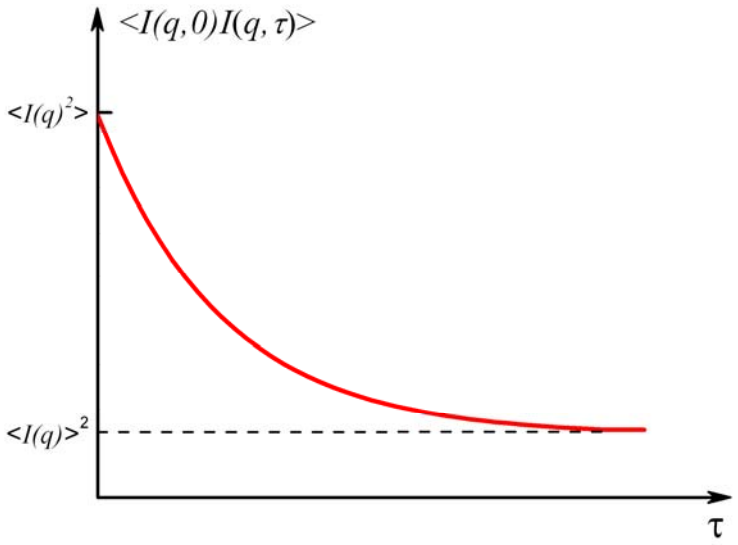

Figure 3.1.2.1. The time correlation function of the scattering intensity

The time autocorrelation function of the scattered intensity $g^2(q,\tau)$ and electric filed $g^1(q,\tau)$ is defined as following:

$$g^2(q,\tau) = \frac{\langle I(q,0)I(q,\tau)\rangle}{\langle I(q)^2\rangle} \qquad [3.19]$$

$$g^1(q,\tau) = \frac{\langle E_S(q,0)E_S(q,\tau)\rangle}{\langle E_S(q)^2\rangle} \qquad [3.20]$$

The autocorrelation function of the scattered intensity and electric filed can be converted via so-called Siegert relation:

$$g^2(q,\tau) = B(1 + \beta\left|g^1(q,\tau)\right|^2) \quad [3.21]$$

where B is the experimentally determined baseline and β is an efficiency factor. For monodisperse small particles the correlation function decreases as single-exponential function:

$$g^1(\tau) = A_0 \exp(-q^2 D\tau) \quad [3.22]$$

here A_0 is the signal-to-noise ratio and depends on the optical setup of the experiment. For polydisperse small particles $g^1(q,\tau)$ is given by:

$$g^1(q,\tau) = A_0\left(\frac{\sum m_i M_i \exp(-q^2 D_i\tau)}{\sum m_i M_i}\right) \quad [3.23]$$

The electric filed autocorrelation function can also be converted to the distribution of inverse relaxation times by the inverse Laplace Transformation:

$$g^1(q,\tau) = \int_0^\infty A(\Gamma)exp(-\Gamma\tau)d\Gamma \quad [3.24]$$

$$A(\Gamma) = \frac{1}{2\pi}\int_0^\infty g^1(q,\tau)exp(-\Gamma t)dt \quad [3.25]$$

with the relaxation rate (inverse relaxation time) Γ given by the relationship:

$$\Gamma = \frac{1}{\tau} = q^2 D \quad [3.26]$$

The inverse Laplace Transformation has to be performed via a least square procedure under regularization, which can be done by programs such as CONTIN or ORT. Alternatively, one can also express the electric field autocorrelation function as a series of cumulants:

$$ln\, g^1(q,\tau) = \sum_{n=1}^{\infty} \frac{\Gamma_n}{n!}\tau^n = -\Gamma\tau + \frac{\mu_2}{2}\Gamma^2\tau^2 - \frac{\mu_3}{6}\Gamma^3\tau^3 + \ldots \quad [3.27]$$

An apparent diffusion coefficient can be defined from the initial slope:

$$D_{app}(q) = \frac{\Gamma}{q^2} \quad [3.28]$$

the higher cumulants μ_2 and μ_3 represent a qualitative measure of the polydispersity when the effect of internal modes can be neglected. Furthermore, the cumulant fit is a good approach only in the case of presence of one narrow decay time distribution.

Finally the diffusion coefficient can be converted into the hydrodynamic radius R_H via the Stokes-Einstein relationship:

$$D = \frac{kT}{6\pi\eta R_H} \quad [3.29]$$

Although this function holds for spherical particle, commonly it is applied for any sample yielding the hydrodynamic radius that represents the radius of a friction equivalent sphere. Furthermore, considering interparticle interactions, polydispersity and internal modes, the diffusion coefficient shows both concentration and q dependency:

$$D_{app}(q) = D_0(1 + CR_G{}^2q^2) + k_Dc + \ldots \quad [3.30]$$

where D_0 is the diffusion coefficient extrapolating to scattering vector q = 0; C represents a characteristic constant for various particle structures; k_D is related to second virial coefficient. This equation is formally in analogy to function 3.15, the Zimm equation for the static scattering intensity. It has been suggested that equation 3.30 can be plotted as a “dynamic Zimm plot”, which yields D_0, k_D and A_2 by extrapolating $q^2 \rightarrow 0$ and $c \rightarrow 0$.

3.2 Atomic Force Microscopy[100,101,102]

The basic principle of AFM is to take advantage of the interactions between a sharp tip and a sample when the tip is placed very close to the sample. Compared to the traditional TEM technique, the advantage of AFM is that no staining is required for the samples, which may bring artifacts in TEM measurements. In addition to the conventional function of “imaging”, AFM also offers the possibility to characterize the surface mechanical properties and the surface forces of the sample on the nanometer scale.

The essential instrumental components in an atomic force microscope are: a sharp tip fixed on a cantilever spring, a cantilever deflection sensor, an electronic feedback system, a data display and a mechanical scanning system. The general setup of an atomic force microscope is illustrated in Figure 3.2.1. The sample is fixed on a piezoelectric scanner, which can move in three directions. When the tip approaches to the surface and the sample is scanned, the interatomic force between the tip and the sample molecules, either repulsive or attractive, can lead to elastic deformations of the cantilever. The deflection of the cantilever then is captured by an optical detection system, which is consisting of a laser beam and a split photodiode. Finally the deflection detected by the photodiode is converted into an electronic signal and displayed on the monitor.

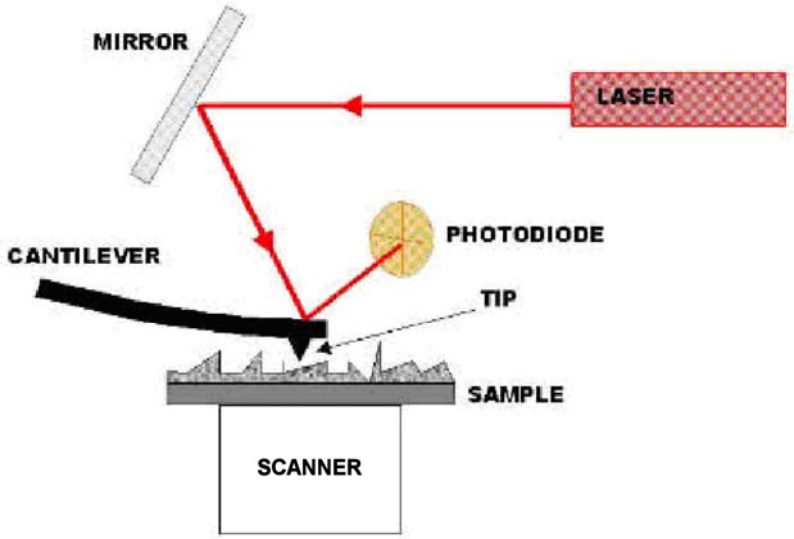

Figure 3.2.1. Schematic illustration of AFM setup[103]

The operation of AFM normally is divided into two groups, the static and the dynamic mode. In the static mode operation (also known as contact mode), the tip is in contact with the sample. The force between the tip and sample (normally repulsive force) is translated into a deflection of the static cantilever. The surface structure can be imaged at “constant height” or at “constant force”. In the static mode, the cantilever should be much softer than the bonds between bulk atoms in the tip and sample. Therefore, the typical spring constant of a cantilever for the static mode is in the range of 0.01 Nm^{-1} to 5 Nm^{-1} with resonance frequency of 5 kHz to 50 kHz.

In the dynamic mode operation (also commonly called non-contact mode), the cantilever is externally oscillated at or close to its fundamental resonance frequency. The oscillation amplitude, phase and resonance frequency are changed by the interactions between the tip and sample. These changes in oscillation with respect to the external reference oscillation provide information about the sample. If the dynamic mode operation is applied at a closer distance range involving repulsive tip-sample interactions, then it is specified as tapping mode AFM.

Two basic modulations are recognized in dynamic mode AFM: amplitude modulation (AM) and frequency modulation (FM). In AM-AFM, the actuator is driven by a fixed amplitude at a fixed frequency. When the tip approaches the sample, the interactions between them cause a change in both the amplitude and the phase of the oscillation of the cantilever, which are proceeded as the feedback signal. The height of the sample is determined according to the changes in the amplitude. The changes in the phase can be used to discriminate different types of materials on the surface. While in FM-AFM, the signal resulted from the interactions between the tip and sample is provide by the changes in the oscillation frequency.

Compared to contact mode AFM, non-contact mode AFM exhibits several advantages. Contact mode imaging is heavily influenced by frictional and adhesive forces. The sample or the tip might be damaged during scanning in the contact mode AFM. Non-contact mode AFM does not suffer such lateral forces, which provides the opportunities to image very soft and fragile samples. Furthermore, the dynamic mode AFM can be performed in very high sensitivity in respect of frequency or amplitude. Thus it is much easier to image sample with atomic resolution in dynamic mode AFM than in static mode.

AFM can be performed in vacuum, air and liquids. A typical setup for liquid AFM measurement is schematically illustrated in Figure 3.2.2. The cantilever is fixed in a small notch on the bottom side of the liquid cell by a gold-coated steel wire clip. A tiny coil spring is mounted on the top of the liquid cell and holds the wire clip against the cantilever. The glass surface of the liquid cell provides a flat interface so that the AFM laser beam may pass into the solution without distortion. The liquid cell, the substrate and a small round shape rubber, which is called O-ring, compose a sealed chamber. The sample solution is then injected into the chamber for measurements. The volume of solution in such setup is normally (30 ~ 50) μL. Compared to AFM in dried state, immobilization of particles on the substrate surface is more important and crucial in liquid AFM measurements.

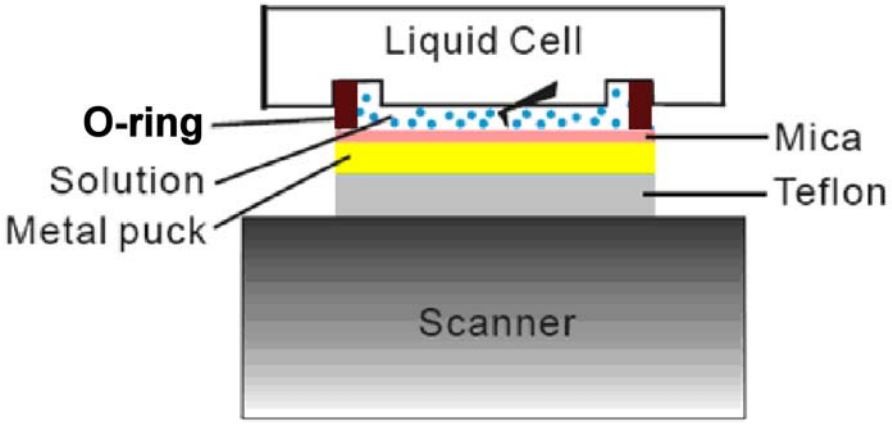

Figure 3.2.2. Schematic illustration of the cross section of a liquid AFM setup[102]

3.3 Gel Electrophoresis[104]

Gel electrophoresis is a technique for the separation of DNA, RNA or protein molecules. A typical set-up for gel electrophoresis is illustrated in Figure 3.3.1. A porous gel matrix is placed in buffer solution and an electric field is applied on the gel. The charged molecules can migrate in the gel due to the electric potential. Based on their charges, molecular mass and/or conformations, those charged molecules exhibit different electrophoretic mobility in the gel. The higher charge to mass ratio, the smaller molecular mass or the more compact structure of the molecule, the faster the molecules migrate in the gel. In this way, gel electrophoresis can be used not only for separating DNA or protein molecules, but also possibly for studying the DNA complexes qualitatively and/or quantitatively.

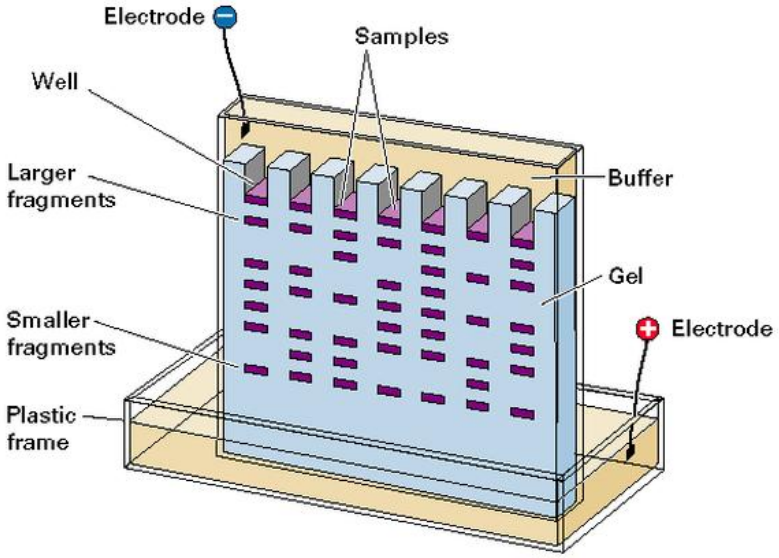

Figure 3.3.1. Schematically illustration of a gel electrophoresis setup[105]

The matrix gel used in the electrophoresis is a polymer the porosity of which can be controlled by the concentration of the composition according to the target samples. Generally, agarose and polyacrylamide are the two most common matrix materials for gel electrophoresis. The agarose gel is formed by gelation

through hydrogen bonding and electrostatic interactions. The polyacrylamide gel is composed of cross-linked polyacrylamide with the help of *N, N'*-methylenebisacrylamide.

Compared to polyacrylamide gel, agarose gel is thermally reversible. The formation of agarose gel is a simpler and more reproducible procedure than polyacrylamide gel. The agarose gel exhibits relatively large pore size, which requires a relatively short experimental time.

3.4 Zeta Potential[106]

When charged particles (phase I) are placed in a solvent medium (phase II), such as colloidal systems, there is a tendency for the electric charges to distribute in a non-uniform way at the interface. The arrangement of the charges on the surface of phase I and the charges in the liquid phase II is referred to the electrical double layer at the interface. This double layer may be considered to consist of two parts: one part is called stern layer (or compact layer), it is an inner region which includes ions bound relatively strong to the surface of phase I. The outer part is known as diffusion layer in which the ion distribution is determined by a balance of electrostatic force and random thermal motion. The potential in this region, therefore, decays with the distance from the surface, until it becomes zero in the bulk liquid far away from the surface of phase I (Figure 3.4.1).

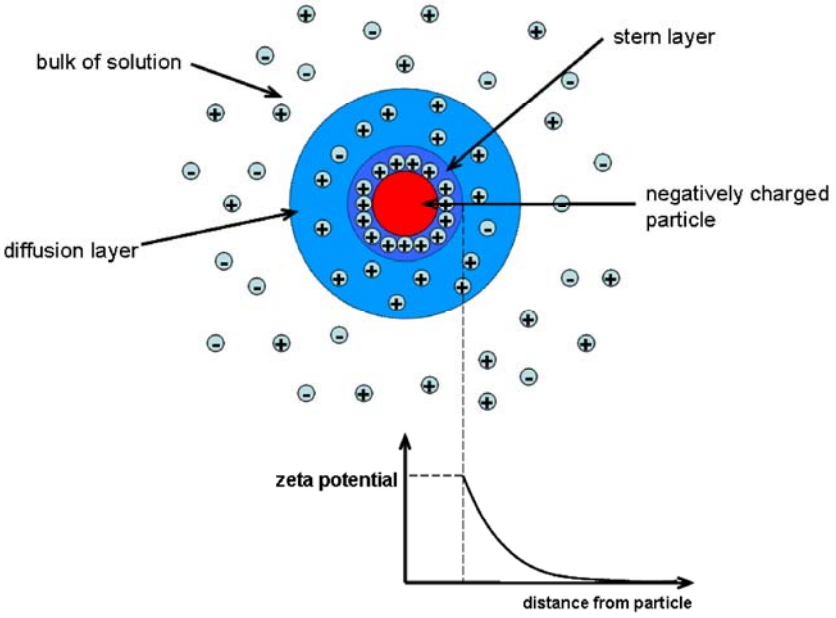

Figure 3.4.1. Illustration of double layer and zeta potential

The zeta potential (ζ-potential) is defined as the electric potential difference between the boundary of the stern layer and the bulk fluid far away from the interface. There are various techniques for determining the zeta potential based

on different electrokinetic effects, which are electrophoresis, electro-osmosis, streaming potential and sedimentation potential. Among them, electrophoresis is the most common technique. In this method, the ζ-potential is determined by placing the particles in an electric field E and measuring their velocity v_E in the solution. It yields the electrophoretic mobility u_E which relates to the ζ-potential according to the Smoluchowski equation:

$$u_E = \frac{v_E}{E} = \frac{\varepsilon_o \varepsilon_r \xi}{\eta} \qquad [3.31]$$

where ε_r is the relative dielectric constant, ε_o is the electric permittivity of a vacuum, η is the viscosity of the solution. This equation is applied for a large particle with a thin double layer. If it is a small particle with a relatively thick double layer, instead of equation 3.31, one obtains the Henry equation:

$$u_E = \frac{2\varepsilon_o \varepsilon_r \xi}{3\eta}(1 + kr) \qquad [3.32]$$

where r is the particle radius and k is the inverse Debye-Hückel screening length.

The zeta potential is an important parameter for a number of applications including characterization of biomedical polymers, electrokinetic transport of particles and microfluidics etc. Moreover, the value of zeta potential can be related to the stability of colloidal systems. The zeta potential indicates the degree of repulsion between like-charge particles in a dispersion. A colloidal solution with a high absolute ζ-potential value (normally $|\zeta|$ ≥ 30 mV) are considered to be electrostatically stable since the charged particles repel each other and resist the aggregation. When the potential is too low (usually $|\zeta|$ ≤ 5 mV), the repulsive force between particles cannot prevent the coagulation or flocculation. It is then often an instable system. However, the size of the particles can influence the ζ-potential measurements, which should be taken into account in the interpretation of ζ-potential results.

CHAPTER 4. ASSOCIATION OF DNA WITH ORGANIC COUNTERIONS

4.1 Introduction

In this chapter, the association of DNA with non-planar and thus non-intercalating counterions is discussed. The focus is on the external binding of the counterion to the DNA strand by electrostatic interaction and investigating the capability of di- and multivalent counterions to induce aggregation of multiple DNA molecules. The main question here is whether it is possible to form stable assemblies of DNA and counterions in solution. Different organic counterions are applied to deduce a systematic behavior. In particular, this includes stiff counterions because multivalent stiff counterions allow for the formation of defined complexes via “electrostatic self-assembly” with other macroions.[35,36,39] The perylene based tetravalent ion PSPDI (Figure 4.1.1) is a water soluble dye with high fluorescence quantum yield and photostability.[107] Its three-dimensional molecular structure suggests that it is impossible for PSPDI to intercalate into the DNA helix because of the steric hindrance arising from the groups surrounding the aromatic system. Thus it is expected to bind on the outside of the DNA helix and potentially connect multiple DNA strands. Moreover, exhibiting two different charge distances offers more possibilities to arrange in the complex formation. In particular the smaller charge distance corresponds to the distance of adjacent phosphate groups on the DNA double strand. Thus a different behavior as compared to classical porphyrins is expected. The solubility in aqueous solution and its optical properties may lead to applications in the biological area.[67,108] Methyl viologen MV^{2+} (Figure 4.1.1) is an excellent electron acceptor with which

photoinduced electron transfer can be achieved.[109,110,111,112] Additional potential may thus lie in the PSPDI and MV^{2+} counterions apart from serving as model probes. The other two counterions $C6D^{2+}$ and $C6T^{4+}$ shown in Figure 4.1.1 are utilized to compare with different systems. The alkyl chain in between the charges brings more flexibility of those counterions as compared to the stiff ones. The 3-D structure of the head group also ensures a non-intercalating interaction with DNA strands. In addition to varying the counterion, studies on counterion/DNA ratio and two types of DNA, linear and supercoiled DNA with the same molar mass, are performed. Complexes are mainly investigated in solution by static and dynamic light scattering, UV-Vis spectroscopy and after deposition on a surface by AFM.

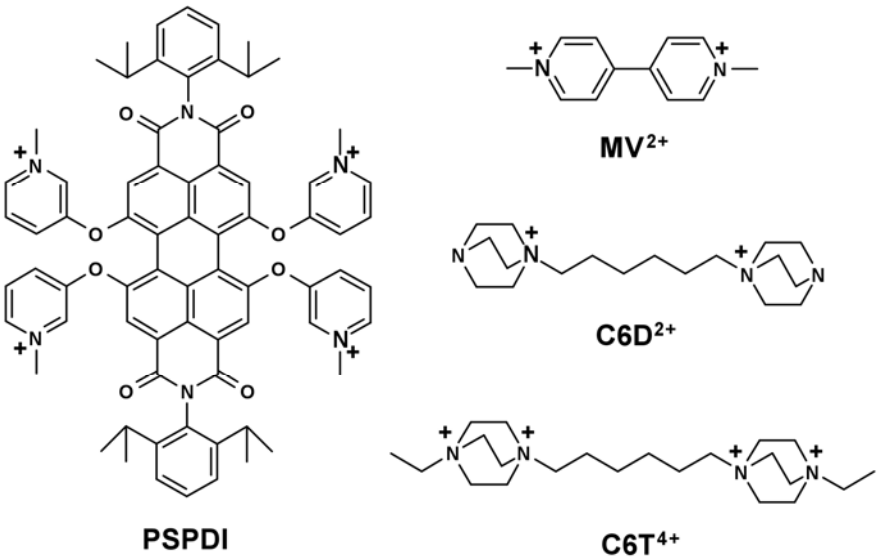

Figure 4.1.1. Structural formulae of organic counterions

4.2 Characterization of DNA

First, the DNAs used in this work were characterized. DNA is not only the key secret of life, but also a highly charged polyelectrolyte. It is well known that polyelectrolytes exhibit so-called “polyelectrolyte effects” in the absence of additional low molecular weight salt, such as NaCl (see Chapter 2.3). In order to avoid the polyelectrolyte effects in light scattering measurements, the DNA is dissolved in 1 X Tris-EDTA (TE) buffer solution, which contains 10 mM Tris and 1mM EDTA. TE buffer is a commonly used solution to protect DNA or RNA from degradation. The pH of the buffer solution used in this work is around 7.5. At this pH value, around 78% amino group of the Tris molecules are protonated, which means that there are approximately 7.8 mM monovalent “salt” in the solution. Concerning the fact that the working concentration of negative charges from DNA varies from 0.0154 mM to 0.31 mM (DNA concentration is between 0.005 gL^{-1} and 0.1 gL^{-1}), it is sufficient to eliminate the polyelectrolyte effects by 1 X TE buffer solution.

Figure 4.2.1 shows typical electric field autocorrelation functions and distributions of relaxation times for supercoiled pUC19 in 1 X TE buffer at various scattering angles. From the plots, it is obvious that by inverse Laplace Transformation of the autocorrelation function using a constrained regularization method (CONTIN), predominantly one distribution of decay times is found, while with increasing scattering angles, a small second peak appears. It has been reported that this second peak is due to the internal modes of a large molecule.[113,114,115] The reason for the internal mode can be explained as follows:[116] the autocorrelation function of dynamic light scattering contains contributions from macromolecular translational motion and various internal motions of the polymer. The relative contributions of those motions depend on the product of the scattering vector q and the radius of gyration R_G. When qR_G << 1, translational diffusion is the dominant contribution; when qR_G >> 1, the observation scale is small, and the

scattering is substantially influenced by the motion of chain segments, i.e. internal dynamics of the macromolecule; when qR_G ≈ 1, the internal motion of the macromolecule begins to contribute significantly to the autocorrelation function.

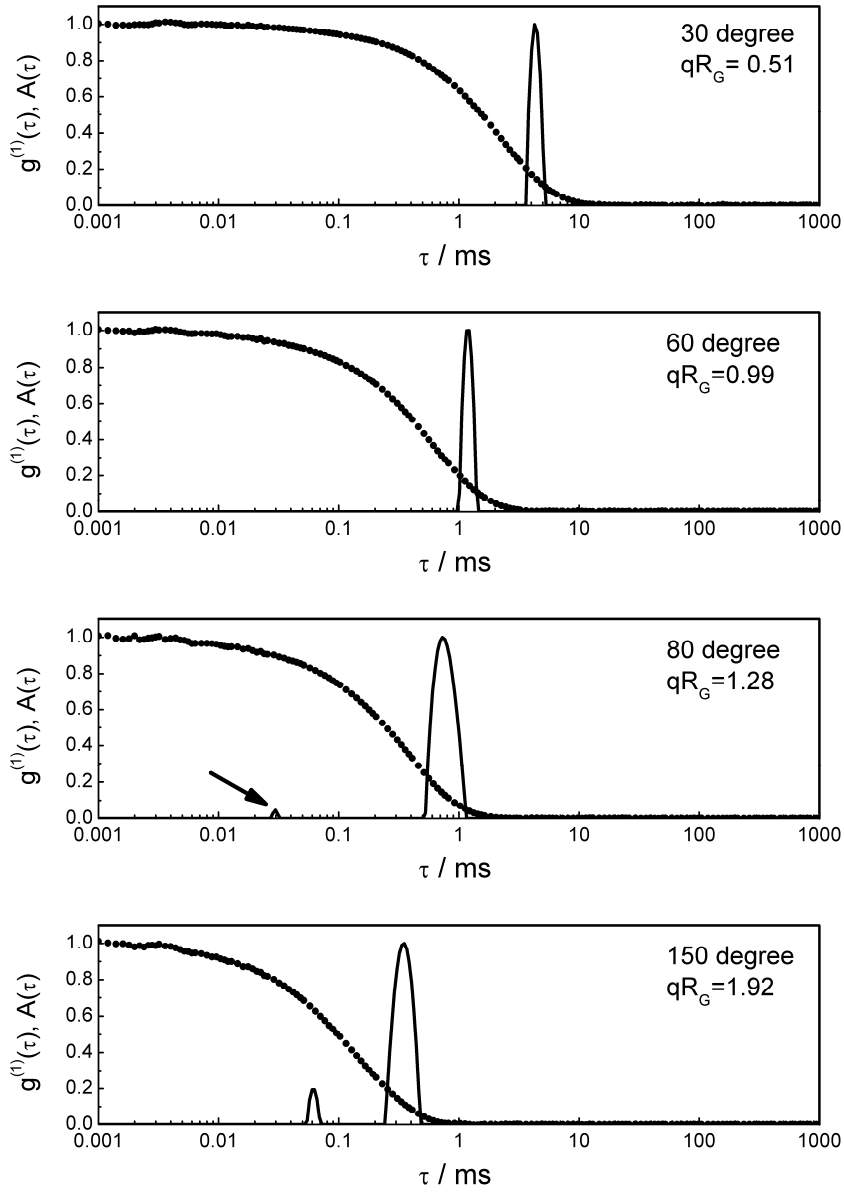

Figure 4.2.1. Normalized electric field autocorrelation functions $g^{(1)}(\tau)$ and relaxation time distributions $A(\tau)$ of supercoiled pUC19 at different scattering angles. (c(DNA) = 0.01 gL^{-1} in TE buffer)

Experiments show that at scattering angles 30° and 60°, which means that the qR_G value is below 1 (0.51 and 0.99, respectively), there is only one distribution

of relaxation times monitored. It represents the translational diffusion behavior of single DNA molecule. When the scattering angle becomes larger until the qR_G value is around 1 (θ = 80°, qR_G = 1.28), the second peak appears (marked with arrows). By increasing the scattering angle to 150° (qR_G = 1.92), the second peak is more pronounced. It shows that the internal motion contributes more and more to the scattering signals with increasing qR_G value. This result is consistent with the theoretic knowledge mentioned.

Figure 4.2.2 shows the diffusion coefficient as a function of scattering vector square by the translational motion. By extrapolating the curve to zero scattering vector, a D_{app} of 4.8·10^{-12} m^{2}s^{-1} results. According to the Einstein-Stokes equation 3.29, this yields a R_H = 44.8 nm. The low slope of the plot also confirms the narrow distribution of the molecules.

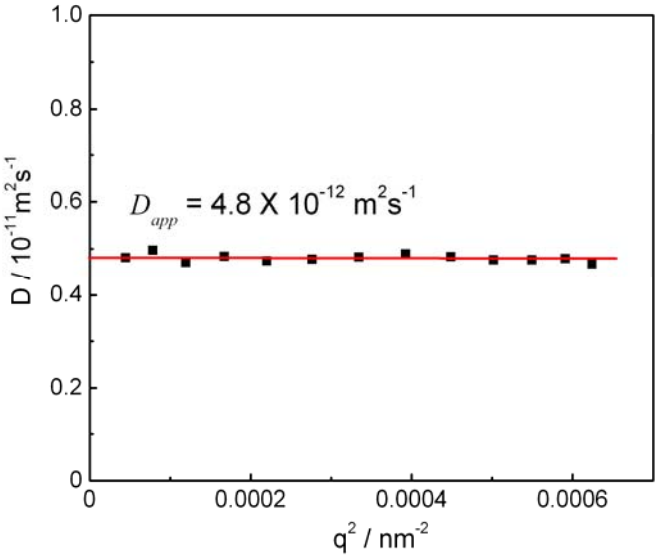

Figure 4.2.2. Diffusion coefficient as a function of scattering vector square for supercoiled pUC19. (c(DNA) = 0.01 gL^{-1} in TE buffer)

Different information can be extracted from SLS measurements. Figure 4.2.3 shows a Zimm plot for supercoiled pUC19 in TE buffer with various concentrations. Data analysis is performed by plotting $Kc/R(\theta)$ as a function of (q^2+kc) for each sample concentration. Extrapolating to q = 0 yields $Kc/R(\theta)_{q=0}$,

plotting this value versus the sample concentration and extrapolating to c = 0 gives $Kc/R(\theta)_{q=0,c=0}$, which is the reciprocal value of M_w. The radius of gyration R_G is calculated by taking the slope of $Kc/R(\theta)$ versus (q^2+kc) for each concentration and the extrapolation value $Kc/R(\theta)_{q=0}$ with the formula 3.15. From the slope of the concentration dependence, the second virial coefficient A_2 is obtained.

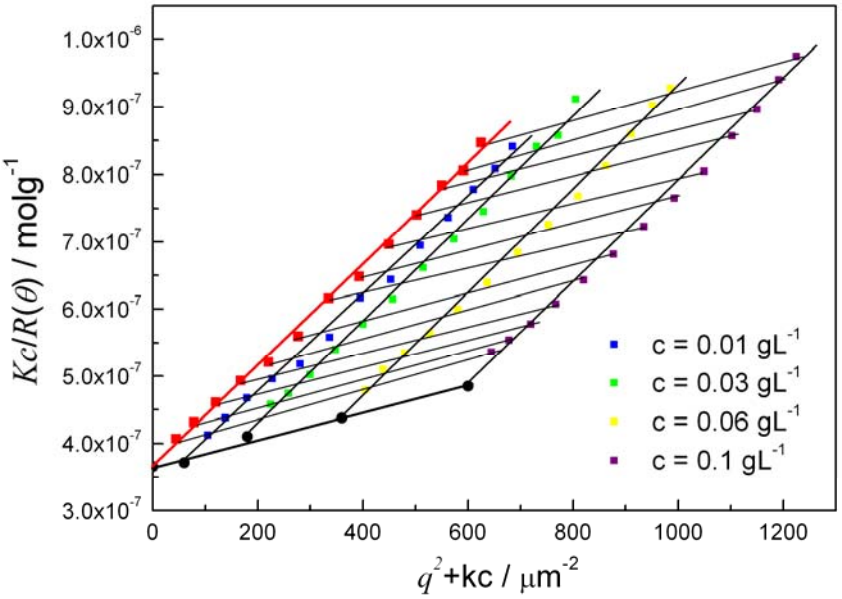

Figure 4.2.3. Zimm plot of supercoiled pUC19 in 1 X TE buffer

Considering the fact that the dn/dc value of a pure DNA solution does not change significantly upon various buffer solutions, a dn/dc value of 0.17 mLg^{-1} from literature is used.[117,118,119] Then the weight average molecular mass M_w and the second virial coefficient A_2 of pUC19 in TE buffer is calculated to be (2.7 ± 0.3)·10^6 gmol^{-1} and (6 ± 0.2)·10^{-4} molmLg^{-2}, respectively. The value of the second virial coefficient is comparable to that obtained from other authors,[117,120] while the molecular weight is higher than the theoretical prediction of molecular weight of a pUC19 molecule (1.7·10^6 gmol^{-1}). The possible reason might be that the DNA molecules are slightly aggregated in the solution. The hydrodynamic radius R_H, radius of gyration R_G and their ratio R_G/R_H for supercoiled pUC19 at different concentrations are shown in Figure 4.2.4. It is evident that with increasing DNA

concentration, both R_H and R_G slightly decrease. The R_G/R_H ratio is almost constant in the whole concentration range.

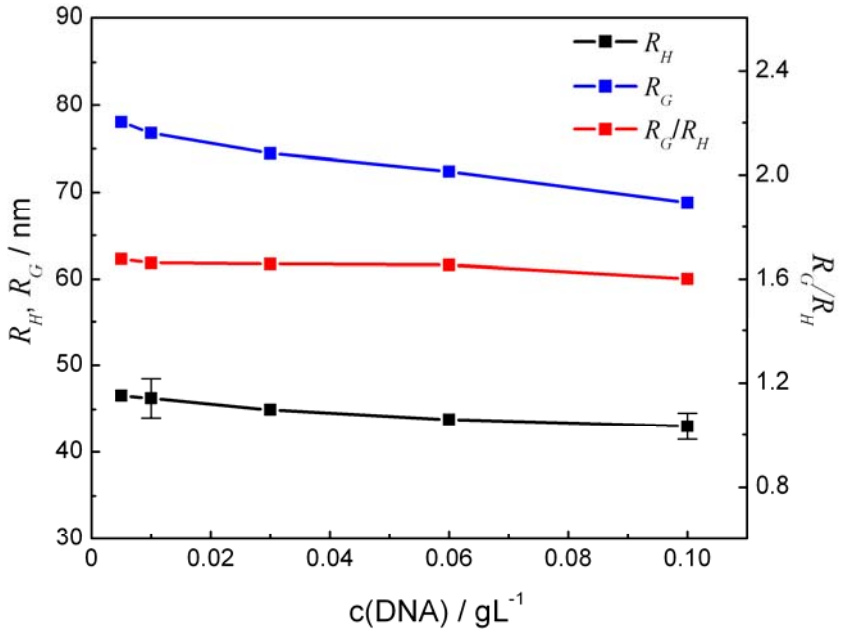

Figure 4.2.4. Hydrodynamic radius R_H, radius of gyration R_G and R_G/R_H ratio of supercoiled pUC19 as a function of DNA concentrations

The combination of hydrodynamic radius and radius of gyration is a useful tool that indicates the particle structure.[121,122] The radius of gyration is geometrically defined, while the hydrodynamic radius is also determined by the hydrodynamic interaction. R_G/R_H ratio becomes smaller if the particle is more compact. For example, the R_G/R_H ratio of a monodisperse random polymer coil in good solvent is 1.78, while that of a homogenous sphere is 0.778.[96] The R_G/R_H ratio of supercoiled pUC19 in TE buffer is estimated around 1.65 at concentration of 0.01 gL^{-1}, and it is almost constant in the DNA concentration range from 0.005 gL^{-1} to 0.1 gL^{-1}, which indicates that in this regime, supercoiled pUC19 keeps the same morphology in buffer solution. This result also suggests that it is safe to carry out later experiments in this DNA concentration range. Finally the normal DNA concentration for further work is decided to be 0.01 gL^{-1}, unless mentioned otherwise.

The linear pUC19 is obtained by directly cutting supercoiled pUC19 with the help of restriction enzyme BamHI. Therefore the number of base pairs and molecular weight of the linear DNA are the same as the ones of the supercoiled DNA. The digestion reaction was characterized and confirmed by 1% agarose gel electrophoresis, which is shown in Figure 4.2.5. It is evident that there is an electrophoretic mobility difference between supercoiled and linear DNA. The supercoiled DNA (lane 2) moves faster than linear one (lane 1) because supercoiled DNA has more compact form, and the length of the supercoiled molecule is only half as compared to linear one. The supercoiled DNA is thus expected to move faster than linear one under same conditions. This difference observed in the gel electrophoresis is in agreement with other results[123,124] and confirms the successful cutting of supercoiled DNA. The digestion solution was then purified by phenol/chloroform extraction and precipitation with ethanol. The UV absorbance ratio A_{260}/A_{280} was measured in order to check for protein contamination. Values between 1.84 ~ 1.88 were obtained to ensure an essentially protein-free DNA.

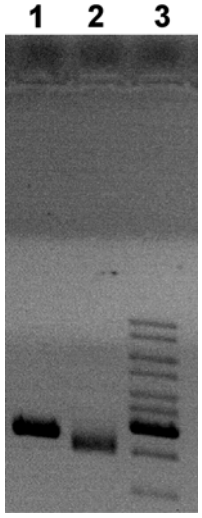

Figure 4.2.5. Agarose gel image for digestion reaction. Lane 1: linear pUC19, lane 2: supercoiled pUC19, lane 3: DNA ladder. (direction of movement: downward)

Linear pUC19 was also characterized by both dynamic and static light scattering. The diffusion coefficient as a function of scattering vector and Zimm plot of linear

pUC19 is shown in Figure 4.2.6. From DLS, by extrapolating the curve to zero scattering vector, linear pUC19 exhibits a D_{app} of $3.3 \cdot 10^{-12}$ m^2s^{-1} and thus yields a hydrodynamic radius of 66 nm. From SLS, a radius of gyration of 77 nm is received.

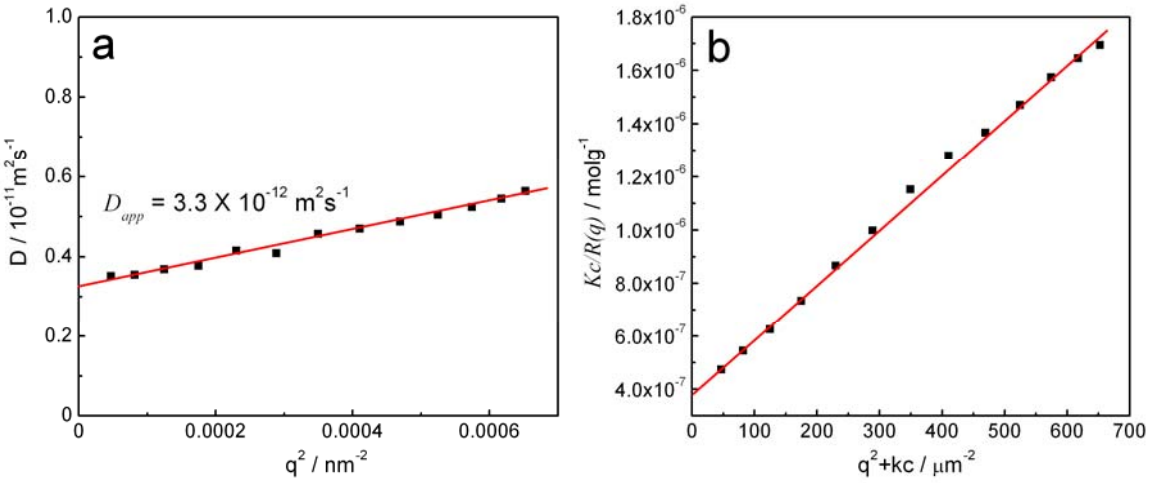

Figure 4.2.6. (a) Diffusion coefficient as a function of scattering vector square and (b) Zimm plot for linear pUC19. (c(DNA) = 0.01 gL^{-1} in TE buffer)

The light scattering results of both DNAs are summarized in Table 4.2.1. It shows that at a concentration of 0.01 gL^{-1}, linear pUC19 yields a larger R_H (66 nm) and R_G (126 nm) than supercoiled pUC19 with R_H = 46 nm and R_G = 77 nm. Similar results were also found by other authors.[125, 126] The structural difference is evident from the characteristic ratio R_G/R_H. The R_G/R_H ratio for supercoiled and linear pUC19 in TE buffer is 1.66 and 1.89, respectively. Thus supercoiled pUC19 is indeed in a more compact form than linear one, as expected. It is also in consistence with the gel electrophoresis result.

DNA	D_{app} / m^2 s^{-1}	R_H / nm	R_G / nm	R_G/R_H
Supercoiled pUC19	4.7 x 10^{-12}	46.3	76.8	1.66
Linear pUC19	3.3 x 10^{-12}	66.7	126.2	1.89

Table 4.2.1. Light scattering results of DNA samples used in this study. c(DNA) = 0.01 gL^{-1} in 1 x TE buffer, pH is around 7.5

AFM has been widely applied to image biological molecules and their complexes.[127,128,129] To investigate the morphology of DNA assemblies, a reliable and reproducible substrate must be selected that as far as possible represents the solution structures. The most common substrate for AFM is mica due to its large atomically smooth surface areas.[130] As mica has a negatively charged surface, several methods were developed to immobilize negatively charged DNA molecules on a mica surface. The first method is to use divalent metal ions, such as Mg^{2+} or Ni^{2+}.[131,132] The function of the divalent ions here is to form a charge bridge between the negative mica surface and negative phosphate groups of DNA backbone, so that DNA molecules can be immobilized on the mica substrate (Figure 4.2.7a).[133] The second method is to modify the mica surface with 3-aminopropyltriethoxysilane (APTES). The modification process is illustrated in Figure 4.2.7b.[134] When water is present, the APTES monomer hydrolyses first and hydroxyl groups result. They cross-link and polymerize into silicon gels. The exposed hydroxyl groups react with neighboring hydroxyl groups to form Si-O-Si covalent bonds, and its amino moieties remain stable on the mica surface. When DNA molecules are deposited onto this surface, the amino moieties can electrostatically adsorb negatively charged DNA. The advantage of this method is that no additional divalent cations are needed for immobilization, which might influence the complexation reaction. The charge density of the surface can be easily controlled by varying the concentration of APTES solution. Both methods are tested in this work.

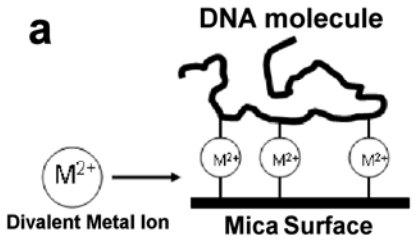

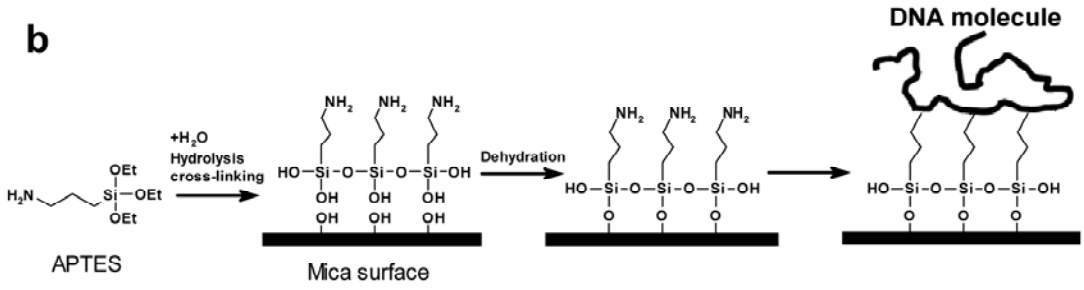

Figure 4.2.7. Schematic drawing of immobilization of DNA molecules on mica surface by (a) divalent metal ions and (b) APTES

Figure 4.2.8 shows an AFM image of supercoiled pUC19, which is deposited from a solution containing 5 mM $MgCl_2$. It is obvious that most of the DNA molecules are in the shape of open circle and only few DNA molecules are in supercoiled form (marked with arrows). It is due to the fact that DNA molecules equilibrate on the mica substrate into a two-dimensional structure different to the solution structure.[130,135] However, this result does not represent the supercoiled form present in solution.

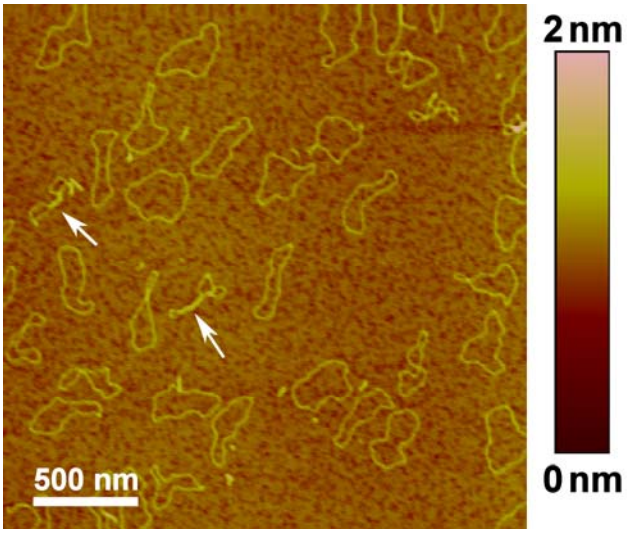

Figure 4.2.8. AFM image of supercoiled pUC19 on bare mica, deposited from a solution containing 5 mM $MgCl_2$

Although modifying mica surfaces with APTES is frequently used in AFM measurements, it should be noted that the charge density of the modified surface

can influence the morphology of the molecules deposited on the surface.[136,137] In order to minimize the influence, the charge density of the surface has to be optimized by varying the concentration of APTES solution. Figure 4.2.9 shows AFM images of supercoiled pUC19 on APTES modified mica with different concentrations. When the concentration of APTES is 0.01%, most of the DNA molecules are still in open circle form which is similar to the morphology of DNA imaged on bare mica with $MgCl_2$ (Figure 4.2.9a). When the APTES concentration is increased to 0.03%, both supercoiled and open circle DNA molecules are observed (Figure 4.2.9b, marked with arrows). If the APTES concentration is increased to 0.05% (Figure 4.2.9c), all the DNA molecules remain in supercoiled form. This represents the structure of supercoiled DNA known for solutions. Further increasing the APTES concentration to 0.1% (Figure 4.2.9d), not only supercoiled structure but also more condensed DNA molecules are present. It implies that at this APTES concentration, the charge density of the surface is high enough to induce further condensation of DNA molecules when they are adsorbed on the surface. Due to the fact that the pUC19 is bought in supercoiled form, and to minimize the influence of the morphology from surface treatment, the mica surface modified with 0.05% APTES solution is chosen as the standard substrate for all the future samples in this work, unless mentioned else wise.

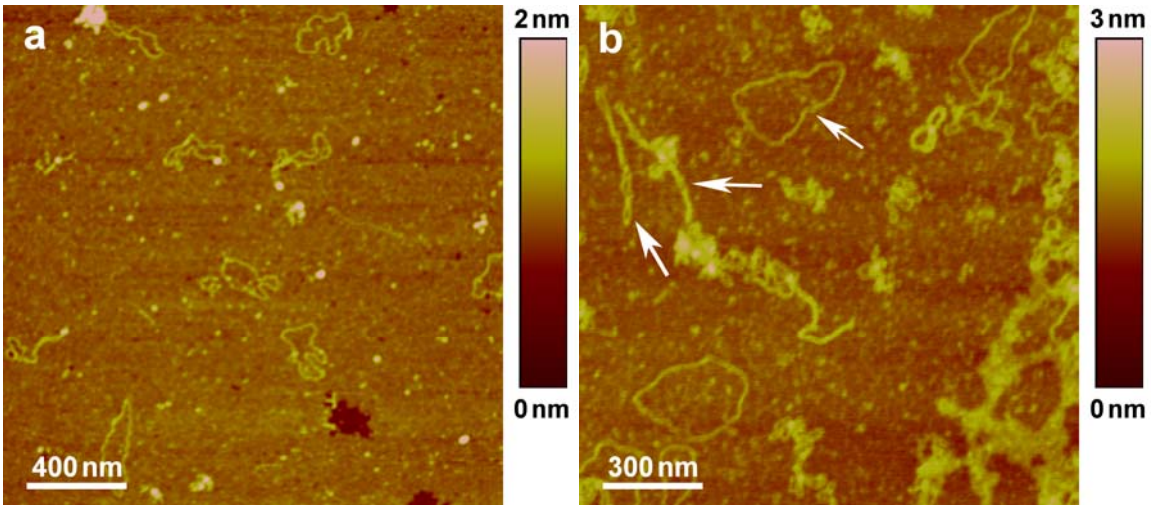

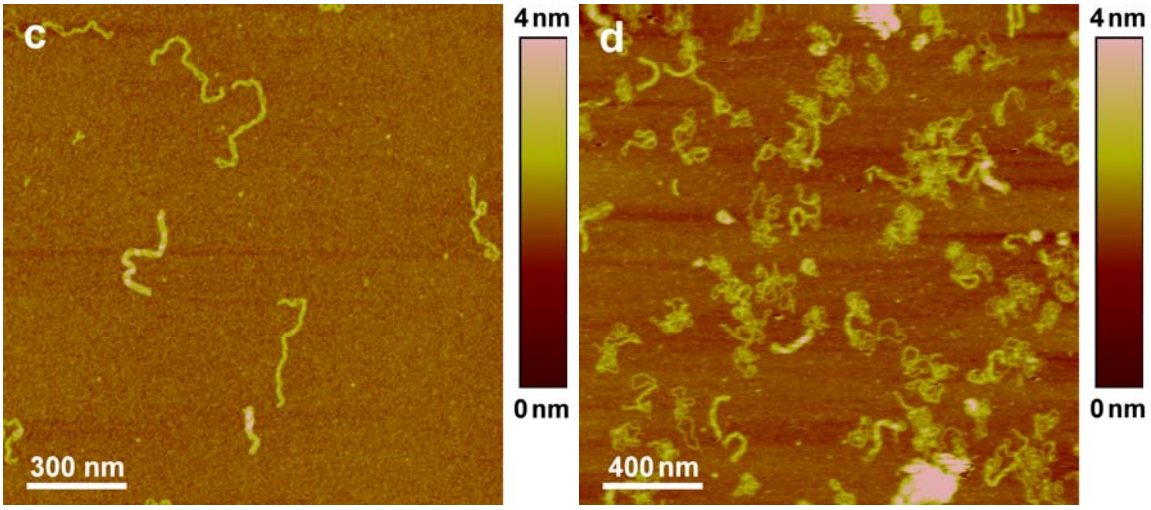

Figure 4.2.9. AFM images of supercoiled pUC19 on (a) 0.01% APTES, (b) 0.03% APTES, (c) 0.05% APTES and (d) 0.1% APTES modified mica. (all: c(DNA) = 0.01 gL^{-1} in 1 X TE buffer)

Figure 4.2.10 exhibits a magnified AFM image of supercoiled pUC19 on 0.05% APTES modified mica surface. It is much clearer that the molecules keep the supercoiled form on the surface. The average height of supercoiled DNA estimated from AFM is (1.5 ± 0.39) nm, which is lower than the value of 4 nm expected for two twisted B-DNA[138] strands. Compression of the molecule by the tip during the scanning process and dehydration of the molecules upon drying are considered as reasons for this reduction.[133, 135, 139] The length of those molecules is counted around (0.46 ± 0.02) µm, as shown in the image.

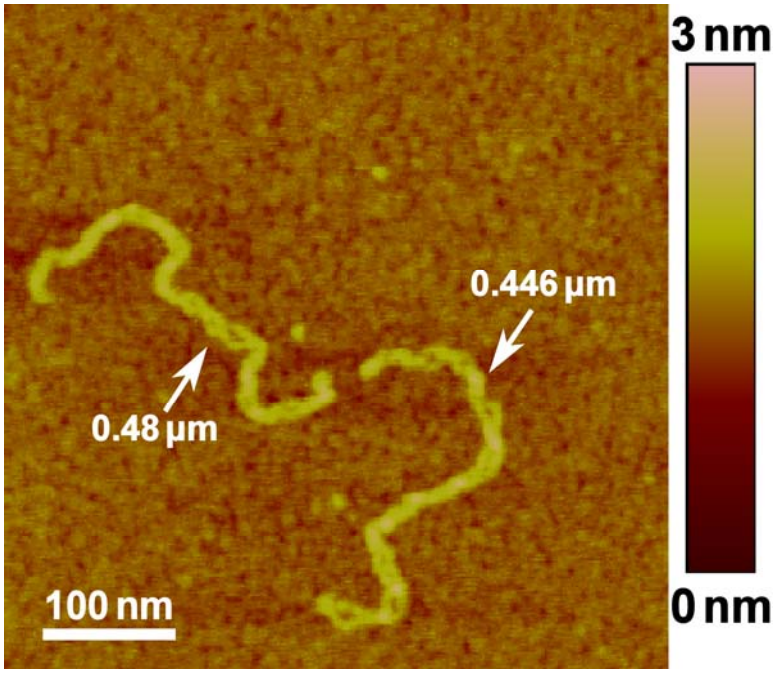

Figure 4.2.10. AFM image of supercoiled pUC19 on 0.05% APTES modified mica. (c(DNA) = 0.01 gL^{-1} in 1 X TE buffer)

Applying 0.05% APTES modified mica surface for linear pUC19, an expected result is obtained, as shown in Figure 4.2.11. The linear DNAs (both in extended and random coil form) are observed. The average height of linear pUC19 is (0.7 ± 0.15) nm, is about half of that for supercoiled pUC19. The length of the molecules is around (0.92 ± 0.02) µm. pUC19 has 2686 base pairs, which corresponds to a contour length of around 0.91 µm. Therefore the lengths of both supercoiled and linear pUC19 obtained here are in very good agreement with the theoretical contour length of pUC19. The AFM results of linear pUC19 thus confirm the successful digestion of the suerpociled pUC19 and testify the optimized experimental conditions for imaging DNA molecules by AFM.

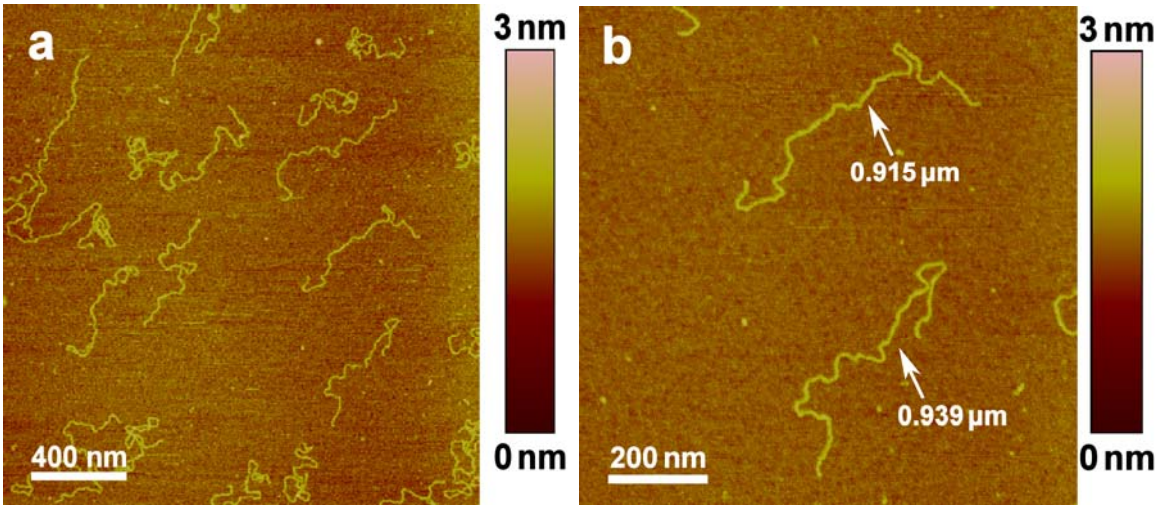

Figure 4.2.11. AFM images of linear pUC19 on 0.05% APTES modified mica. (c(DNA) = 0.01 gL^{-1} in 1 X TE buffer)

4.3 Association of DNA with Divalent Counterions

The complexes induced by supercoiled and linear pUC19 with different divalent counterions were first investigated by light scattering. The charge ratio l is defined as the ratio of the molar concentration of positive counterion charges to the molar concentration of PO_4^- groups of DNA:

$$l = \frac{c(N^+, counterion)}{c(PO_4^-, DNA)}$$

Figure 4.3.1a and b demonstrate typical autocorrelation functions and distributions of relaxation times of pure DNA and their complexes. For both supercoiled and linear pUC19, the clear shift of the distributions suggests the formation of aggregates by DNA and divalent counterions at high charge ratios. With increasing charge ratio, the distributions of supercoiled DNA complexes become broader, which indicates higher polydispersity (Figure 4.3.1a). However, the assemblies formed with linear DNA do not exhibit significant change of polydispersity with increasing charge ratios (Figure 4.3.1b). This difference is also observed in the plots of diffusion coefficient as a function of scattering vector square (Figure 4.3.1c, d). For the aggregates formed with supercoiled DNA, the higher the charge ratio, the bigger slope is obtained. It is consistent with the conclusion of increasing polydispersity from autocorrelation functions. On the other hand, the linear DNA complexes show comparable slopes with various charge ratios, which suggests a higher polydispersity of the samples at lower charge ratios compared to that of supercoiled DNA complexes. The possible reason could be that during the digestion reaction, different sizes of DNA fragments might be produced, which brings a higher polydispersity of linear DNA than supercoiled one. However, the amount of those small fragments should be sufficiently low because they are not detectable in gel electrophoresis.

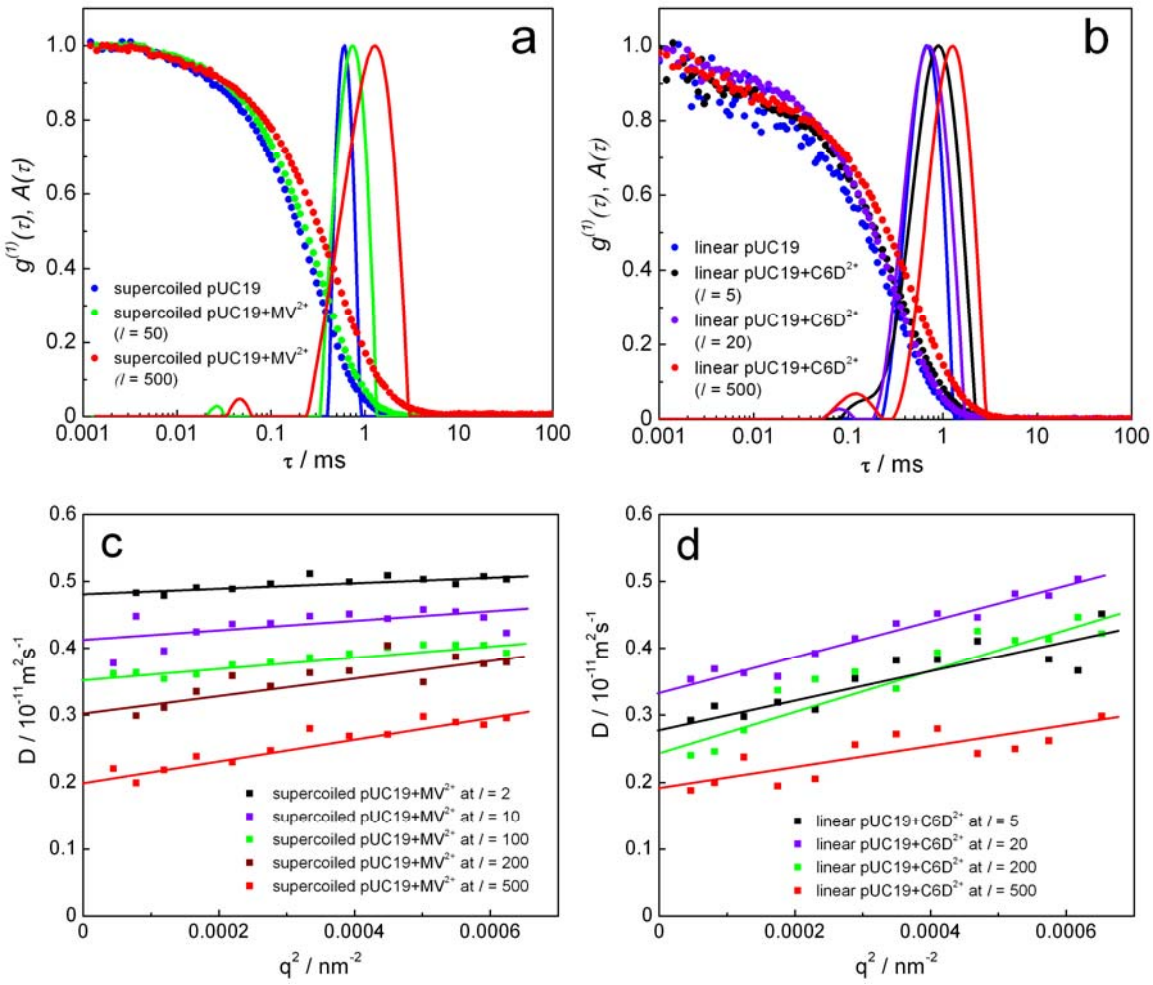

Figure 4.3.1. Normalized electric field autocorrelation functions $g^{(1)}(\tau)$ and distributions of relaxation times $A(\tau)$ at a scattering angle of 90° for complexes induced with (a) supercoiled pUC19 and (b) linear pUC19; diffusion coefficient as a function of scattering vector square for assemblies formed with (c) supercoiled pUC19 and (d) linear pUC19; (all: c(DNA) = 0.01 gL^{-1} in TE buffer)

Concerning the high amount of counterions, the question arises whether the changes observed in light scattering are due to the complexation of DNA and counterions or due to the aggregation of counterion itself. Therefore a pure counterion solution was investigated for comparison. The light scattering result shows that even at MV^{2+} concentration 26 times higher than that for the complexation, no measureable autocorrelation function is obtained, which means there are no aggregates in the pure counterion solution. This experiment thus proves that the complexes we obtained before have to be a consequence of

interaction between DNA and counterions, not due to the aggregation of counterions.

Figure 4.3.2 shows examples of SLS data for complexes formed with both types of DNA and different divalent counterions. All the data are presented as Zimm plot. The assemblies formed with different type of DNA exhibits different behaviors in SLS: for supercoiled DNA complexes, the molecular weight continuously increases with increasing charge ratios. For linear DNA complexes, the size of the particles decreases first at low charge ratios while the molecular weight of the particles does not change significantly, which suggests no aggregation of multiple DNA molecules occurs at this stage. Increase of molecular weight is only observed at higher charge ratios where the R_G of the complexes increases.

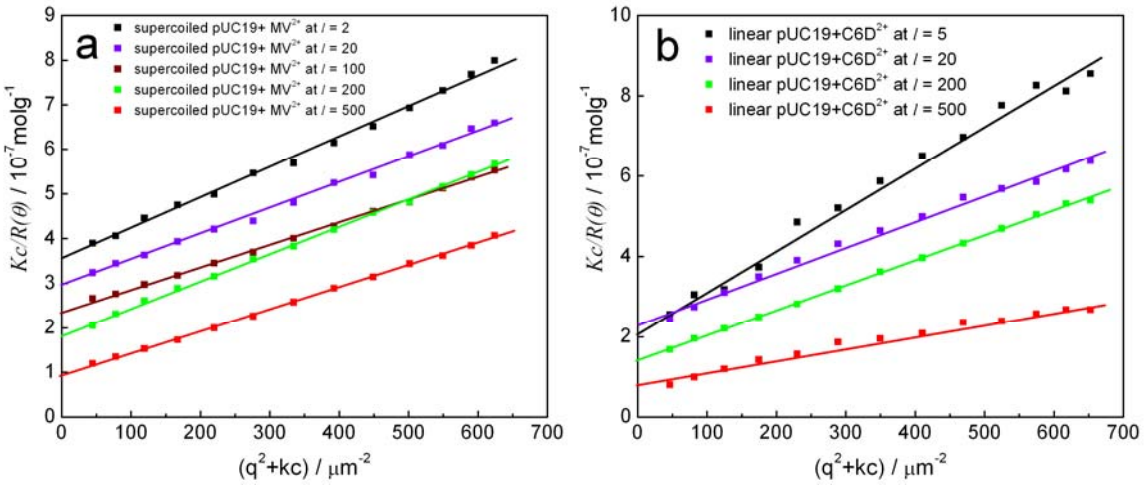

Figure 4.3.2. $Kc/R(\theta)$ as a function of scattering vector square for assemblies formed by (a) supercoiled pUC19 with MV^{2+} and (b) linear pUC19 with $C6D^{2+}$. (all: c(DNA) = 0.01 gL^{-1} in TE buffer)

Systematic results of aggregate size for different DNA/counterion combinations are given in Figure 4.3.3. For both divalent counterions MV^{2+} and $C6D^{2+}$, similar association behavior is observed: for supercoiled DNA complexes, R_H and R_G do not show significant changes up to a charge ratio of l = 50. The onset of growth depends on the DNA type. For linear DNA complexes, R_H and R_G increase for

charge ratio $l \geq 200$ (green and red line). At a charge ratio of l = 500, both supercoiled and linear DNA form complexes with $R_H \approx 110$ nm. The difference between supercoiled and linear DNA complexes is essentially found at low charge ratios: almost no changes in R_H and R_G are detected for supercoiled DNA complexes at low charge ratios, but the R_H and R_G of the linear DNA complexes decreases from the initial value of 76 nm to 64 nm and 119 nm to about 95 nm at l = 10, respectively. They both stay approximately constant for $10 \leq l \leq 100$. Then R_H and R_G increases with increasing charge ratio. This different complexation behavior may be explained by the larger excluded volume and larger flexibility of linear DNA prior to association. When the counterions are added into the DNA solution, the size of single DNA molecules may first be reduced by screening of electrostatic repulsion between phosphate groups, so that both R_H and R_G decrease. In difference, the size of supercoiled DNA is less sensitive to the influence of the counterion unless intermolecular aggregation is induced and it increases. Thus the divalent counterions MV^{2+} and $C6D^{2+}$ form complexes with different types of DNA in aqueous solution at room temperature, at high charge ratios.

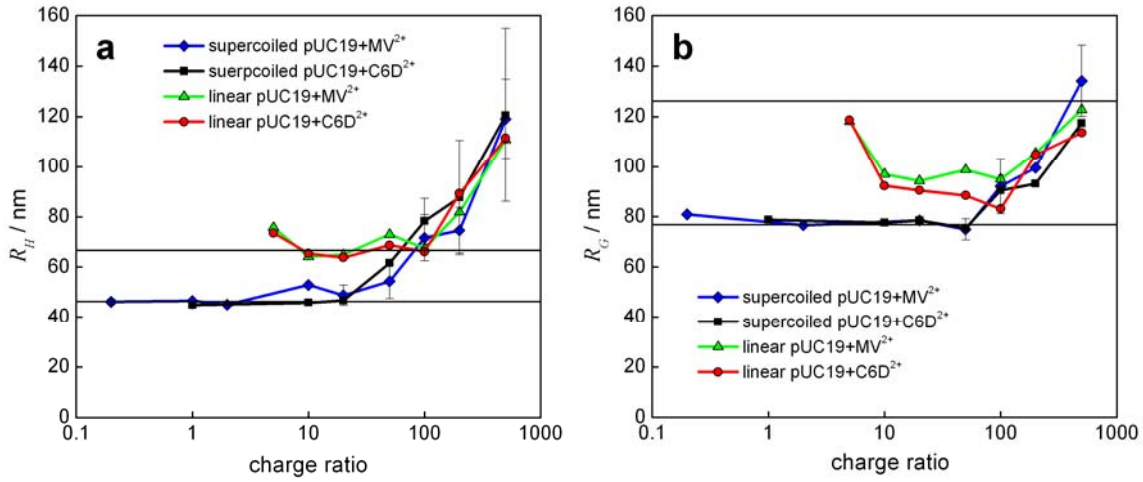

Figure 4.3.3. Light scattering results of complexes formed by supercoiled and linear pUC19 with different divalent counterions: (a) hydrodynamic radius R_H and (b) radius of gyration R_G. Horizontal lines: pure supercoiled pUC19 (lower line) and linear pUC19 DNA (upper line). (all: c(DNA) = 0.01 gL^{-1} in TE buffer)

Figure 4.3.4 shows the characteristic ratio R_G/R_H of the samples above. For all DNA/counterion combinations the ratio decreases with increasing charge ratio (and increasing R_H of the complexes), indicating the formation of somewhat more compact aggregates. The characteristic ratio of all the DNA complexes reaches approximately R_G/R_H = 1.1 at l = 500, which implies that similar aggregate structures are obtained for all complexes.

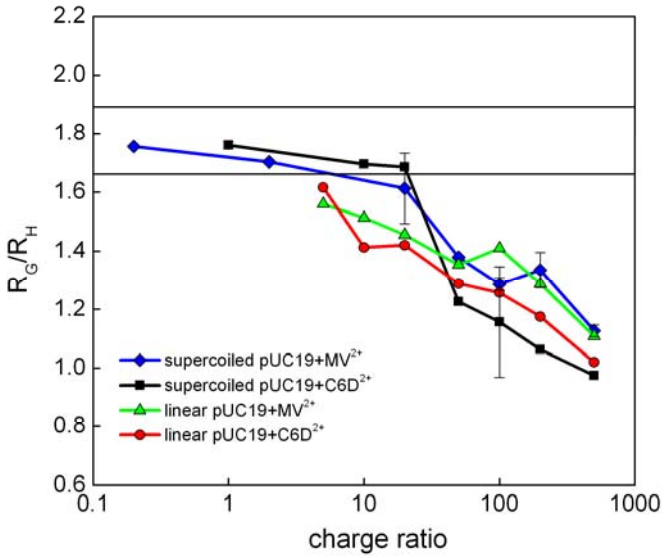

Figure 4.3.4. Characteristic ratio R_G/R_H of complexes induced by supercoiled and linear pUC19 with different divalent counterions. Horizontal lines: pure supercoiled pUC19 (lower liner) and linear pUC19 (upper line). (all: c(DNA) = 0.01 gL^{-1} in TE buffer).

By extrapolating $Kc/R(\theta)$ to zero scattering vector, a relative scattering intensity can be deduced that is shown as function of charge ratio in Figure 4.3.5. From the increase in scattering intensity of the samples, it is evident that the molecular weight of the DNA/counterion complexes increases with charge ratio, which indicates that a DNA/counterion aggregate at high charge ratios consists of multiple DNA molecules.

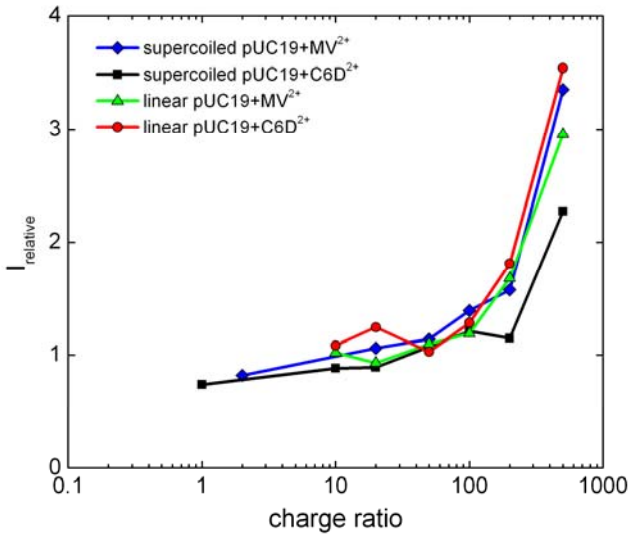

Figure 4.3.5. Relative scattering intensity of aggregates formed by supercoiled and linear pUC19 with different divalent counterions (all: c(DNA) = 0.01 gL^{-1} in TE buffer).

The influence of total concentration on complexes associated by supercoiled pUC19 and MV^{2+} was also investigated. Figure 4.3.6 shows the light scattering results of samples at charge ratio of 100 and 500. In both cases, R_G and R_H first increase with increasing DNA concentration and then remain approximately constant for 0.06 gL^{-1} ≤ c(DNA) ≤ 0.1 gL^{-1}. R_G/R_H does not show significant changes in the investigated concentration range, which implies that although the size of complexes changes with concentration, the structure of the assemblies remains approximately the same.

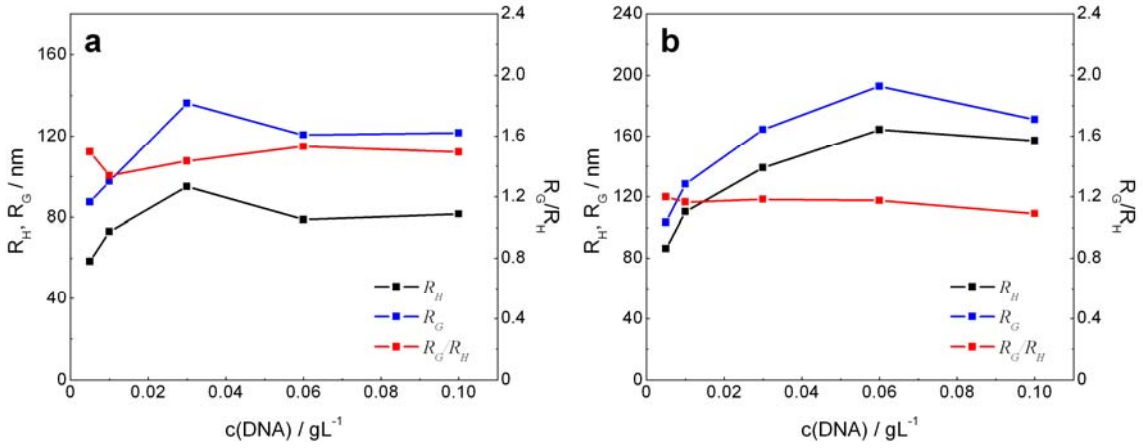

Figure 4.3.6. Light scattering results for aggregates induced by supercoiled pUC19 and MV^{2+} in TE buffer at: (a) charge ratio l = 100, (b) charge ratio l = 500

Furthermore, the stability of the complexes induced by divalent counterions was investigated (Figure 4.3.7). It is evident that both aggregates formed with either $C6D^{2+}$ at charge ratio of 100 or MV^{2+} at charge ratio of 500 show no significant changes in the hydrodynamic radius and radius of gyration for 60 and 40 days, respectively. The R_G/R_H ratios show a slight increase over time. It indicates that the complexes induced by divalent counterions are relatively stable in size but the structure may become slightly looser after about 1 month.

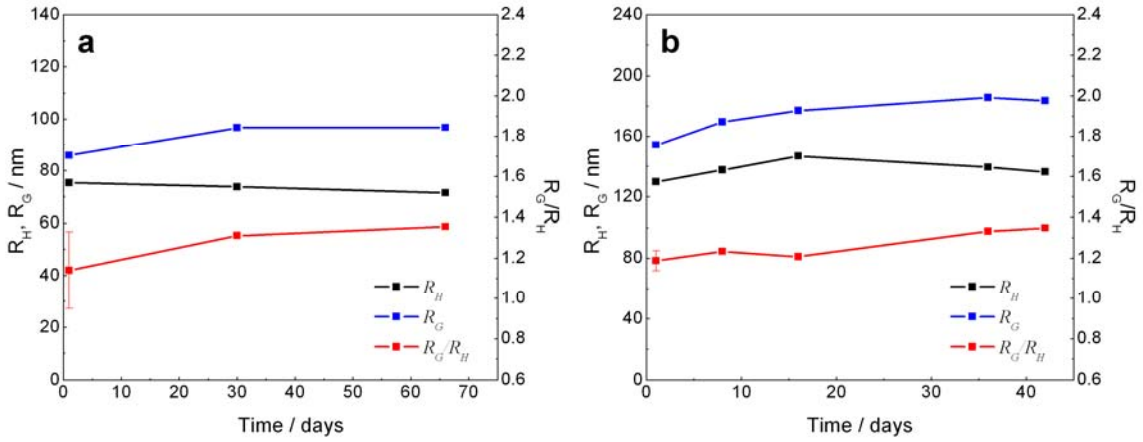

Figure 4.3.7. Stability of complexes formed with supercoiled pUC19 and (a) $C6D^{2+}$ at charge ratio of 100, (b) MV^{2+} at charge ratio of 500

As introduced in Chapter 3.3, gel electrophoresis has been also suggested to be a simple and effective method for studying DNA complexes qualitatively and/or quantitatively.[140, 141] Ma and Bloomfield investigated DNA condensation with NaCl, $MgCl_2$, $Co(NH_3)_6^{3+}$ and $spermidine^{3+}$ in gel electrophoresis.[142] Their results of the fractional charge neutralization of DNA with various counterions calculated from electrophoresis mobility are in good agreement with the theoretical predictions from counterion condensation theory. In this study, the aggregation of DNA with MV^{2+} in a broad range of charge ratio was studied by this technique, not only for confirming the formation of DNA complexes, but also for obtaining the information about the charge neutralization of DNA molecules with MV^{2+}.

Figure 4.3.8 shows an agarose gel image of supercoiled pUC19 and its complexes formed with MV^{2+}. Firstly, pure supercoiled pUC19 (lane 2) exhibits two bands. The main bottom band is caused by the DNA molecules in supercoiled form. The much weaker middle band is originated from the nicked circle DNA, which is always present due to the manufacturing process of supercoiled DNA. Secondly, it is found that for samples at charge ratio $l \geq 50$ where complexes are formed (R_H increases in light scattering), extra bands are observed at the very top, i.e. the starting point (lane 5 ~ 8). It implies that the complexes induced by DNA and counterions are almost fully neutralized so that they do not move in the electric field. This is a proof of complexes existing in the solution. The higher the charge ratio, the more pronounced complex band can be seen via stronger absorption intensity, and accordingly a less intense DNA band is observed. Thirdly, no visible complex bands can be observed for the samples with charge ratio $l < 50$ (lane 3 ~ 4), which is in agreement with light scattering results. However, the free DNA bands at the bottom show less intensity compared to pure DNA sample. It indicates that certain amount of DNA molecules are fully neutralized due to the counterion condensation even though the aggregation of multiple DNA chains is not provoked yet at low charge ratios. Finally, even for complexes at charge ratio $l = 500$, a weak free DNA band is obtained. It is not expected to observe a band of unbound DNA in the gel at excess of counterions. One possible explanation for the free DNA is that the complex might be disassembled under electric field since the complex is formed mainly by electrostatic interaction. Therefore it may not be possible to carry out quantitative analysis via gel electrophoresis for our complex system. However, it qualitatively confirms the formation of DNA complexes with divalent counterions.

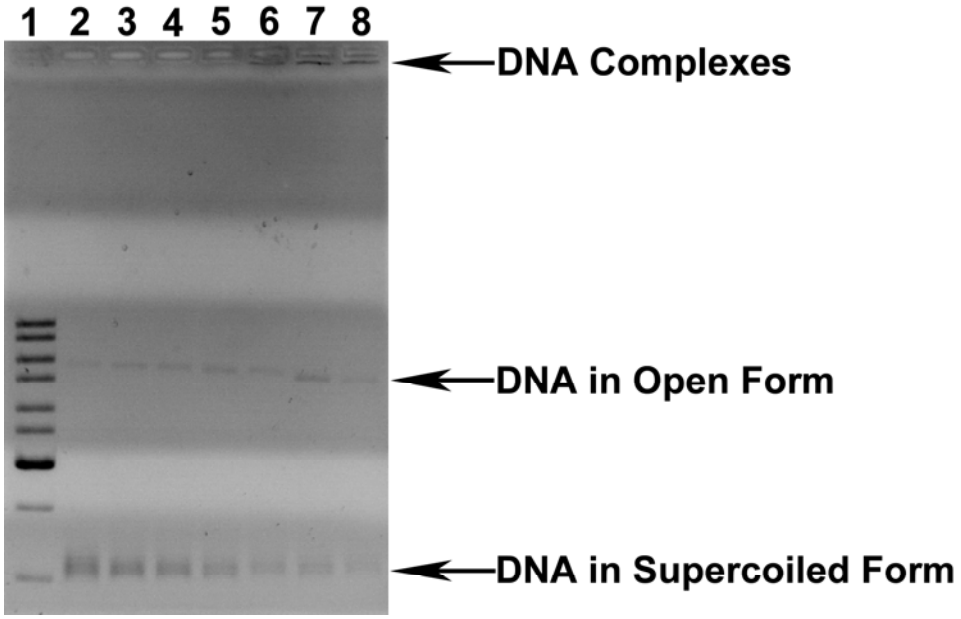

Figure 4.3.8. Agarose gel image of supercoiled pUC19 and its complexes. Lane 1: DNA ladder, lane 2: supercoiled pUC19, lane 3-8: complexes induced by supercoiled pUC19 and MV^{2+} at charge ratio of 2, 20, 50, 100, 200, 500. (direction of movement: downward)

Further, AFM was applied to visualize the morphology of the DNA complexes. The samples with charge ratio of 500 are selected since those are the complexes with largest size and biggest change in R_G/R_H ratio as compared to pure DNA. Figure 4.3.9 shows the images of the samples taken on standard 0.05% APTES modified mica. In all cases, similar so-called flower-like aggregates are observed. Evidently, upon complexation, the DNA molecules are released from their supercoiled form and few chains connect through one or multiple junctions (marked with arrows). This is in agreement with the increasing R_H, R_G and decreasing R_G/R_H from light scattering experiments. It confirms again that divalent counterions can induce association of DNA in aqueous solution at room temperature. The type of DNA shows almost no influence on the morphology of the complexes. Those so-called flower-like structures were also reported by other authors for the assemblies induced by either polymeric or multivalent counterions.[56,120, 143 , 144] However, this is the first time that such flower-like structures are reported for the complexes formed with divalent counterions.

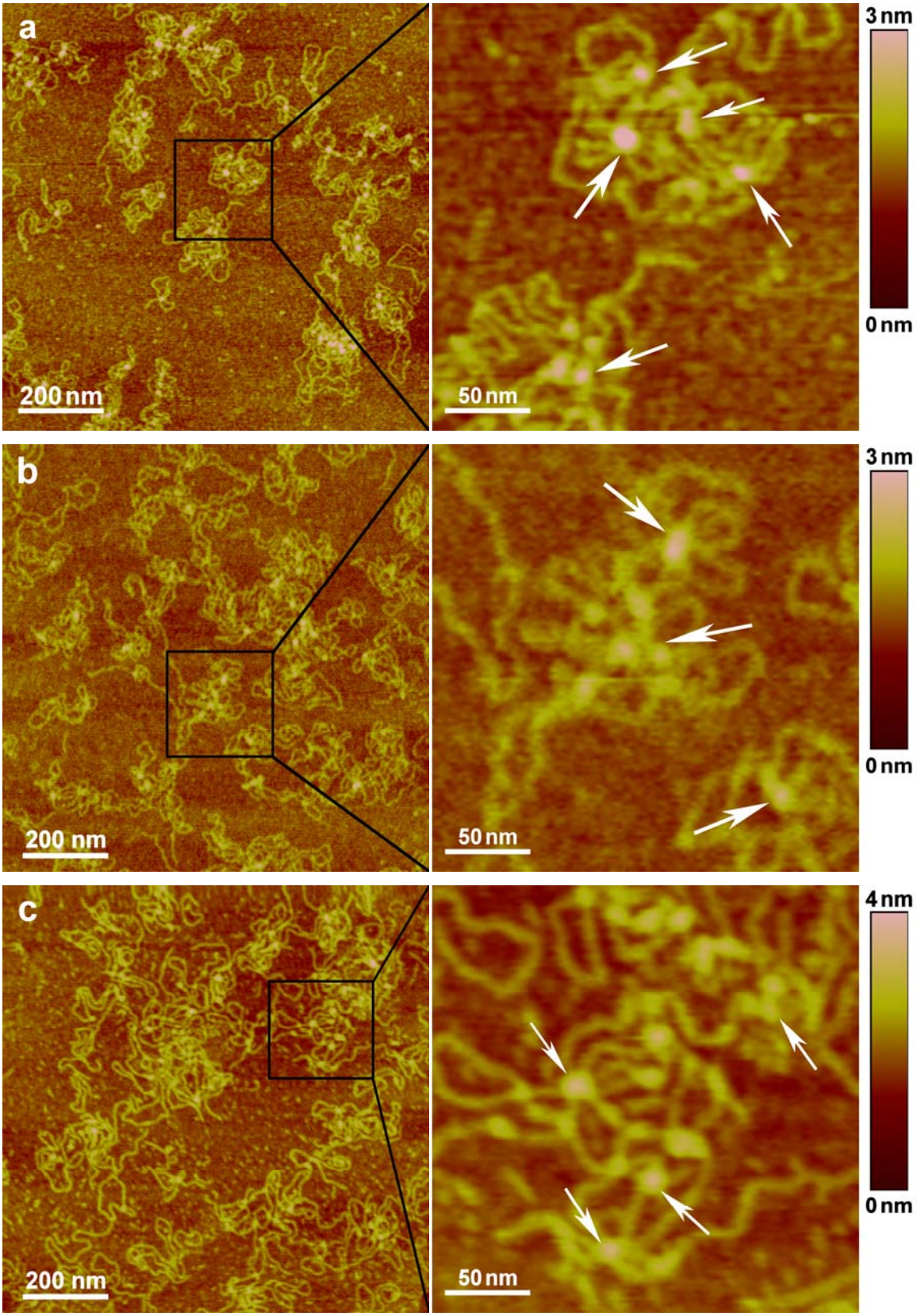
a
200 nm
50 nm
3 nm
0 nm
b
200 nm
50 nm
3 nm
0 nm
c
200 nm
50 nm
4 nm
0 nm

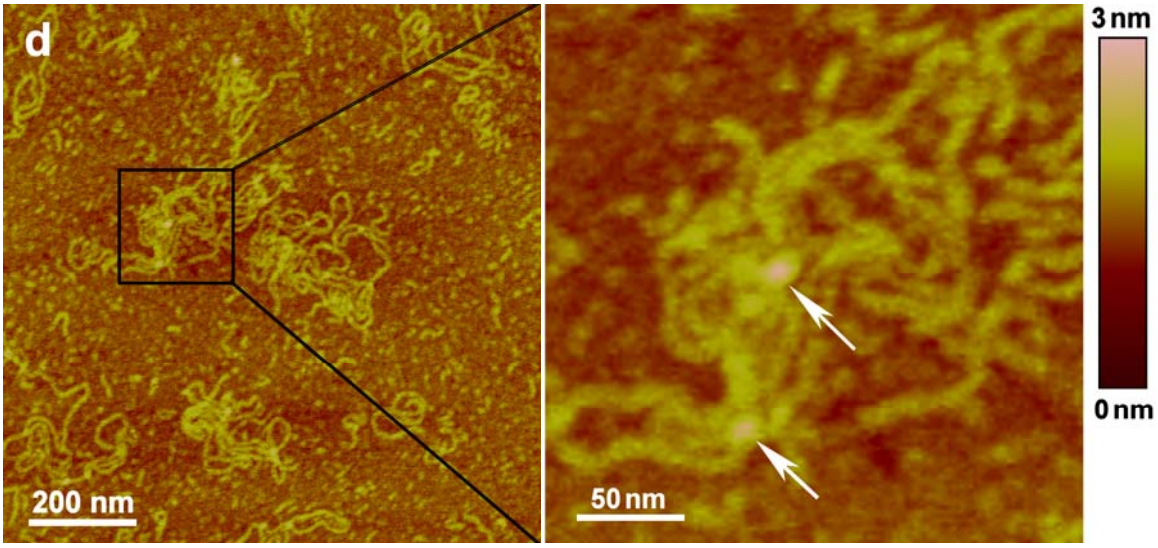

Figure 4.3.9. AFM images (left) of DNA complexes formed with: (a) supercoiled pUC19 and MV^{2+}, (b) supercoiled pUC19 and $C6D^{2+}$, (c) linear pUC19 and MV^{2+}, (d) linear pUC19 and $C6D^{2+}$; right images are zoomed from the black box in the left ones. (all: l = 500, c(DNA) = 0.01 gL^{-1} in TE buffer)

As mentioned above, the alternative method of immobilizing DNA molecules by divalent metal ions was also tested for those complexes for comparison. Figure 4.3.10 shows an AFM image of complexes formed by supercoiled pUC19 and MV^{2+} at charge ratio of 500 on bare mica, which is immobilized by Mg^{2+}. Despite of few flower-like aggregates, most of the molecules are separated and remained in open circle structure. On the one hand, the morphology of the complex induced by DNA and divalent counterion is confirmed to be flower-like by using this different method. On the other hand, a large amount of free DNA molecules is observed here. The reason for the free DNA might be that the immobilization process by divalent metal ion allows the complexes to disintegrate and then relax into open circle form when deposited on bare mica surface, which has already been observed for pure DNA molecule previously. From this experiment, it can be concluded that for imaging the assemblies induced by DNA and organic counterions, APTES modified mica seems to be a reliable substrate.

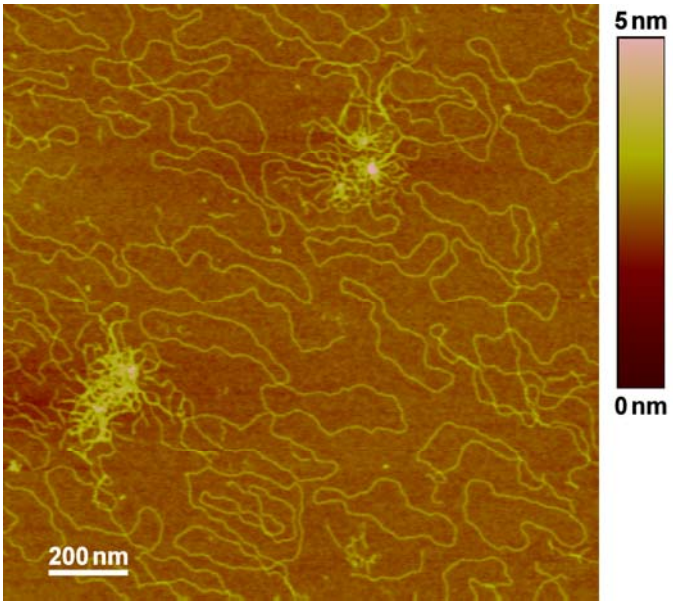

Figure 4.3.10. AFM image of assembly formed by supercoiled pUC19 and MV^{2+} at charge ratio l = 500 on bare mica; (c(DNA) = 0.01 gL^{-1} in TE buffer containing 5 mM $MgCl_2$)

The high concentration of counterions in the solution also raises the question whether the aggregation takes place due to the high ionic strength, which would be achieved by any monovalent salt, i.e. the so-called “salting out” effect. Further, it is of interest whether any divalent counterion can induce aggregation or this is some structure specificity. Therefore for comparison, the same amount of NaCl or $MgCl_2$ was added into the DNA solution to increase the ionic strength and reach the same charge ratio of l = 500. Furthermore, a mixture of MV^{2+} and $MgCl_2$ was also attempted to induce the association of DNA. The composition of MV^{2+} and Mg^{2+} was designed to achieve the charge ratio of PO_4^-:MV^{2+}:Mg^{2+} = 1:1:500. No complexes were detected either in light scattering or AFM measurements for all those systems. It is thus evident that the complexation of DNA induced by MV^{2+} and $C6D^{2+}$ is not a simple ionic strength effect or not a general consequence of neutralization of DNA strands by any divalent ions. Obviously, the structure of the divalent counterion with a separation of charges on the backbone is important for the formation of flower-like aggregates from multiple DNA molecules.

At this point, it is interesting how the counterions can induce aggregation at such high charge ratios only. It seems not possible that such large excess of ions binds to DNA. Thus analytical ultracentrifugation experiments were performed to determine the amount of counterions bound to DNA. Figure 4.3.11 shows the results for a sample of supercoiled pUC19 with MV^{2+} at charge ratio l = 10. The initial absorption at a certain wavelength can be separated into the contributions from DNA and counterion based on the spectra of sample and components. The value is compared with the absorption that the supernatant solution exhibits after the complex sedimented. As it is shown that (even unaggregated) DNA sediments at the rotation speed used for this analysis, the remaining absorption can be regarded as from the counterions only. Comparison yields the amount of non-sedimented counterions. Results in Figure 4.3.11 show that (90 ± 3) % of the MV^{2+} stay in solution, while only (10 ± 3) % sediment with the complex. Accordingly, for the sample with a charge ratio of 500, almost the total amount of counterions stays in solution and the fraction of sedimented species can just roughly be estimated as being a maximum of 1% of the total counterion amount. These results indicate that the association takes place up to about charge stoichiometry even at these extremely high loading ratios.

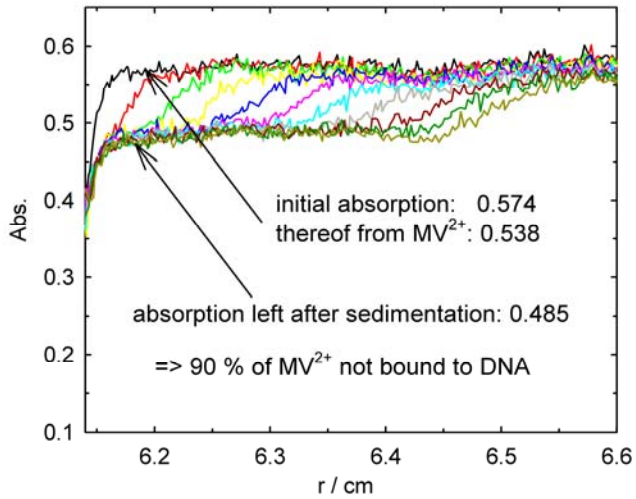

Figure 4.3.11. Analytical ultracentrifugation of a complex formed by supercoiled pUC19 and MV^{2+} at l = 10, sedimentation velocity run with rotation speed 20000 rpm, absorption scans for a

wavelength of 258 nm; (r : radius of the centrifuge. Error of absorption values from averaging a region of data points is ± 0.007)

The results described so far showed that in TE buffer solution, the divalent counterions MV^{2+} and $C6D^{2+}$ can only induce aggregation of DNA at charge ratio $l \geq 50$ and flower-like assemblies are observed for the samples at charge ratio l = 500 for both counterions. However, to further elucidate the influence of additional salt (buffer ions), the complexation of DNA with different divalent counterions was also carried out in salt free aqueous solution. Figure 4.3.12 presents examples of detailed DLS and SLS data for complexes produced by supercoiled pUC19 and MV^{2+} in salt free solution. It is clear that with increasing charge ratios, the polydispersity of the assemblies increases, which is similar to that of supercoiled DNA complexes in TE buffer (Figure 4.3.12a). In SLS, all the data are fitted by Zimm plot (Figure 4.3.12b). It is found again that at charge ratio $l \leq 50$, even thought the radius of gyration of the samples decreases, almost on changes in the molecular weight of the particles is observed, which suggests no aggregates are formed. Increase of molecular weight is only obtained at higher charge ratios where the size of the complexes increases in both DLS and SLS.

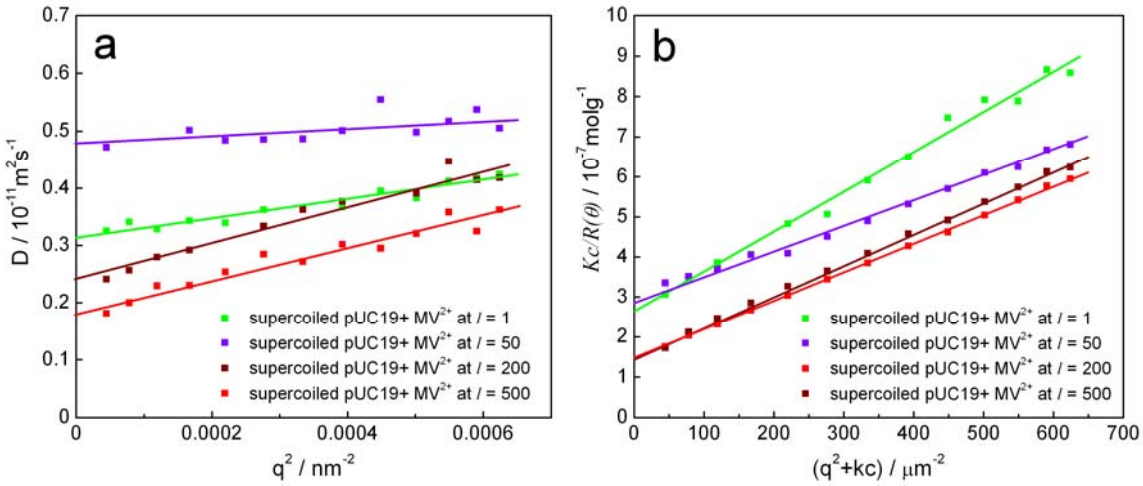

Figure 4.3.12. (a) Diffusion coefficient and (b) $Kc/R(\theta)$ as a function of scattering vector square for assemblies formed with supercoiled pUC19 and MV^{2+} at different charge ratios; (all: c(DNA) = 0.01 gL^{-1} in MQ water)

The changes of the size of the aggregates formed with supercoiled pUC19 and different counterions are illustrated more clearly in Figure 4.3.13. Both R_H and R_G show a decrease with increasing charge ratio first at charge ratio of 20 to 50, the complexes reach a minimum size close to that of pure supercoiled pUC19. When the size of the complexes reaches a minimum, addition of more counterions causes an increase in both R_H and R_G. These curves show that there may be two "binding steps" in the complexation process in salt free solution: before the counterions are added, there is no additional salt in the solution so that the repulsive force from each segment of one DNA molecule makes the total persistence length relatively large.[145] Adding counterions screens the phosphate groups somewhat and thereby reduces the repulsive force between DNA segments. This causes the decrease of hydrodynamic radius and radius of gyration. At this stage, the counterions act like low molecular mass salt and no aggregation occurs. When the amount of counterions is further increased, the repulsive forces between different DNA molecules are overcame so that the divalent counterions bridge multiple DNA molecules and larger complexes consisting of multiple DNA molecules are formed, which is evident from increasing size (R_H and R_G) and increasing molecular weight discussed above.

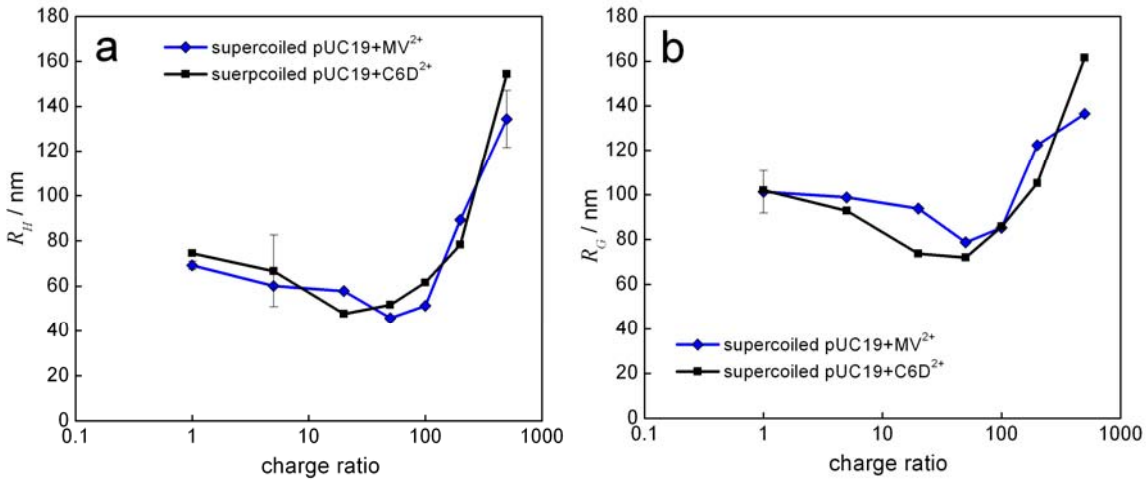

Figure 4.3.13. Hydrodynamic radius (a) and radius of gyration (b) of complexes induced by supercoiled pUC19 and different divalent counterions. (all: c(DNA) = 0.01 gL^{-1} in MQ water)

The characteristic R_G/R_H ratio of those samples is shown in Figure 4.3.14. In salt free solution, the aggregation of DNA and counterions exhibits slightly different behavior as compared to that in TE buffer: R_G/R_H ratio shows a slight increase up to charge ratio of 50, for both MV^{2+} and $C6D^{2+}$. The maximum R_G/R_H ratio for assemblies induced by MV^{2+} is 1.72 at charge ratio l = 50, and that for DNA/$C6D^{2+}$ complexes reaches 1.55 at l = 20. Those values are close to the characteristic ratio for supercoiled pUC19 in TE buffer mentioned before. A major decrease is observed at high charge ratios (l ≥ 50) where the lowest value is R_G/R_H = 1 at l = 500. It means that even in salt free solution, the assemblies induced by sufficient amount of divalent counterions have a similar morphology compared to those formed in TE buffer. Absence of low molecular weight salt does not influence the complex formation substantially. This is consistent with the results mentioned above, as the excess of free counterions that became evident from analytical ultracentrifugation causes a similar screening effect as added salt. Thus effectively a complex with a ratio of l = 500 is not in salt-free solution but in salt containing solution due to the additional counterions already.

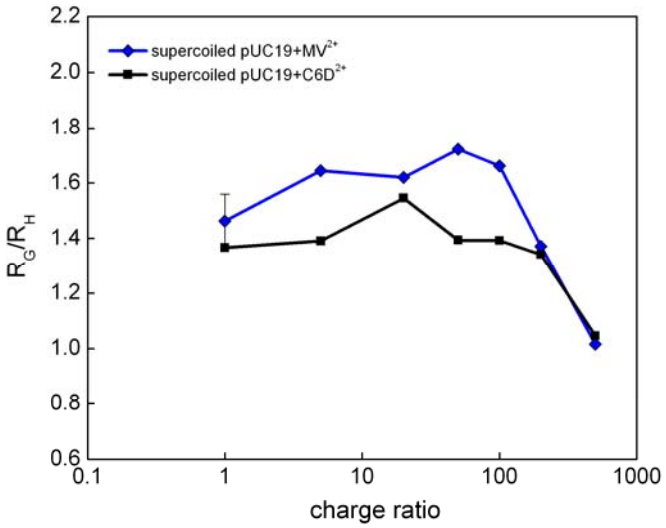

Figure 4.3.14. Characteristic R_G/R_H ratio of assemblies formed by supercoiled pUC19 and different divalent counterions. (all: c(DNA) = 0.01 gL^{-1} in MQ water)

Further, AFM measurements were also performed to investigate the morphology of the complexes formed in salt free solution. One sample is the complex

associated by supercoiled pUC19 and MV^{2+} at charge ratio of 50, which has the maximum R_G/R_H ratio of 1.72. Figure 4.3.15 exhibits the AFM image of this sample taken on APTES modified mica. It is evident that all the molecules are in supercoiled form, very similar to the pure DNA molecule. It is consistent with the results from light scattering experiments. However, some differences are found: the average length of the supercoiled molecules is around (0.19 ± 0.04) μm, which is much smaller than supercoiled DNA (0.46 ± 0.02) μm. The average height is (1.9 ± 0.2) nm, which is higher than that of supercoiled DNA (1.5 ± 0.39) nm. This is a hint that those supercoiled molecules are more condensed than normal supercoiled pUC19 in TE buffer.

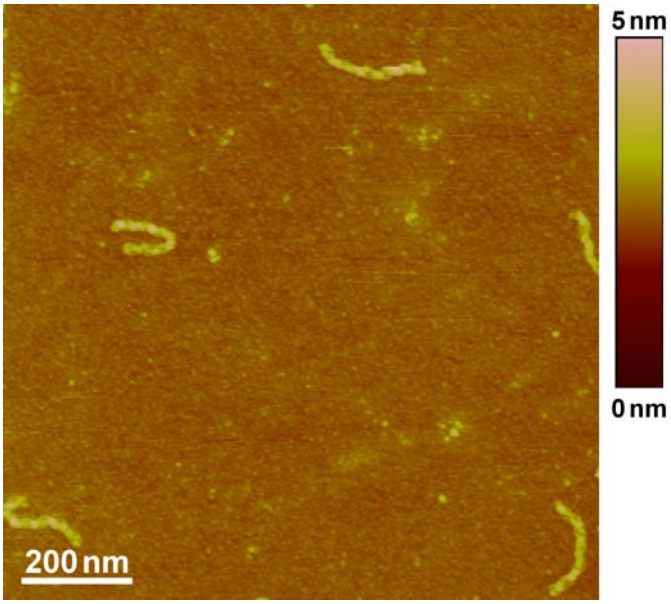

Figure 4.3.15. AFM image of a sample formed with supercoiled pUC19 and MV^{2+} at charge ratio of 50 in MQ water

Figure 4.3.16 presents a magnified image of the sample in Figure 4.3.15. Both of the molecules shown in the image are shorter than normal supercoiled DNA. From the section analysis plot, two separated supercoiled DNA strands can be distinguished. It is obvious that although those particles are still in supercoiled form, part or even half of the molecules are merged together through counterions. It shows again that MV^{2+} has stronger ability to condense DNA

strands than normal low molecular weight salt, such as NaCl. The supercoiled molecule observed here thus is not a simple supercoiled DNA strands, but a condensate of individual DNA strands with counterions.

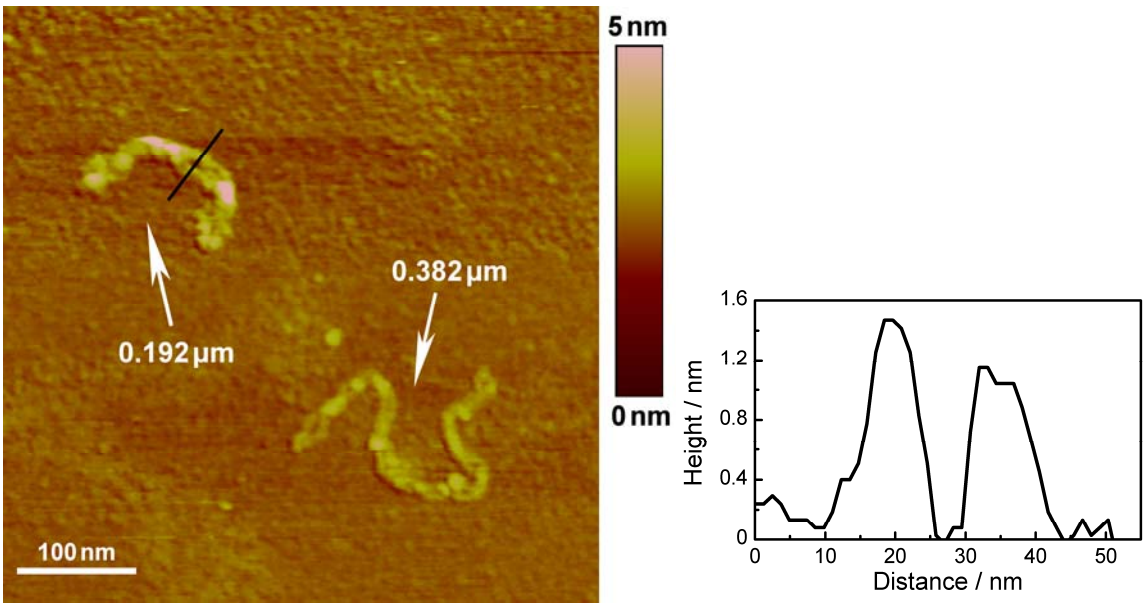

Figure 4.3.16. Magnified AFM image of the sample induced by supercoiled pUC19 and MV^{2+} at charge ratio of 50 in MQ water (left) and the section analysis plot of the indicated line (right)

A further sample studied by AFM is the complex formed with supercoiled pUC19 and MV^{2+} at charge ratio l = 500, which has the lowest R_G/R_H ratio and thus the most compact structure. Similar flower-like aggregates are also observed in Figure 4.3.17 as obtained in TE buffer. All those AFM measurements not only reveal the morphologies of the complexes in salt free solution, but also are in agreement with light scattering results.

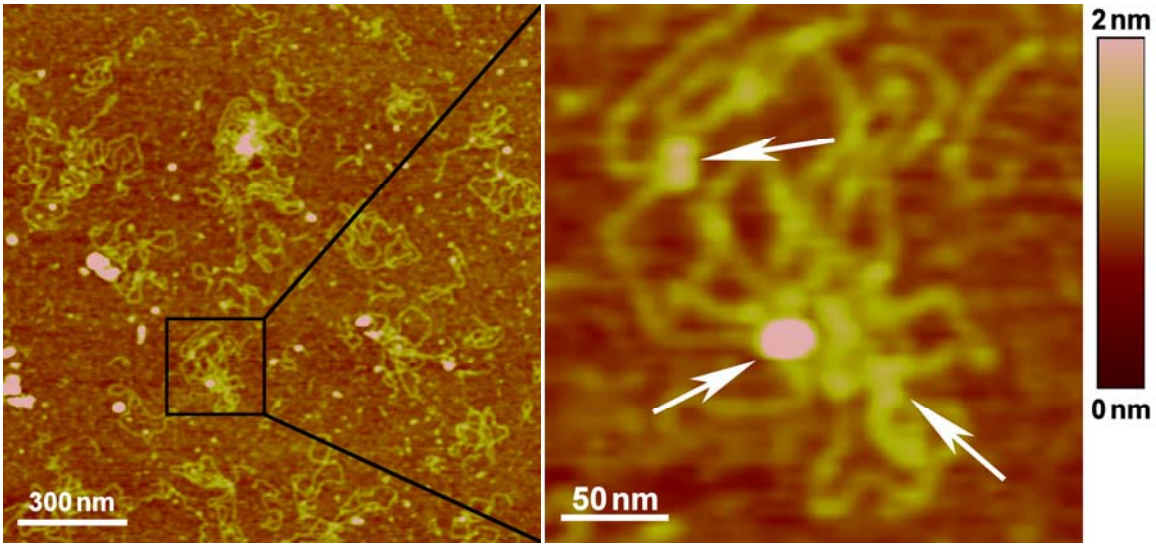

Figure 4.3.17. AFM image (left) of complexes associated by supercoiled pUC19 and MV^{2+} at charge ratio of 500 in MQ water; right image is zoomed from the black box in the left one

4.4 Association of DNA with Tetravalent Counterions

4.4.1 Association of DNA with $C6T^{4+}$

Figure 4.4.1.1 shows the light scattering results for the DNA/$C6T^{4+}$ system. First, aggregation is evident at a charge ratio of about 1 to 1.5, i.e. at much lower charge ratios than with divalent counterions. The hydrodynamic radius starts to increase at l = 1 for supercoiled DNA complexes and l = 1.5 for linear DNA complexes (Figure 4.4.1.1a). At charge ratio l = 3, R_H reaches around 102 nm for supercoiled DNA assemblies and 150 nm for linear DNA assemblies. The DLS results strongly indicate the higher efficiency of tetravalent counterion in complexation with DNA due to multiple valences. The difference between supercoiled and linear pUC19 is even more pronounced in SLS (Figure 4.4.1.1b). The radius of gyration does not increase for supercoiled DNA aggregates until R_H increases, while R_G for the linear DNA complexes goes through a minimum around 97 nm at charge ratio l = 1.5, then R_G increases with increasing charge ratio. This is as the similar behavior observed already for divalent counterions.

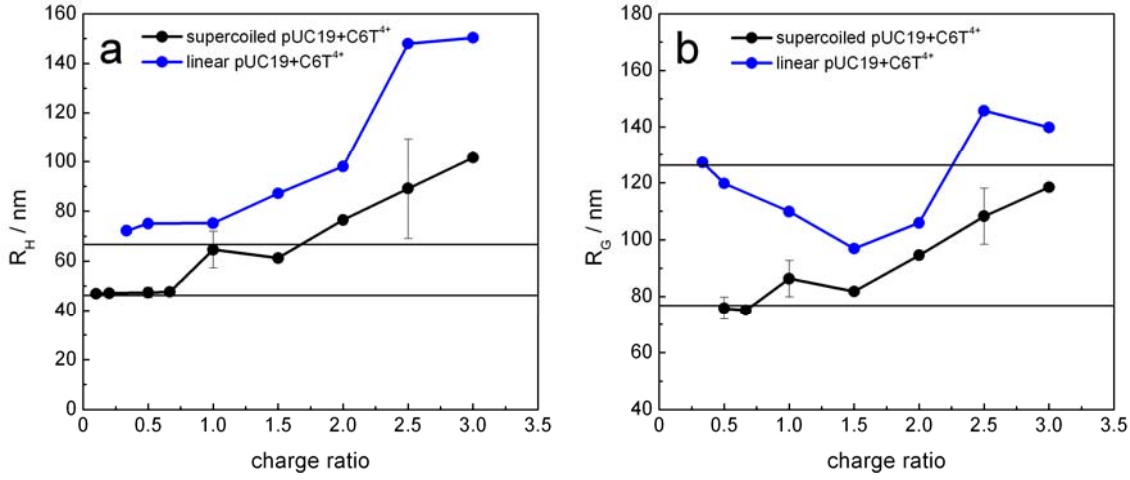

Figure 4.4.1.1. (a) Hydrodynamic radius and (b) radius of gyration of complexes formed by supercoiled and linear pUC19 with tetravalent counterion $C6T^{4+}$; horizontal lines: pure

supercoiled pUC19 (lower liner) and linear pUC19 (upper line). (all: c(DNA) = 0.01 gL^{-1} in TE buffer)

In Figure 4.4.1.2a the characteristic ratio R_G/R_H shows a continuous decrease for both types of DNA complexes. However, the decrease of the R_G/R_H ratio for aggregates induced by supercoiled pUC19 is significantly smaller above charge ratio l = 1.5. It reaches a minimum value of about R_G/R_H = 1.16 at charge ratio l = 3, which is comparable to the values obtained from complexes induced by divalent counterions at charge ratio l = 500. It implies that the complex of supercoiled pUC19 and C6T^{4+} at charge ratio of 3 has a similar structure as those induced by divalent counterions at charge ratios l = 500. For the complex formed by linear pUC19 and C6T^{4+} at charge ratio l = 3, the R_G/R_H ratio decreases to 0.9. The difference is evident more obviously in the relative scattering intensity (Figure 4.4.1.2b). For supercoiled DNA, the scattering intensity continuously increases, which is expected due to the aggregation of multiple molecules. For linear DNA complexes, the intensity first increases at charge ratio of 2, it reaches approximately same value as compared to that of supercoiled DNA complex at charge ratio of 3 (around 2). Considering the fact that at l = 2 the R_G/R_H ratio for the linear DNA aggregate (1.08) is close to that of supercoiled DNA complex (1.16) at l = 3, the observation in scattering intensity strongly supports the assumption that a similar supramolecular structure is obtained for the supercoiled DNA assembly at l = 3 and the linear DNA at l = 2. When the charge ratio is further increased for the linear DNA complex, a dramatic increase in scattering intensity is observed, which corresponds to the further decrease in R_G/R_H ratio. The scattering intensity of the complexes induced by supercoiled and linear pUC19 at charge ratio l = 3 is 1.86 and 7.43, respectively. The corresponding radius of gyration of those assemblies is R_G = 118 nm (supercoiled DNA) and R_G = 140 nm (linear DNA). These results can be compared to the change in scattering intensity. It is calculated that at charge ratio l = 3, the R_G^6 of the linear DNA aggregate ($7.53 \cdot 10^{12}$ nm^6) is 2.8 times higher than that of supercoiled DNA ($2.7 \cdot 10^{12}$ nm^6). However, the scattering intensity of

linear DNA complex is 4 times higher than that of supercoiled DNA at same charge ratio. This result thus suggests that the abrupt increase of scattering intensity here, in addition to the size increase, may be due to an increase in internal density of the assemblies. It indicates that more condensed or compact particles are obtained at charge ratios l = 3. By combining the results from R_G/R_H and the scattering intensity, even taking possible polydispersity effects into account, it is evident that more compact complexes are formed from linear DNA with a charge ratio l > 2. This shows a strong influence of the type of DNA on the morphology of the complexes.

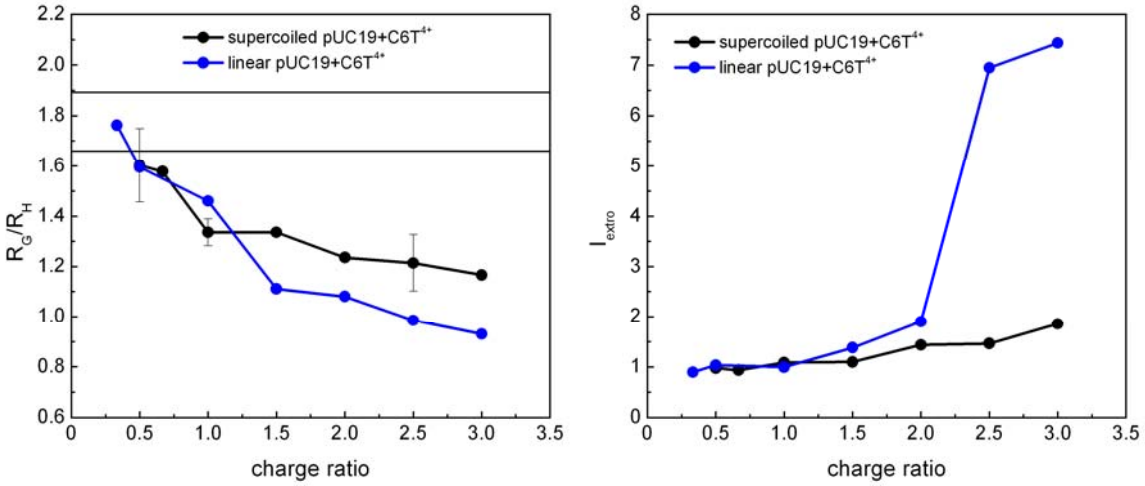

Figure.4.4.1.2. (a) R_G/R_H ratio and (b) relative scattering intensity for complexes induced by supercoiled and linear pUC19 with tetravalent counterion $C6T^{4+}$; horizontal lines: pure supercoiled pUC19 (lower liner) and linear pUC19 (upper line). (all: c(DNA) = 0.01 gL^{-1} in TE buffer)

In order to further prove the influence of DNA type on complex morphology, AFM was again performed complementary to light scattering measurements. Results of complexes formed at charge ratio 3 with different types of DNA are shown in Figure 4.4.1.3. Flower-like aggregates are observed for supercoiled DNA (Figure 4.4.1.3a, b). It is consistent with the results obtained for DNA/divalent counterion assemblies, as described previously. More compact structures in form of rods and toroids are found for the assemblies induced by linear DNA (Figure 4.4.1.3c, d). However it shows that this sample is in the transition stage

since few flower-like aggregates can still be seen in the image. The average height of the rod-like and toroid-like molecules is (2.46 ± 0.4) nm and (2.79 ± 0.92) nm, respectively, which is higher than the single linear DNA molecules. It is obvious that those species are in more compact form compared to flower-like aggregates. This is also in agreement with the intensity results in light scattering. Therefore, the AFM results support that the type of DNA significantly influences the morphology of the aggregates when complexation is induced by $C6T^{4+}$. A possible explanation for these results is that linear pUC19 has a more open structure than supercoiled one, so that it could cause less steric hindrance for different DNA molecules to mutually interact at multiple sites. This effect may only play a role for tetravalent ions that act as “stronger linkers” than divalent ions. It also shows the efficiency difference between divalent and tetravalent counterions.

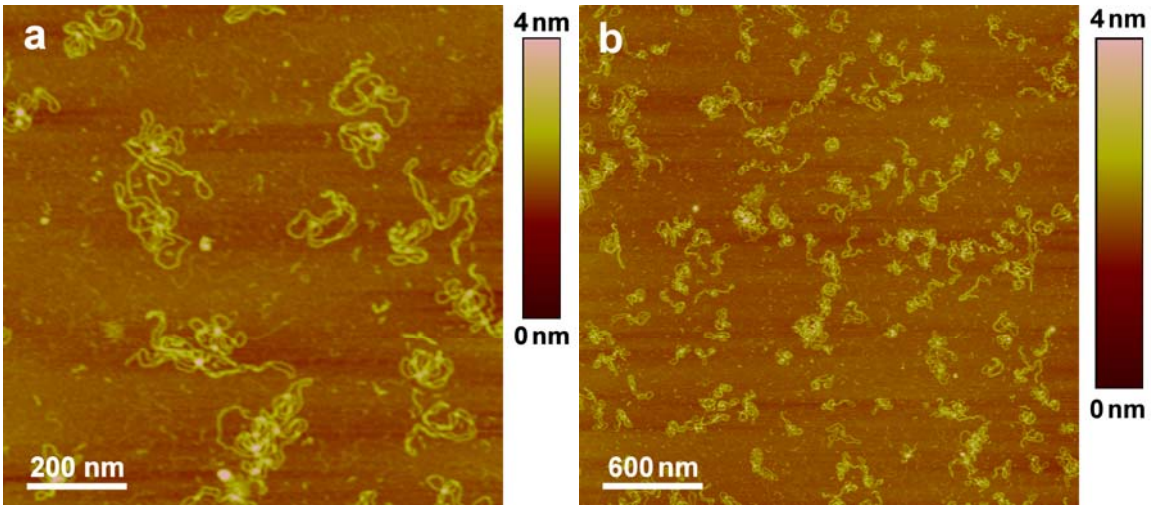

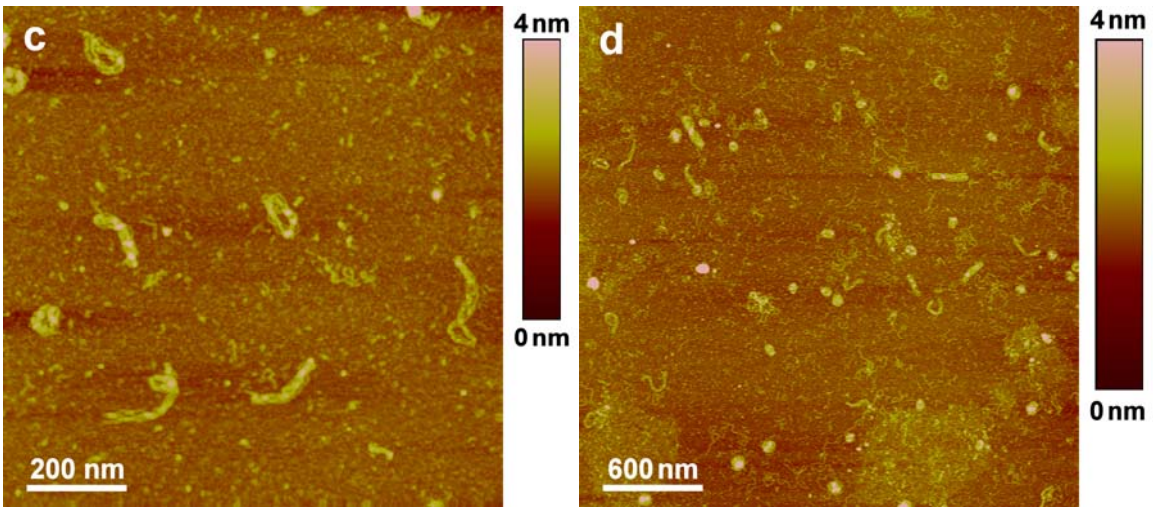

Figure 4.4.1.3. AFM images of assemblies induced by C6T^{4+} with supercoiled pUC19 (a, b) or linear pUC19 (c, d) at charge ratio of 3. (all: c(DNA) = 0.01 gL^{-1} in TE buffer)

Compared to the divalent counterions, the tetravalent counterion C6T^{4+} causes aggregation of DNA at much lower charge ratios in TE buffer solution. The type of DNA exhibits significant influence on the resulting complex morphology. In a comparable experiment, the association of supercoiled pUC19 and C6T^{4+} was also carried out in salt free solution (no additional added low molecular mass salt except original counterions). Figure 4.4.1.4 shows the light scattering results of those samples. Similar to the behavior observed for divalent counterions, both R_H and R_G go through a minimum first, then increase with increasing charge ratio. In consistence with the fact that the higher valence ion exhibits stronger screening and connection ability, the location of the minimum for DNA/C6T^{4+} system is at much smaller charge ratio as compared to the DNA/divalent counterion system. At a charge ratio of 3, the corresponding minimum values are R_H = 47 nm, R_G = 45 nm and R_G/R_H = 0.96. It indicates that the function of C6T^{4+} is more than the one of low molecular weight salt or divalent counterions MV^{2+} and C6D^{2+}. When the tetravalent counterion reduces the size of DNA molecules by screening the negative charges, it also induces the DNA molecules to form more compact structures. In contrast, the morphology of DNA/divalent counterion aggregates does not change significantly with the size reduction in the salt-free solution. This shows an important difference between tetravalent and divalent counterions.

Furthermore, adding more tetravalent counterion, i.e. increasing the charge ratio, the size of the complex increases while the R_G/R_H ratio increases as well. It implies that a higher charge ratio causes a larger complex size but possibly a looser structure. This is specific for salt-free solution.

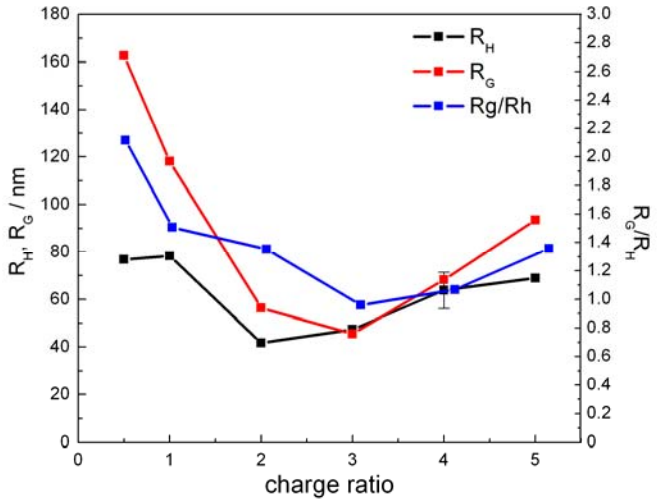

Figure 4.4.1.4. Light scattering results of complexes induced by supercoiled pUC19 and tetravalent counterion C6T^{4+} in MQ water

Likewise, the stability of the assemblies induced by tetravalent counterions C6T^{4+} in MQ water was also investigated. For complexes formed at either charge ratio of 2 (Figure 4.4.1.5a) or charge ratio of 3 (Figure 4.4.1.5b), both hydrodynamic radius, radius of gyration and R_G/R_H ratio keep constant over 40 days. It is evident that in salt free solution, the complexes induced by C6T^{4+} are stable both in size and structure over a month.

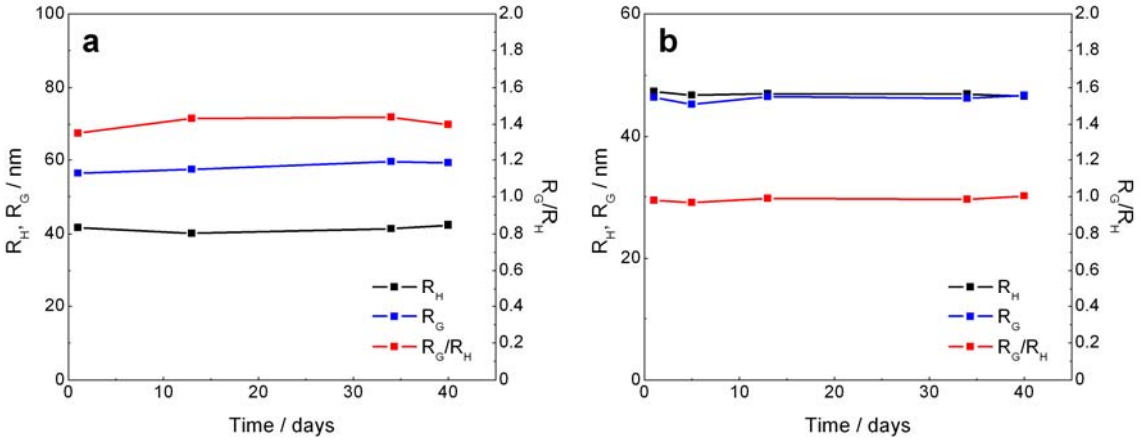

Figure 4.4.1.5. Stability of complexes associated with supercoiled pUC19 and C6T^{4+} at (a) charge ratio of 2 and (b) charge ratio of 3. (all: c(DNA) = 0.01 gL^{-1} in MQ water)

It is of fundamental interest whether the observed structures are kinetically controlled and depend on the preparation procedure or thermodynamically controlled and represent the equilibrium structures, which usually means the same structure can be obtained via different preparation routes. Complexes of two oppositely charged polyelectrolytes usually represent kinetically trapped structures due to the high number of charges.[120, 146] In contrast, recently described dendrimer-dye assemblies were shown to be equilibrium structures.[21,24] Thus the influence of sample preparation is highly interesting. We therefore prepared samples using two different mixing orders, that is adding DNA into counterion solution or adding counterion into DNA solution. For the divalent counterions and for C6T^{4+}, both in the TE buffer and MQ-water, changing the order does not give different light scattering results in terms of R_H, R_G, and R_G/R_H ratio. Thus the structures induced by these counterions are likely thermodynamically controlled and can be regarded as equilibrium structures.

4.4.2 Association of DNA with PSPDI

As mentioned in the introduction, to investigate a stiff multivalent counterion but avoid intercalation of counterions into the DNA double helix structure, a water

soluble perylene dye with bulky groups surrounding the aromatic system was chosen to associate with DNA. The molecular structure of this chromophore is illustrated in Figure 4.4.2.1 (top). It demonstrates that the diisopropylphenyl groups at the head and the pyridinium groups at the side are all perpendicular to the center perylene system, which brings a big steric hindrance to prevent the dye molecule to intercalate into DNA helix. The distance of the closest charges is between (0.51 ~ 0.54) nm, fits the distance of adjacent phosphate groups along DNA stand (0.547 nm). The geometric design of this dye molecule might thus cause a different structure when associating with DNA molecules as other tetravalent counterions.

PSPDI is a fluorescent dye, its UV-Vis absorption spectrum is shown in Figure 4.4.2.1 (bottom). In the wavelength range between 300 nm to 800 nm, two major peaks are observed. One is located at wavelength of 548 nm, the other at a wavelength of 427 nm. The absorption property of this dye gives opportunities to investigate the complexation behavior with DNA via UV-Vis spectroscopy. However, a weak absorption can still be seen in the wavelength range of 600 nm to 800 nm, which causes a fluorescence effect when a red laser with wavelength of 632.8 nm is applied for this dye in light scattering. Therefore, an infrared laser with a wavelength of 831.5 nm was used to investigate the aggregates formed with this dye by light scattering.

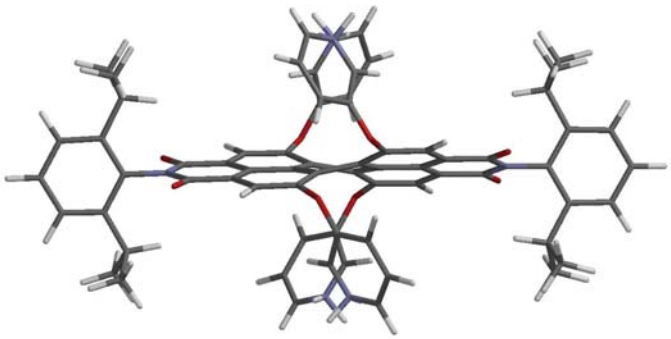

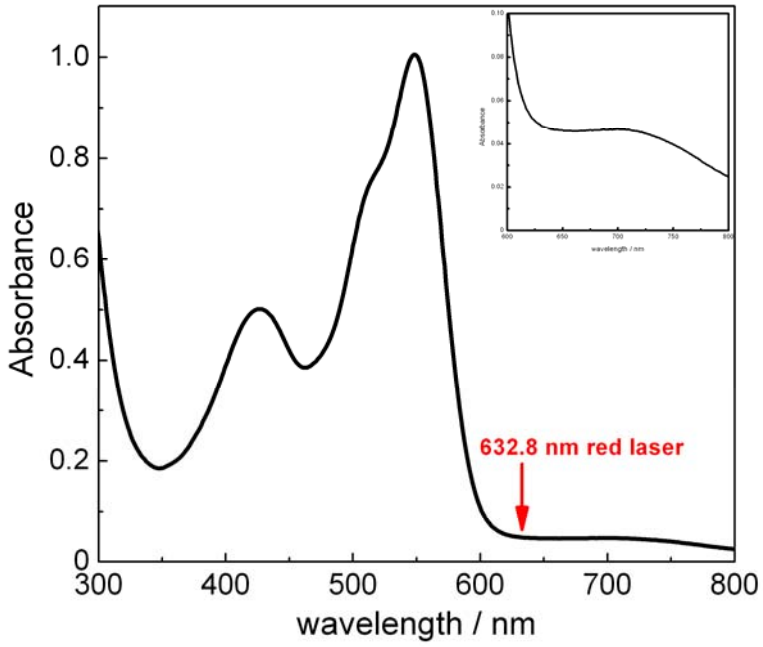

Figure 4.4.2.1. Molecular structure (top) and UV-Vis absorption spectrum (bottom) of PSPDI

The spectra of PSPDI titrated with supercoiled pUC19 are shown in Figure 4.4.2.2. With increasing amount of DNA, the absorption peak shifts to longer wavelength from 548 nm to 553 nm. The intensity of the absorption maxima decreases with addition of DNA till c(DNA) ≈ 2.5 mgL^{-1} and then the intensity of the red shifted peak increases again with further DNA addition (Figure 4.4.2.2b). The maximum hypochromicity is around 44%. Furthermore, no characteristic isosbestic point is observed in Figure 4.4.2.2a. All those phenomena indicate that the system cannot be described by a simple equilibrium of two spectroscopically distinguishable species, as it is often the case for dye molecules binding to polyelectrolytes where monomeric and (bound) stacked dye molecules are in equilibrium.[147,148] The observed behavior is also in difference to UV-Vis results with meso-tetrakis(4-*N*-methylpyridiumyl) porphyrin (TMPyP) that interacts with DNA by intercalation[149,150] and rather in similarity with meso-tetrakis(4-(*N*-tri-methylammonium)phenyl) porphyrin (TAPP)[151,152] or meso-tetrakis(4-*N*-ethyl-pyridiumyl) porphyrin (TEPyP)[153] that binds outside on the DNA surface. However, no indication for self-stacking is observed with PSPDI. Thus no mutual π-π interaction is induced when the PSPDI binds to DNA, as expected

due to the molecule geometry with the bulky groups surrounding the aromatic system. This steric hindrance should also prevent the dye molecules to intercalate into DNA double helix, which is desired initially. The decrease in absorbance may be simply due to the interaction with DNA, which thereby causes changes in the polarity surrounding the PSPDI. The increase in the intensity of the red shifted peak might indicate structural changes of the complexes with further addition of DNA.[151,154]

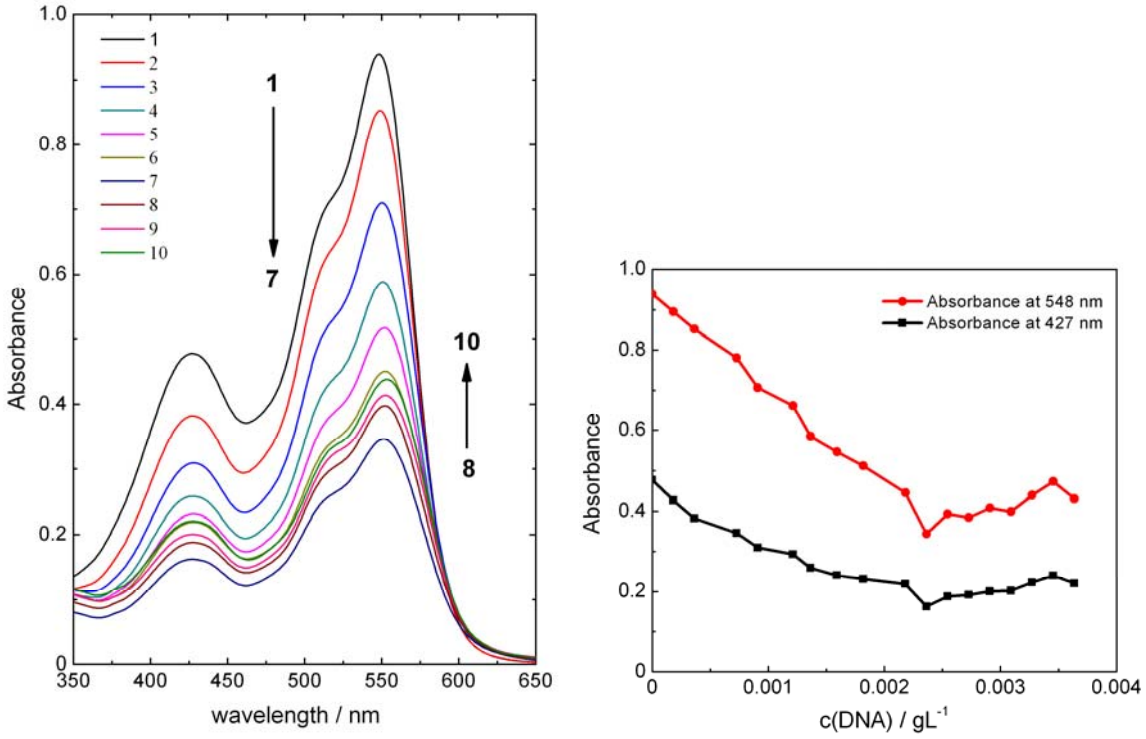

Figure 4.4.2.2. (a) UV-Vis absorbance spectra of PSPDI titrated with supercoiled pUC19 in TE buffer and (b) absorbance as a function of DNA concentration. The concentration of PSPDI in titration was 3.1 μM. The concentration of DNA from 1 to 10 was 0, 0.4, 1, 1.5, 2, 2.4, 2.6, 2.8, 3.2 and 4 mgL^{-1}

Light scattering results obtained with the infrared laser setup are shown in Figure 4.4.2.3. As opposed to the systems discussed so far, two diffusion processes are observed with this counterion in certain regimes. Figure 4.4.2.3a shows typical electric field autocorrelation functions and relaxation times distributions for samples with different charge ratios. Two separated peaks are

present for the complex induced at a charge ratio of 1.5, while a monomodel distribution is found for a lower charge ratio sample (l = 0.5). The diffusion coefficient as a function of scattering vector for the sample with charge ratio l = 0.5 is presented in Figure 4.4.2.3b. The peak at slower decay time generates an apparent diffusion coefficient of $1.7 \cdot 10^{-12}$ m^2s^{-1} and thus a hydrodynamic radius of 23 nm, while the other distribution at faster decay time yields a D_{app} of $9.2 \cdot 10^{-12}$ m^2s^{-1} and a R_H of around 126 nm. Figure 4.4.2.3c exhibits relaxation rate as a function of scattering vector. It is obvious that the curves from both distributions go through the original point, which indicates that both processes are contributed from translational motion.[126,155] Systematic results for assemblies formed with both supercoiled and linear pUC19 are displayed in Figure 4.4.2.3d. Both systems show only one process for charge ratio $l \leq 1$. In this regime, the size of the complexes decreases with increasing charge ratio. In contrast, above charge ratio 1, two processes are detected. One corresponds to a size between 20 nm to 30 nm and does not show significant changes with increasing charge ratio. The other process gives an increasing R_H with increasing charge ratio up to $R_H \approx$ 140 nm. It needs to be mentioned here that in some case the peaks in bimodal distribution are very close to each other so that it is difficult to determine quantitative values for the radii, but it is clearly proven that two diffusive processes occur for those samples.

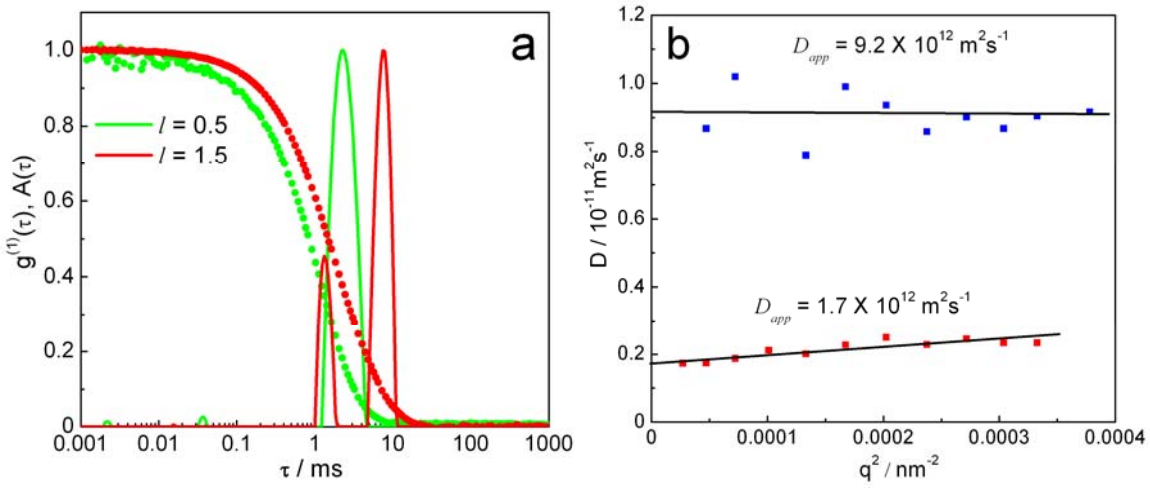

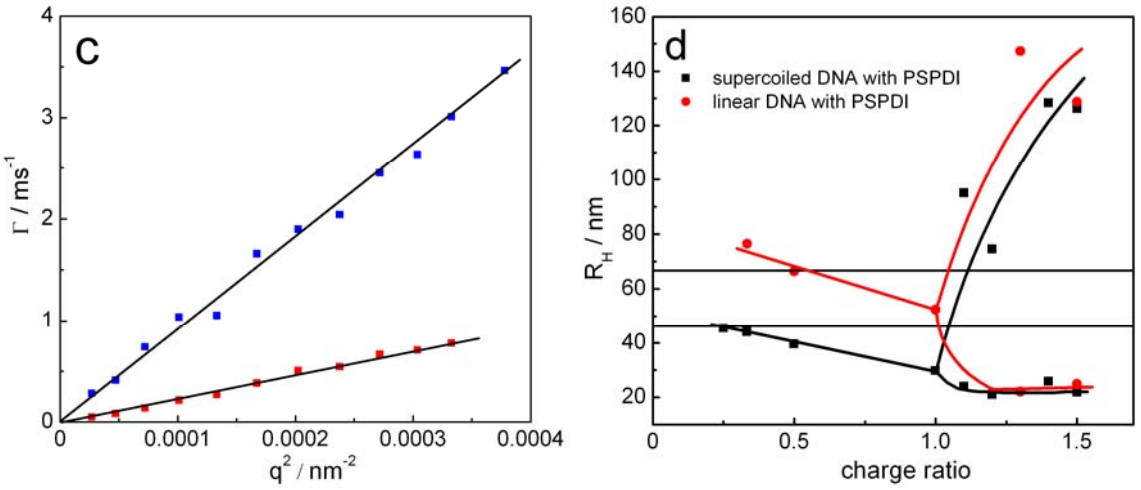

Figure 4.4.2.3. (a) Normalized electric filed autocorrelation functions and relaxation times distributions at a scattering angle of 50° of complexes induced by supercoiled pUC19 and PSPDI; (b) diffusion coefficient and (c) relaxation rate as a function of scattering vector square for supercoiled pUC19/PSPDI complex at charge ratio of 1.5; (d) hydrodynamic radius of assemblies formed with supercoiled or linear pUC19 and PSPDI; horizontal lines: pure supercoiled pUC19 (lower liner) and linear pUC19 (upper line); (all: c(DNA) = 0.01 gL^{-1} in TE buffer)

The first question that arises is for the cause of those bimodal distributions. Usually two processes are observed either in polyelectrolyte solutions due to polyelectrolyte effects or because of two species with different size. The polyelectrolyte effects can be eliminated by adding a sufficient amount of low molecular mass salt to screen the charges. As discussed in Chapter 4.2, experiments are already performed in ionic buffer solution so that no polyelectrolyte effects should be expected (λ = c(PO_4^-)/c(buffer) = 0.0031). However, in order to ensure the formation of two species, additional NaCl, varying the concentration from 0.01 mM to 1 mM, was added into the complex solution. Bimodal distributions are always observed in light scattering measurements (Figure 4.4.2.4). This strongly supports the conclusion that there are in fact two species in the solution, and the bimodal distributions in light scattering are caused by the size difference of those species.

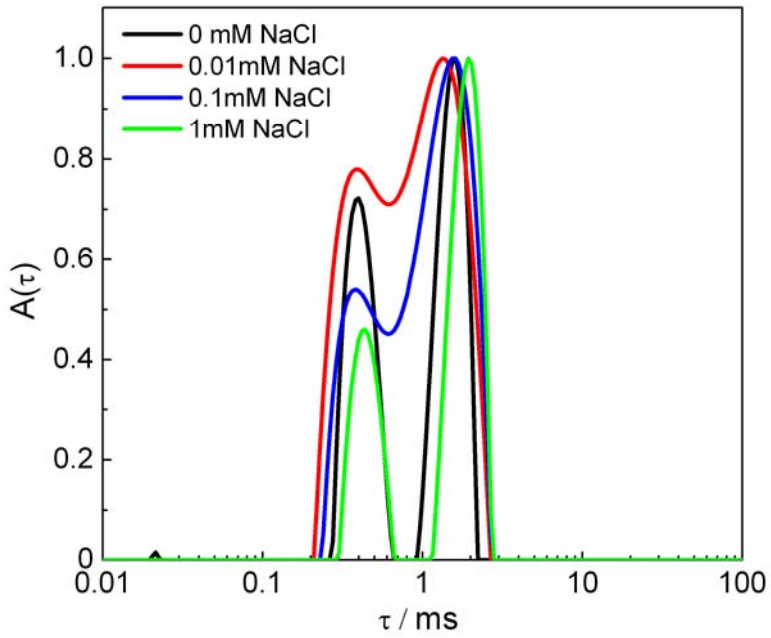

Figure 4.4.2.4. Relaxation time distributions of aggregates formed with supercoiled pUC19 and PSPDI with additional NaCl; (all: c(DNA) = 0.01 gL^{-1} in TE buffer)

The second question thus is what the two species are. AFM measurements provide further insight. Figure 4.4.2.5-4.4.2.6 present a series of AFM images of complexes induced by PSPDI at different charge ratios with both DNA types. Figure 4.4.2.5-4.4.2.6 (a, b) show that at low charge ratio l = 0.5 where only one process is obtained in light scattering, only flower-like aggregates are found. This is similar to other complexes in this study. When the charge ratio is increased to l = 1, as seen in Figure 4.4.2.5-4.4.2.6 (c, d), rod-like, flower-like and few toroid-like aggregates are observed in coexistence. At charge ratio of 1.4~1.5, where bimodal distributions are detected in light scattering, only rod and toroid structures are found and no flower-like aggregates (Figure 4.4.2.5-4.4.2.6 e, f). Rods and toroids have well-defined dimensions: for the rod structure, the images yield an average length of (190 ± 50) nm for supercoiled DNA samples and (200 ± 80) nm for linear DNA ones. For the toroid, an average diameter of (55 ± 8) nm for supercoiled DNA complexes and (60 ± 10) nm for linear DNA ones are obtained. Those results are consistent with the R_H and the bimodal distribution resulting from DLS. On the other hand, rods and toroids have a higher height

than that of only DNA strands: rod structures yield an average height of (2.9 ± 0.3) nm for supercoiled DNA and (2.0 ± 0.4) nm for linear DNA, toroids have a height of (3.4 ± 0.4) nm for supercoiled DNA and (2.3 ± 0.5) nm for linear DNA, as compared to 1.5 nm and 0.7 nm for pure supercoiled and linear pUC19, respectively. The increase of height of the complexes indicates a more compact structure associated of multiple DNA molecules. Furthermore, it is quantitatively estimated from AFM images that the assemblies formed with supercoiled DNA show more toroidal aggregates (about 43%) as compared to linear DNA (about 17 %). This is understandable since linear DNA has larger persistence length, as well as excluded volume. Under the same conditions, it may be more difficult to bend linear DNA and form circles than supercoiled one. It thus exhibits the influence of DNA forms on complex morphology. All detailed results are listed in Table 4.4.2.1.

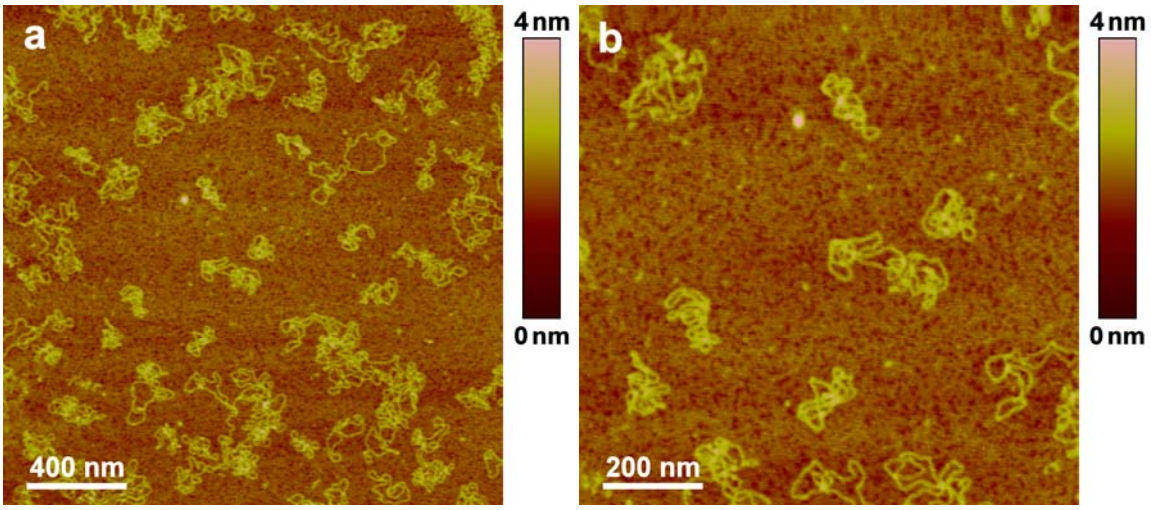

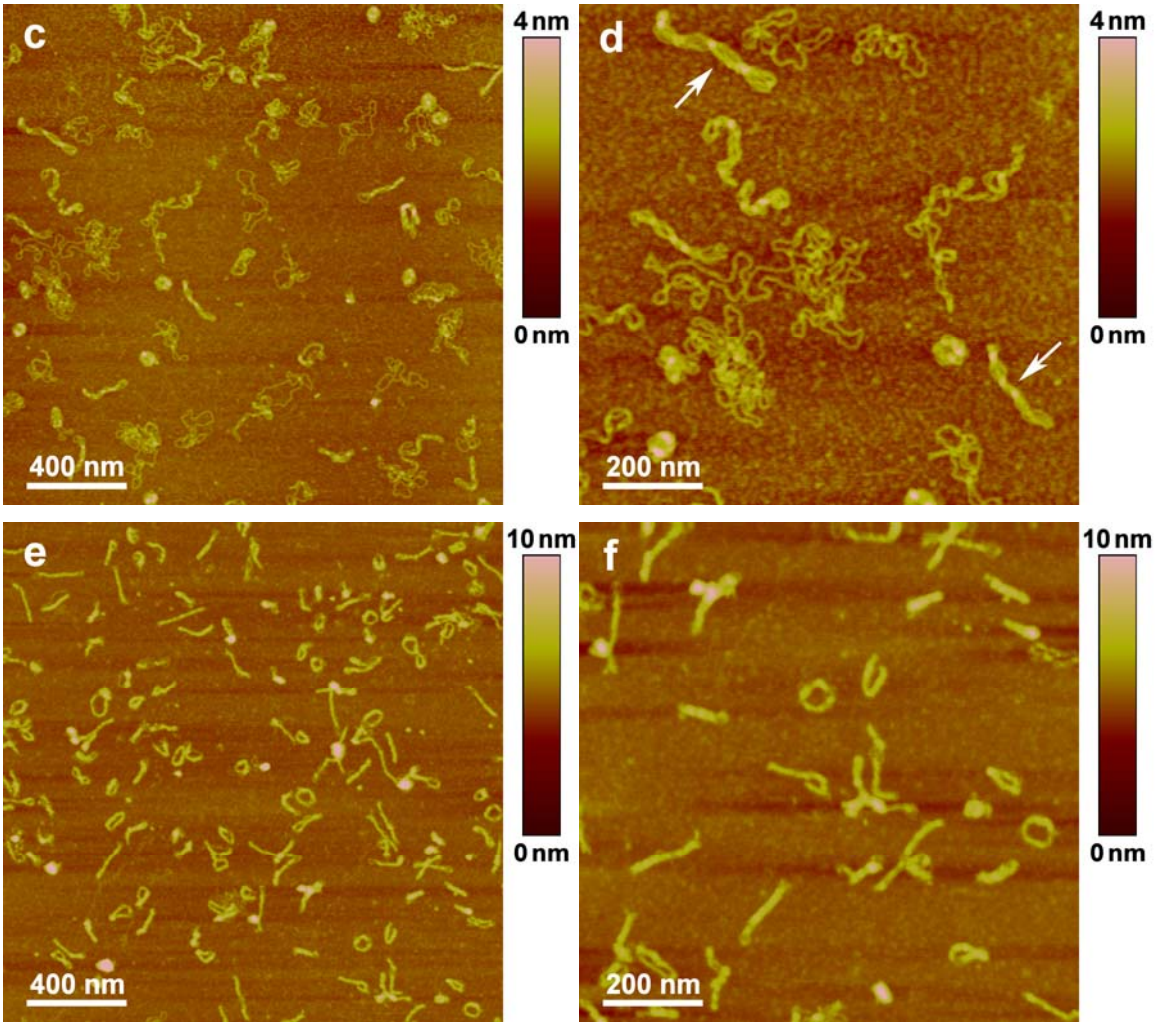

Figure 4.4.2.5. AFM images of complexes induced by supercoiled pUC19 and PSPDI at charge ratio l = 0.5 (a, b), l = 1 (c, d) and l =1.4 (e, f); (all: c(DNA) = 0.01 gL^{-1} in TE buffer)

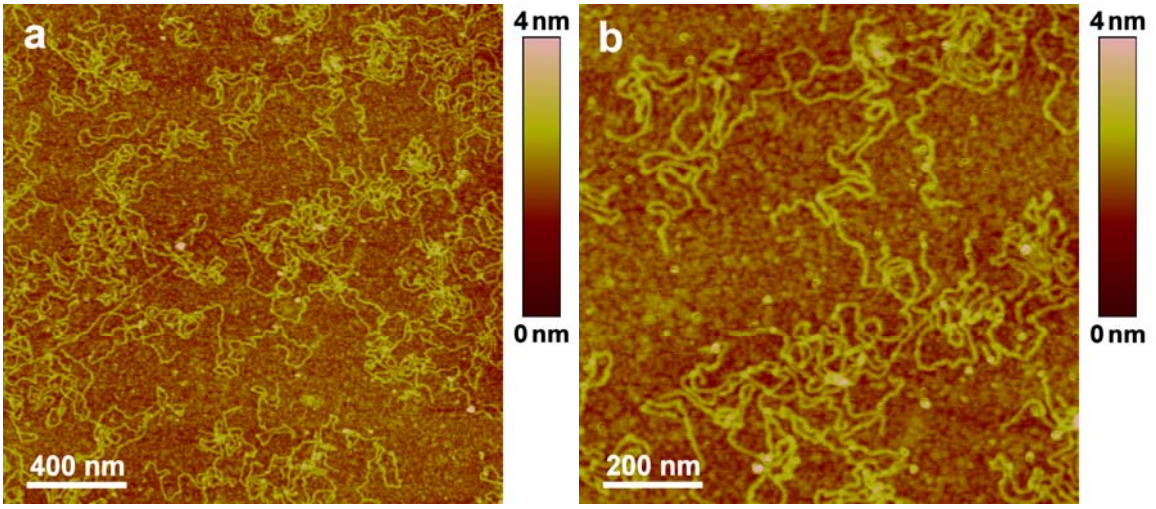

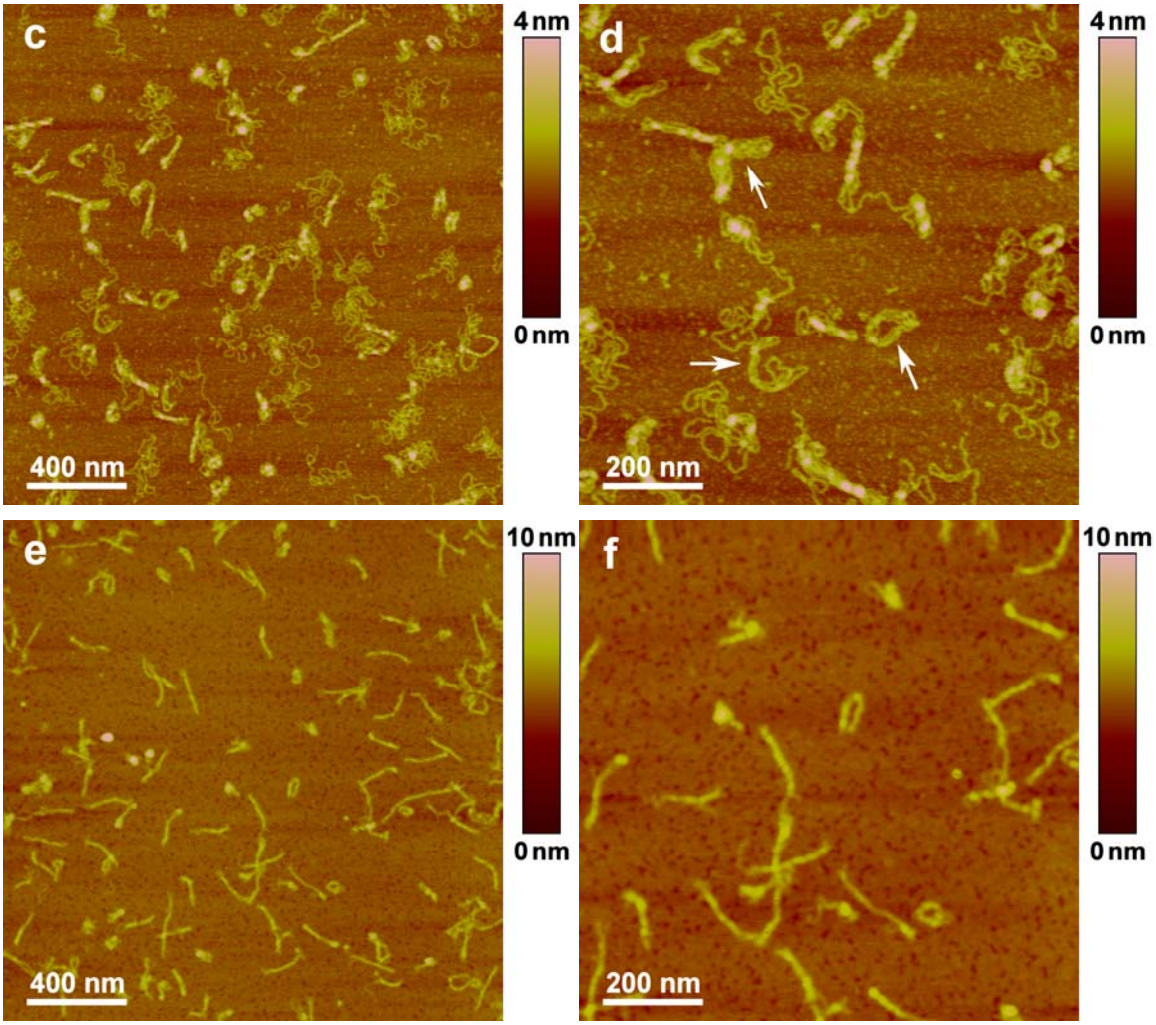

Figure 4.4.2.6. AFM images of complexes induced by linear pUC19 and PSPDI at charge ratio l = 0.5 (a, b), l = 1 (c, d) and l = 1.5 (e, f); (all: c(DNA) = 0.01 gL^{-1} in TE buffer)

Complexes structure	Supercoiled DNA complexes		Linear DNA complexes	
	rods	toroids	rods	toroids
Average size (nm)	190 ± 50	55 ± 8	200 ± 80	60 ± 10
Average height (nm)	2.9 ± 0.3	3.4 ± 0.4	2.0 ± 0.4	2.3 ± 0.5
R_H from DLS (nm)	128	26	129	25
Composition in AFM	58%	42%	86%	14%

Table 4.4.2.1. Summary of results from AFM and dynamic light scattering for aggregates formed with DNA and PSPDI in TE buffer

AFM measurements show that with increasing charge ratio, the complex morphology changes from flower-like structure to rods and toroids with mixtures of these morphologies as intermediates. With adding more PSPDI to DNA, the repulsive force between like-charged DNA molecules may be reduced due to progressing counterion condensation and neutralization of DNA chains. This has the consequence that different DNA strands can approach each other in parallel and come closer, forming strand-strand stabilization. Images in the transition range clearly indicate that rod-like aggregates and toroids are composed of several DNA strands (marked with arrows in image 4.4.2.5-4.4.2.6d). The finding of a transition stage from flower-like aggregates to rods and toroids is consistent with the suggestion by Fang et al. that flower-like structure might be one of the intermediates which are part of the pathway to the final toroid and rod structure.[56] Here we provide evidence for this assumption by demonstrating a complete complexation process, starting from flower-like aggregates to the final rods and toroids.

In AFM investigations, it may always be the case that the complex structure changes upon deposition on the surface and drying. Therefore, liquid AFM was performed. Figure 4.4.2.7 shows a liquid AFM image of an assembly formed with supercoiled pUC19 and PSPDI at charge ratio of 1.4 in TE buffer. Although the quality of the image is somewhat unsharp, the existence of toroids (marked with white arrows) and rods (marked with black arrows) is still evident. The section analyses of selected particles on the right side confirm the structures. The average height for toroids and rods are (4.1 ± 1.1) nm and (4.8 ± 1.2) nm, which is higher than that of the same sample in dried state (toroids: (3.4 ± 0.4) nm, rods: (2.9 ± 0.3) nm). Swelling of the complexes in the solution and/or the imperfect attaching of particles on the surface might be the possible explanations. The average diameter and length for toroids and rods are (62 ± 5) nm and (155 ± 48) nm, which is comparable to those results obtained from dry state AFM (toroids: (55 ± 8) nm, rods: (190 ± 50) nm). Thus it has been proven that in the solution complexes with the structure of rods and toroids are

present. Thereby, it is confirmed that in dry state AFM, the process of deposition and drying on the surface does not change the complex morphology essentially.

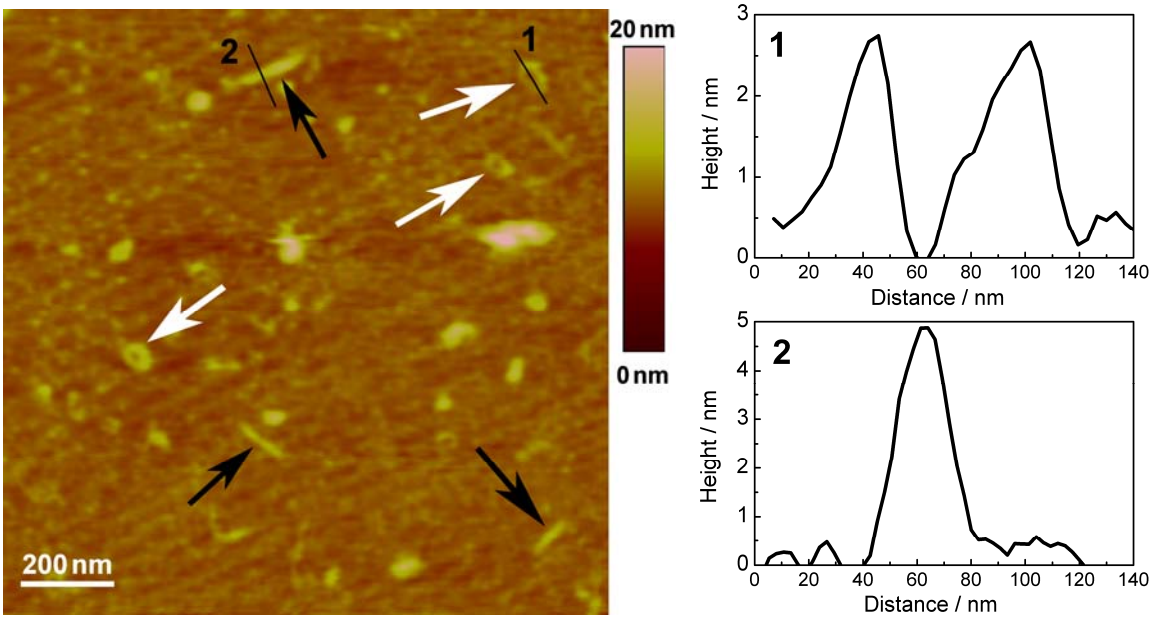

Figure 4.4.2.7. Liquid AFM images of complexes induced by supercoiled pUC19 and PSPDI at charge ratio of 1.4 (left) and section analyses plots of the indicated lines (right)

For comparison, a tetravalent porphyrin derivative TAPP was chosen to induce aggregation of DNA. On the one hand, this porphyrin molecule exhibits similar UV-Vis absorption property as PSPDI when associating with DNA, which is known as binding outside on the DNA surface. On the other hand, TAPP intends to stack with neighboring dye molecules by π-π interaction. This secondary interaction in the self-assembly might direct the complex to a more ordered supramolecular structure, while PSPDI does not show this property. Figure 4.4.2.8 presents an AFM image of an aggregate formed with supercoiled pUC19 and TAPP at charge ratio of 1.5. Only flower-like aggregates but no rodlike or toroidal structures are observed in the image. It is thus in contrast to the behavior of PSPDI. This experiment demonstrates the importance of the counterion structure. It shows that the smallest distance between positive charges of PSPDI molecule (0.51 nm ~ 0.54 nm), comparable to the distance of adjacent DNA phosphate groups (~ 0.55 nm), may play a key role in directing to

a more compact and well defined structures. (The smallest distance between positive charges of TAPP molecule is about 1.3 nm)

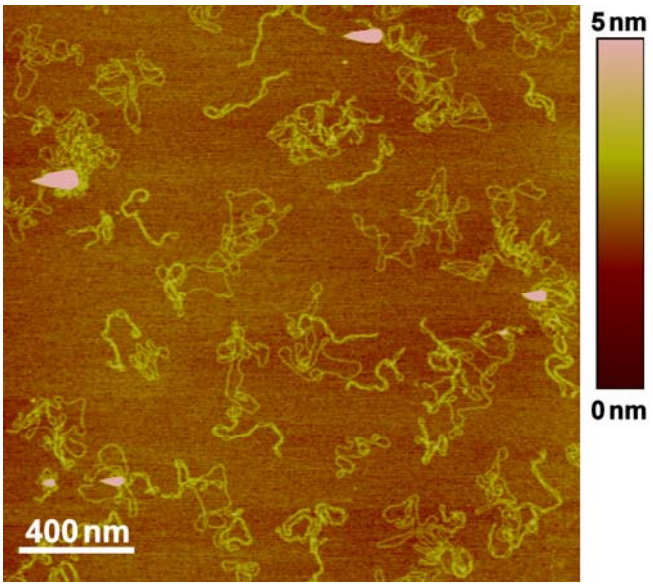

Figure 4.4.2.8. AFM image of aggregate formed by supercoiled pUC19 and TAPP at charge ratio 1.5 in TE buffer

The formation of toroids and rods with well-defined size is in analogy to other results with DNA[54,55] and other biomacromolecules.[156,157,158] It was theoretically explained by various authors. Bloomfield [159] constructed an association equilibrium theory for condensation of DNA by multivalent cations and demonstrated that the net attractive free energy grows nonlinearly because of the increasing average number of nearest neighbors of each duplex as the particle grows. When the size of the complexes reaches a maximum, the repulsive free energy which arises from the electrostatic self-energy of the incompletely neutralized particles prevents growing of the complex. Therefore, the aggregate size distribution is independent of DNA molecular length from 400 to 40000 base pairs. However, the formation of rodlike particles may be slower than the one of toroids even though their total energies are similar. It is required to overcome the high activation energy of highly distorted DNA bends or kinks at the turning points. Pincus et al. showed in theoretical considerations counterion induced

bundle formation.[160] According to his studies, bundle sizes diverge with point-like counterions due to complete charge neutralization, while for larger counterions steric hindrance and short range electrostatics prevent charge neutralization and cause formation of equilibrium bundles with defined size. This is due to the self-energy of the aggregate caused by its net charge in analogy to the Rayleigh instability of a charged oil droplet.[161] In accordance, computer simulations of semiflexible polyelectrolytes with trivalent counterions based on the coupling of surface tension, self-energy, and entropic degrees of freedom showed that thermodynamically stable bundles of finite size can form under certain conditions.[162] The formation of toroids may take place to avoid end-cap effects, as is also the case for polyelectrolyte block copolymer systems described by Förster et al.[163]

Further information could be extracted from the light scattering data. Figure 4.4.2.9 shows the total scattering intensity of DNA/PSPDI complexes in SLS (extrapolated to zero angle) as function of charge ratio. A strong increase is observed starting at charge ratio l = 1, which is an indication of an increase in molecular weight. The complexes thus likely contain more DNA strands for charge ratio l > 1. The bimodal distribution in DLS can yield intensity weighted contributions from different species at each measuring angle. By extrapolating the contribution of respective specie to q = 0, the relative contribution of each specie can be obtained. For example, the relative contribution from the smaller species (toroids) at charge ratio of 1.5 is calculated to be 17% for supercoiled DNA aggregates and 6% for linear ones. As these results represent the intensity weighted values, the number of smaller weight species is much higher. Although statistics of AFM and data quality of DLS are not sufficient to relate the two weights quantitatively, the results obtained from DLS are still qualitatively in accordance with the AFM results showing higher toroids content with supercoiled DNA.

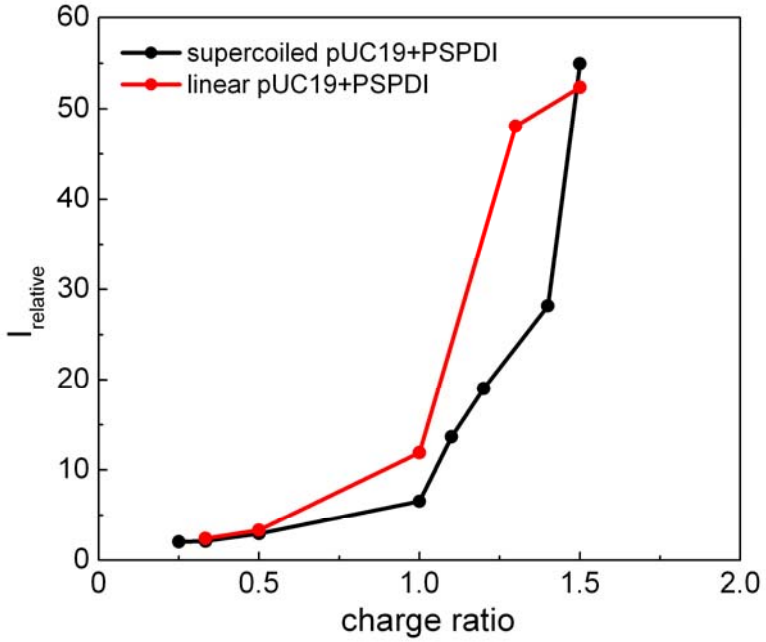

Figure 4.4.2.9. Relative scattering intensity of complexes induced by supercoiled or linear pUC19 and PSPDI; (all: c(DNA) = 0.01 g L^{-1} in TE buffer)

It was shown so far that the aggregates formed with DNA and PSPDI exhibits bimodal distributions at charge ratio over 1, which is rather different than the other divalent and tetravalent counterions. More compact rodlike and toroidal structures are observed for the DNA assemblies induced by PSPDI. It is then further of interest how the total concentration in the solution influences the behavior and structure of the DNA/PSPDI complexes. Light scattering results for varying DNA concentrations at charge ratio l = 0.5 and l = 1.4 are shown in Figure 4.4.2.10. As the DNA concentration increases, in both cases two processes are obtained. For complexes at charge ratio of 0.5, when c(DNA) ≤ 0.02 gL^{-1}, one process is observed. When the DNA concentration is larger than 0.02 gL^{-1}, two processes are presented. For assemblies at charge ratio of 1.4, one process is only obtained when DNA concentration decreases to 0.005 gL^{-1}. Over that concentration, two processes are always found. Similar to the previous results, the R_H of the smaller species lies again in the range of 20 nm to 30 nm and does not show significant changes, while the R_H for the larger particles increases with increasing DNA concentration.

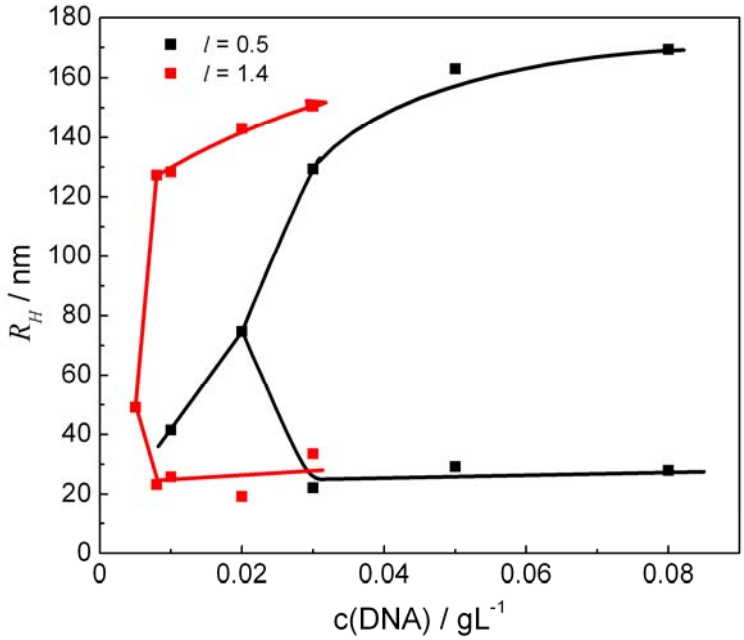

Figure 4.4.2.10. Hydrodynamic radius of assemblies induced by supercoiled pUC19 and PSPDI as a function of DNA concentrations

Corresponding AFM measurements were carried out for the samples mentioned above. Figure 4.4.2.11a shows a AFM image of the sample with c(DNA) = 0.1 gL^{-1} and l = 0.5. It reveals predominantly flower-like and rod-like aggregates. This corresponds to the bimodal distribution obtained in light scattering and is in contrast to only flower-like aggregates found for the sample with c(DNA) = 0.01 gL^{-1} at the same charge ratio discussed previously. For the complex formed at c(DNA) = 0.005 gL^{-1} and l = 1.4, flower-like and rod-like aggregates plus few toroids are observed (Figure 4.4.2.11b). This is in difference to only rods and toroids found for the assembly with c(DNA) = 0.01 gL^{-1} at the same charge ratio, but similar to the sample with c(DNA) = 0.01 gL^{-1} at lower charge ratio l = 1. Hence, the morphology of the complexes induced by DNA and PSPDI is not only directed by the charge ratio, but also by the total DNA concentration. This is in difference to the finding for divalent counterions, where the overall concentration did not show significant influence on the aggregate structure. The result may again be assigned to the stronger “connection” tendency of the tetravalent counterions.

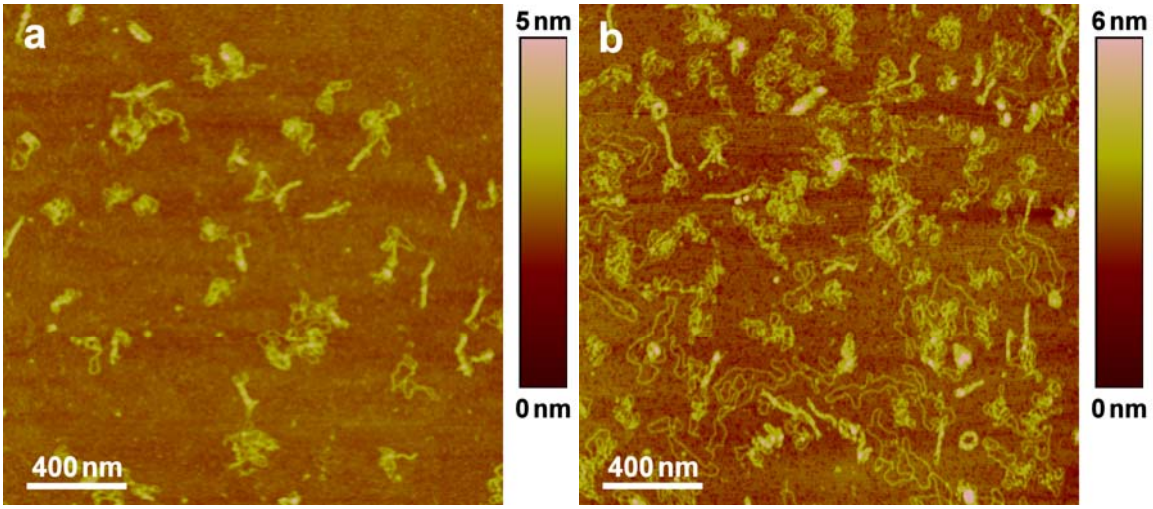

Figure 4.4.2.11. AFM images of complexes induced by supercoiled pUC19 and PSPDI with (a) c(DNA) = 0.1 gL^{-1}, l = 0.5 and (b) c(DNA) = 0.005 gL^{-1}, l = 1.4

A fundamental question of interest is whether aggregation of DNA and PSPDI is thermodynamically or kinetically controlled. Here the aggregate of supercoiled pUC19 and PSPDI at charge ratio of 1.4 is chosen as an example. The electric field autocorrelation functions and distributions of relaxation times are shown in Figure 4.4.2.12. It demonstrates the difference between samples prepared by different procedures: adding PSPDI into DNA solution, the preparation procedure usually applied throughout this study, yields a bimodal distribution, while the opposite procedure gives only one (relatively broad) distribution, which covers the part of smaller species in the bimodal distribution. This result is in contrast to that observed for complexation of DNA with both divalent counterions MV^{2+}, $C6D^{2+}$ and tetravalent counterion $C6T^{4+}$, which was shown to be a thermodynamically controlled process yielding equilibrium structures.

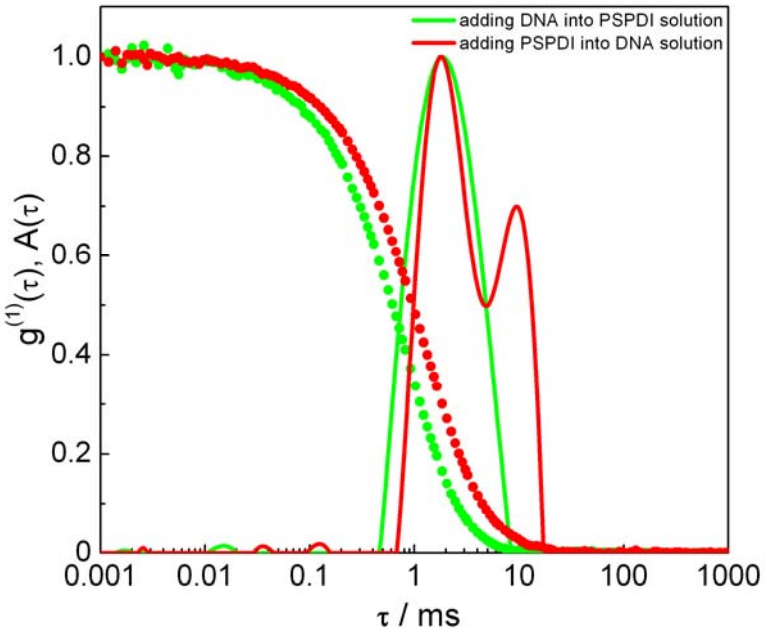

Figure 4.4.2.12. Normalized electric filed autocorrelation functions and relaxation times distributions of complexes formed with supercoiled pUC19 and PSPDI in TE buffer

AFM measurement of the sample prepared by the routine procedure (adding PSPDI into DNA solution) shows rod and toroid structures, while the sample prepared in opposite procedure yields rod-like structures with few flower-like aggregates (Figure 4.4.2.13). This corresponds to the structure “usually” observed for somewhat lower charge ratio samples, i.e. less PSPDI per DNA. This difference may be explained by temporary concentrations in the mixing procedure causing different charge ratios in a certain solution region and complexes once formed do not redissolve later. Evident from the results so far, it can be concluded that DNA/PSPDI assemblies at least partly generate kinetically controlled structures, in contrast to the systems discussed before. This result is thus in consistent with the theoretical prediction by Bloomfield that the formation of DNA complexes in the structure of toroids and rods is determined kinetically rather than thermodynamically.[159]

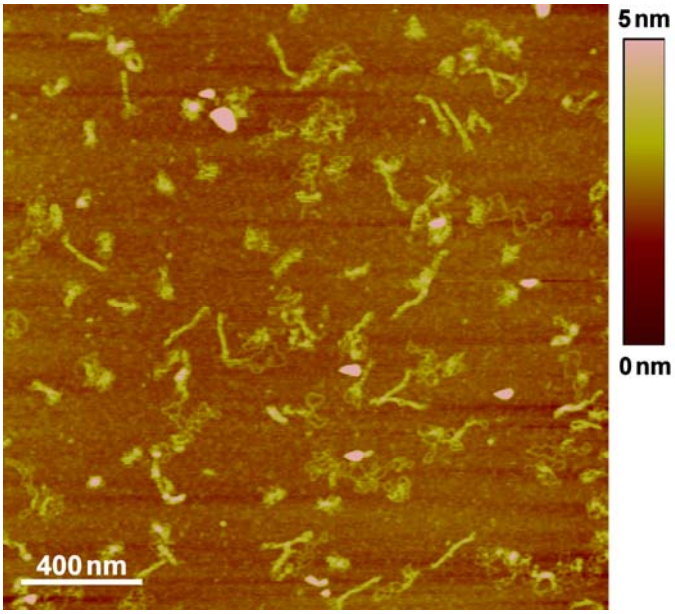

Figure 4.4.2.13. AFM images of complexes induced by supercoiled pUC19 and PSPDI at charge ratio of 1.4, prepared in the procedure of adding DNA into PSPDI solution

4.5 Conclusions

In this chapter the association of double-strand DNA with organic counterions via electrostatic interaction was presented, mainly focused on non-intercalating and non π-π interacting divalent and tetravalent counterions. Combining light scattering and AFM, it was found that in aqueous solution and under ambient temperature divalent counterions can induce the assembly of DNA molecules into flower-like aggregates, but only at high counterion excess, which is at charge ratios l = 500. Here the separation of two charges in the organic molecule is essential and sodium or magnesium ions do not induce formation of flower-like aggregates under the same conditions. To our best knowledge, this is the first time that similar flower-like structures are reported for the assemblies induced by divalent counterions. The tetravalent counterion $C6T^{4+}$ caused aggregation at much lower charge ratios, that is around charge stoichiometry. For the exact onset of aggregation and for the aggregate size and morphologies, it plays a role whether supercoiled or linear double-strand DNA of the same molecular mass is used. The assemblies induced by both divalent counterions and $C6T^{4+}$ were shown to be thermodynamically controlled and yielded equilibrium structures. The complexes were stable for at least 1 to 2 months.

The tetravalent chromophore PSPDI showed rather different complexation behavior than the other counterions. Assembly samples exhibited a bimodal distribution at charge ratios over 1. With increasing charge ratio, a complete complexation process was demonstrated by visualizing the transition of complex morphologies, from flower-like structure to coexisting well-defined rods and toroids with mixture of flowers/rods and toroids structures as intermediates. Rods and toroids consist of multiple DNA molecules. The comparative experiment of DNA/TAPP system suggested that the stiff structure of PSPDI and the closest distance between positive charges of the dye molecule (0.51 ~ 0.54 nm) may be responsible for this behavior. The formation of toroids and rods with well-defined

size was also theoretically explained. Pincus showed that the formation of equilibrium bundles with defined size is due to incomplete charge neutralization and the charged nature of the resulting species for non-point-like counterions. The total DNA concentration exhibited more influences on the association of DNA with PSPDI as compared to other counterions. Bimodal distributions were found with increasing concentration of DNA. In contrast to other systems, DNA/PSPDI complexes most likely generated kinetically controlled structures.

The association of supercoiled and linear DNA of the same molecular weight was compared for all counterions. The type of DNA (supercoiled or linear) showed more influence on the assembly morphology for tetravalent counterions than for divalent counterions. The complexes formed with $C6T^{4+}$ and linear DNA produced more compact structures than that with supercoiled DNA for charge ratio over 2. More rodlike particles (accordingly less toroidal aggregates) were observed for the complexes induced by PSPDI and linear DNA compared to that with supercoiled DNA.

In extension of earlier studies on the formation of defined and stable assemblies by electrostatic self-assembly of polyelectrolytes and organic counterions, it was thus shown that also counterions that do not exhibit mutual π-π interaction can yield assemblies of a certain size and shape that are stable in solution. The structure here is geometrically driven, i.e. determined by macroion and counterion architecture. The stability, in direct analogy to earlier systems, is provided by the charged nature of the assemblies, which again is due to the role of geometric effects in the association process.

In addition to the solution structures studied by light scattering, AFM yielded corresponding results for the complexes deposited on surfaces. Such composite assemblies of DNA and synthetic counterions representing defined entities on a surface may be of interest for further kinds of applications by taking advantage of optical and electrical properties of the counterions. Finally, the findings of this

study are thus not only of importance for a basic understanding of formation of DNA complexes with small synthetic counterions, but may also have an impact on various applications of ionic DNA assemblies, for example, in gene therapy or drug delivery systems.

CHAPTER 5. ASSOCIATION OF SODIUM POLYSTYRENE SULFONATE WITH OLIGOLYSINES

5.1 Introduction

The aim of this study is to investigate the formation of supramolecular structures from linear synthetic polyelectrolytes and oligopeptides. In difference to the DNA/counterion systems described in Chapter 4, a secondary force in addition to electrostatics is designed to provide molecular control of the complexes structure. For this purpose, mutual hydrogen bonding between the oligopeptide counterions is chosen. Oligolysine represents a good candidate due to its extra charges at the side chain and the potential of forming hydrogen bonds via peptide bonds (Figure 5.1.1 right). As introduced in Chapter 2.2, most of the studies on complexation of oligolysine in literature were limited to the association of DNA with oligolysine with a chain length $n \geq 3$. Only a few of those studies considered on the morphology of the aggregates.[85,86,164] Furthermore, it was shown that trilysine or oligopeptide containing trilysine segment failed to induce aggregation of DNA. In contrast, oligolysine with longer chain lengths ($n \geq 4$) could form various supramolecular structures with DNA, e.g. spherical and rodlike particles.[87,88] Therefore, in this study, it is valuable to first extend the concepts of complexation of oligolysine to a simple synthetic polyelectrolyte and then test the influence of the length of short oligolysines (repeat unit n = 2 ~ 5) on the association behavior and resulting assembly morphology, while the main focus is on trilysine.

The polyelectrolyte selected here is linear sodium polystyrene sulfonate (NaPSS). Its molecular structure is shown in Figure 5.1.1 (left). NaPSS is a common and well studied polyelectrolyte, which thus is suitable as model system. The average charge distance of SO_3^- in NaPSS (0.43 nm) is smaller than that of PO_4^- in DNA (0.55 nm), and closer to the distance of two adjacent side chains along the oligolysine backbone (0.39 nm). It means that the oligolysine may enforce less chain deformations when interacting with NaPSS than with DNA. The better matching of charge distance between NaPSS and oligolysine might give a higher possibility for the formation of assemblies and building of supramolecular structures, as compared to those with DNA. Two molecular weights of NaPSS are going to be investigated with regard to the association behavior with oligolysine. The one has a molecular weight of M_w = 3.3·10^4 gmol^{-1}, the degree of polymerization (DP) is about 160. The other one has a molecular weight of M_w = 9.4·10^5 gmol^{-1}, the repeat unit n is around 4560.

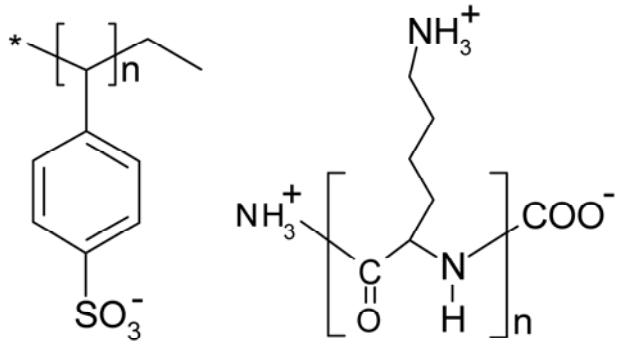

Figure 5.1.1. Molecular structure of sodium polystyrene sulfonate (left) and oligolysine (right)

The content of this chapter is arranged as follows: first, the characterization of the components used in this study will be presented, which includes pH titration, light scattering and AFM measurements. Secondly, association of NaPSS and trilysine will be discussed in detail in Chapter 5.3. Finally, the association of NaPSS with different oligolysines (di-, tetra- and pentalysine) will be compared in Chapter 5.4.

5.2 Characterization of the Components

Oligolysine is a zwitterion containing both amino groups and a carboxylic group, which means that the charges of oligolysine can be changed through the pH of the solution. Therefore, pH titration of the oligolysine solution is necessary to determine the appropriate pH value for the following work. Figure 5.2.1 displays a titration result of pentalysine. Two major changes in the degree of dissociation are observed in the plot. One is in the pH range of 4 to 6, the other appears after pH ≥ 8. It is known that the pK_a value of carboxylic group and amino groups in lysine is 2.16 and 9.06 or 10.54 (depending on N-terminal NH_3^+ or side chain NH_3^+), respectively.[165] Therefore, it is clear that the change in degree of dissociation between pH 4 to 6 is due to the deprotonation of acetate groups (pK_a = 4.75), which are brought as the initial counterions of pentalysine. The other change in degree of dissociation at pH ≥ 8 is contributed from the titration of amino groups. It shows that below pH 8, all the functional groups of pentalysine (amino and carboxylic groups) are charged and thus generate 1 negative charge and 6 positive charges. This titration result is comparable with previous report on the titration behavior of polylysine.[166] Based on the titration results, the pH value of the solution is adjusted in between 6 to 7 for all experiments to ensure a defined charge status of the system.

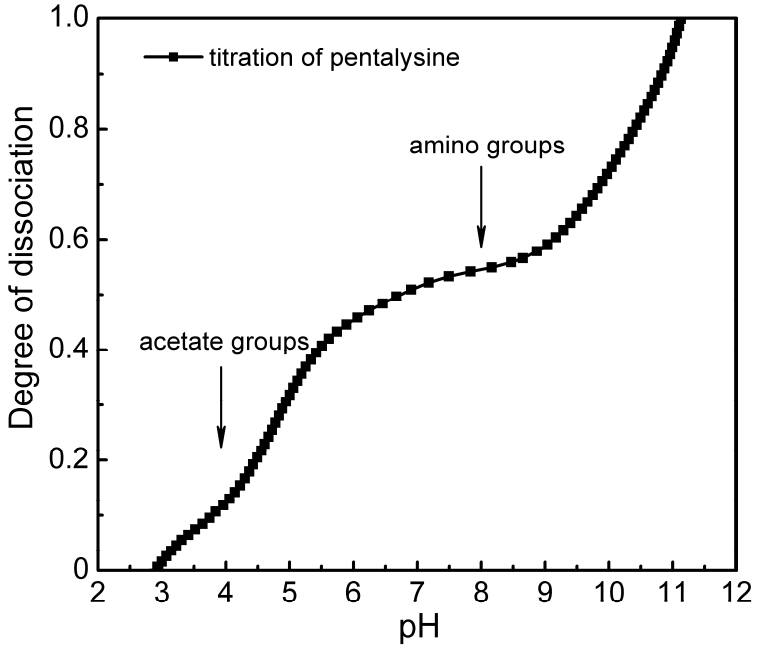

Figure 5.2.1. Degree of dissociation of pentalysine as a function of pH

NaPSS is a strong polyelectrolyte. In the pH range of 6 to 7, the NaPSS molecule is also fully charged. In order to eliminate the polyelectrolyte effects, the characterization of NaPSS in light scattering was carried out in presence of 24 mM NaCl. As demonstrated previously, the characteristic parameter λ is then calculated to be 0.02, which is much smaller than that of the transition regime (λ = 1). It ensures the complete elimination of polyelectrolyte effects in light scattering measurement. Figure 5.2.2 shows the autocorrelation function and relaxation times distribution of high molecular weight NaPSS (M_w = 9.4·10^5 gmol^{-1}, c(NaPSS) = 0.1 gL^{-1}) at a scattering angle of 90°. A monomodal distribution is obtained. The mean relaxation time of the distribution is 0.31 ms. By extrapolating to zero scattering angle, the hydrodynamic radius of this NaPSS at concentration of 0.1 gL^{-1} is calculated to be around R_H = 47 nm. Mandel et al. reported the scaling relationship of NaPSS with various molecular weights under different polymer or salt concentrations.[167,168] They revealed that in the dilute regime, the diffusion coefficient of NaPSS exhibits mainly molar mass dependency. The hydrodynamic radius of NaPSS with molecular weight of 6.5·10^5 gmol^{-1} and 12·10^5 gmol^{-1} in the dilute regime was shown to be 32 nm and

60 nm, respectively (in presence of 10 mM NaCl). Our result is in good agreement with their findings.

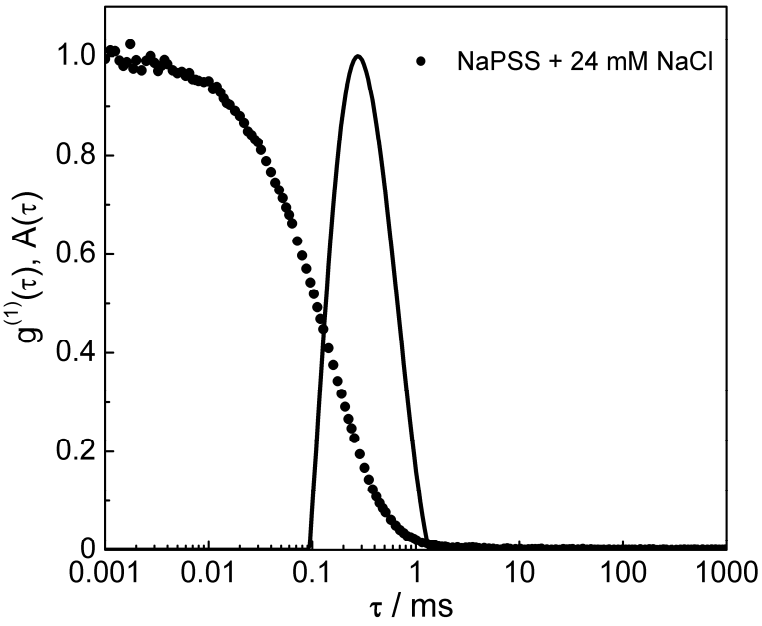

Figure 5.2.2. Normalized electric field autocorrelation function $g^{(1)}(\tau)$ and relaxation times distribution $A(\tau)$ of NaPSS ($M_w = 9.4 \cdot 10^5$ gmol^{-1}) at a scattering angle of 90°

AFM measurements allow visualizing the NaPSS molecules. Figure 5.2.3 shows the AFM images of high molecular weight NaPSS molecules deposited on different substrates. It is found that on bare mica, the NaPSS molecule exhibits both coils and an "extended" coil form (Figure 5.2.3a). The average height of the NaPSS is (0.92 ± 0.09) nm. Similar results were also reported by other authors.[169,170] On the other hand, clusters of NaPSS molecules are observed on APTES modified mica (Figure 5.2.3b). Due to the positively modified surface, the formation of polymer clusters is possible by neutralizing the charges of NaPSS. This shows again the influence of surface on the molecule structure. The scale bar on the right side indicates an enhanced height of the clusters due to the overlapping of NaPSS molecules.

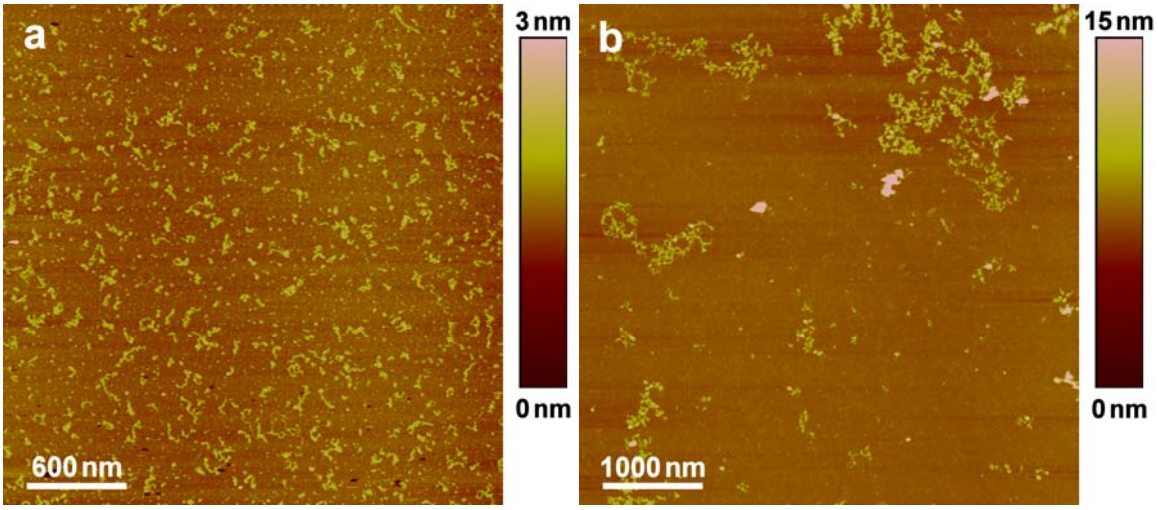

Figure 5.2.3. AFM images of high molecular weight NaPSS on (a) bare mica and (b) 0.1% APTES modified mica.

5.3 Association of NaPSS with Trilysine

The complexation of NaPSS with trilysine was first investigated by light scattering. Figure 5.3.1 displays the autocorrelation functions and relaxation times distributions of NaPSS/trilysine complexes with and without salt. It is evident that at the same charge ratio, complexation without salt generates a single narrow distribution, while the sample with NaCl results in two peaks. One of the peaks from the sample containing NaCl overlaps with the complex peak from the sample without NaCl. The other peak of the bimodal distribution lies at a faster relaxation time τ = 0.22 ms, which is comparable to that of pure NaPSS at 90° (τ = 0.31 ms). It indicates that the smaller peak might be caused by the uncomplexed NaPSS in the solution. The bimodal distribution here thus implies the incomplete complexation of the sample containing NaCl. It shows that trilysine induces aggregation of NaPSS without any additional low molecular mass salt. Presence of NaCl limits the complex formation. Furthermore, no detectable autocorrelation function was obtained for pure trilysine solution at the same concentration as that for the complexation. It shows that the complex obtained here is indeed due to the interaction of NaPSS and trilysine.

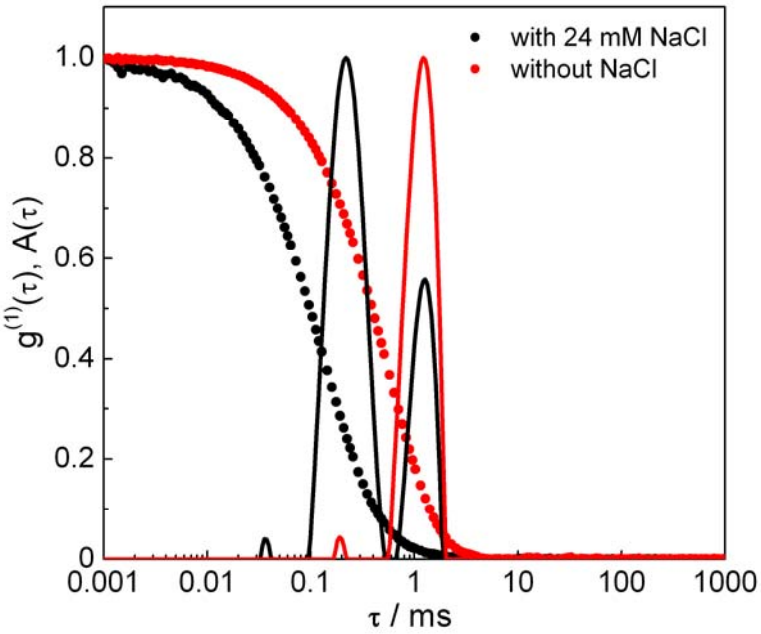

Figure 5.3.1. Normalized electric field autocorrelation functions $g^{(1)}(\tau)$ and relaxation times distributions $A(\tau)$ of complexes formed by NaPSS and trilysine; (all: c(NaPSS) = 0.1 gL^{-1})

The reason for the incomplete complexation behavior in the presence of salt may be explained by the screening of the electrostatic interaction due to the salt, i.e. by thermodynamic aspects. It was proposed by Sato et al.[171] that the free energy of a self-assembly system is contributed from the entropy of mixing, enthalpy of mixing and electrostatic free energy. The entropy gain in our system is determined by the amount of counterions (Na^+) which can be released from NaPSS chains into solution during complexation, while the electrostatic energy is related to the charges of the polyelectrolyte. Therefore, the addition of salt not only reduces the electrostatic energy by screening electrostatic interaction, but also reduces the entropy gain of releasing NaPSS-bound Na^+ ions due to the osmotic pressure changes induced by increasing salt concentration. In other words, the free energy of the complexation is decreased upon addition of salt, which results in a weaker tendency for association. The screening of electrostatic interaction by salt prevents further interactions between polyelectrolytes and counterions. Similar behavior was also observed by other authors.[22,88] Due to the

findings here, all future works are carried out in salt free solution (no added additional salt).

The diffusion coefficients as a function of scattering vector square for assemblies formed by high molecular weight NaPSS and trilysine are shown in Figure 5.3.2 (top). Similar to that of DNA complexes, the charge ratio l is also defined as the ratio of the molar concentration of net positive charges of oligolysine to the molar concentration of SO_3^- groups of NaPSS:

$$l = \frac{c(NH_3^+, oligolysine)}{c(SO_3^-, NaPSS)}$$

When the charge ratio l is smaller than 0.91, no aggregation is detected in light scattering. In the range of $0.91 \leq l \leq 2$, complexes with well-defined size distributions are obtained. The complex solution turns more opalescent with higher charge ratio (Figure 5.3.2 below), which was not observed for the DNA complexes before even though their sizes are comparable. At charge ratio $l > 2$, the solution becomes clear overnight due to the precipitation of the particles.

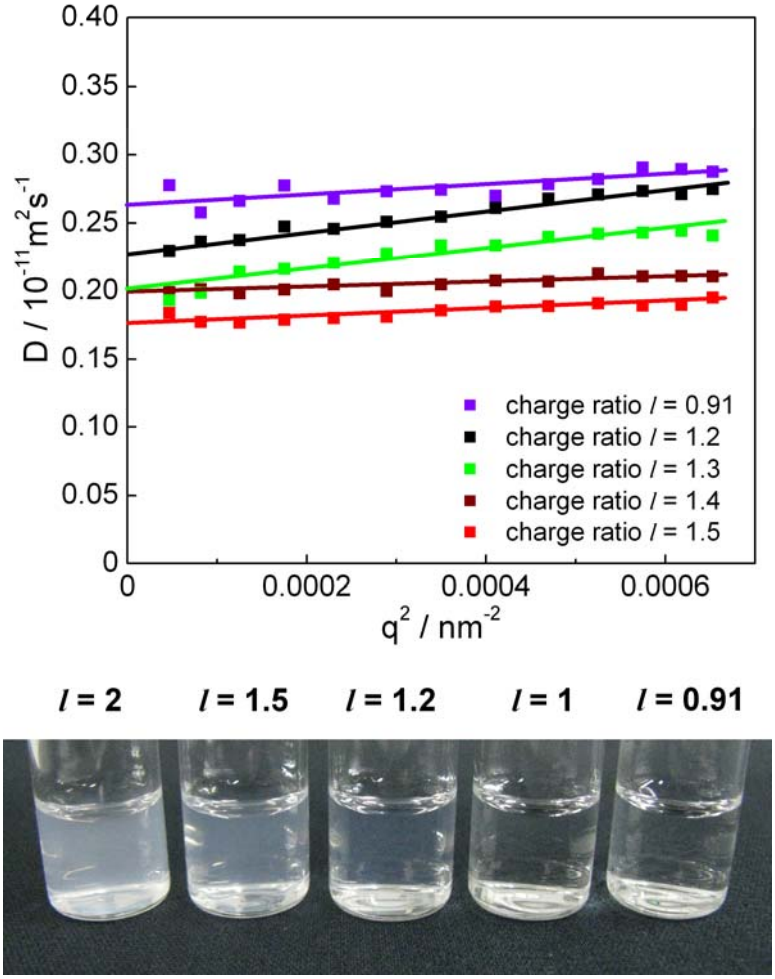

Figure 5.3.2. Diffusion coefficients as a function of scattering vector square for complexes induced by high molecular weight NaPSS and trilysine (above) and the picture of complex solutions (below) at different charge ratios; (all: c(NaPSS) = 0.1 gL^{-1})

Systematic results of the NaPSS/trilysine complex in dependence on charge ratio are shown in Figure 5.3.3. Three distinct regimes are observed for both R_H and R_G: in regime 1 and 3, where the charge ratio $l \leq 1$ and $l \geq 1.5$, R_H and R_G both increase with increasing charge ratio. In regime 2 ($1 \leq l \leq 1.5$), both R_H and R_G show no significant changes. In this regime, R_H and R_G are around 110 nm and 115 nm, respectively. It needs to be noted that all the samples investigated here show a comparable size distribution with about 10% to 20% standard deviation. Therefore, the different behavior observed here is not due to a difference in the broadness of the size distribution. It might indicate that the complexes formed in

the regime 2 have different properties compared to those samples in the regime 1 and 3. This association behavior is also significantly different from that of DNA complexes.

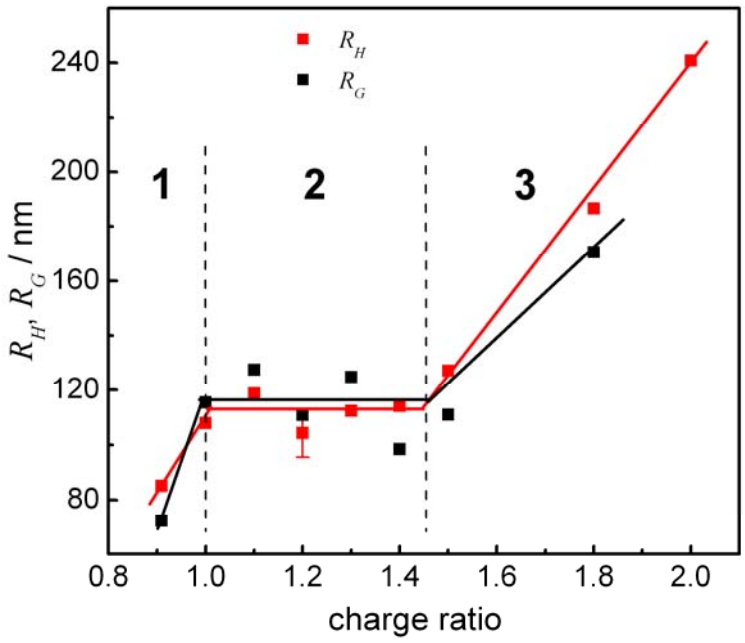

Figure 5.3.3. Hydrodynamic radius (R_H) and radius of gyration (R_G) of complexes associated with high molecular weight NaPSS and trilysine in MQ water

SLS gives more information, as shown in Figure 5.3.4. All the data are presented as Zimm, Berry and Guinier plot. For the samples in the regime 1 and 3, only the Guinier plots exhibit linear relationships (Figure 5.3.4a-c, g-i). The higher the charge ratio, the more pronounced difference in linearity is. The linearity of SLS data in Guinier plot is a strong indication that spherical particles are formed in the solution. In contrast, for the sample in the regime 2, neither Guinier nor Zimm plot show linearity, only Berry plot is suitable for fitting the SLS data (Figure 5. 3.4d-f). Although Berry plot is not as sensitive as Guinier plot in respect of particle shape, however, it is still a clear sign that the samples in the “constant” size regime might have different morphologies as the samples in other regimes.

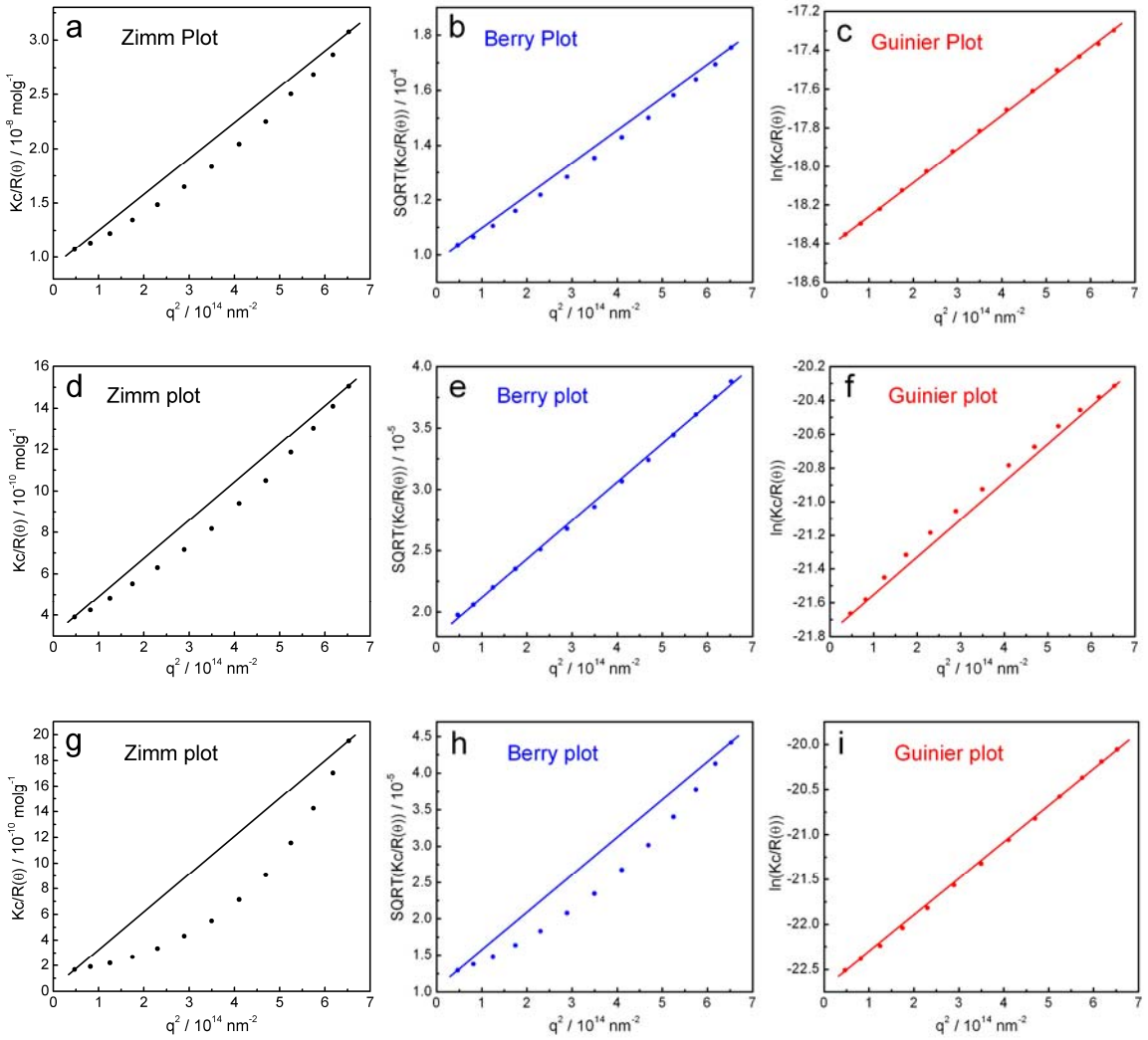

Figure 5.3.4. Static light scattering data of aggregates induced by high molecular weight NaPSS and trilysine at charge ratio of 0.91 (a-c), 1.2 (d-f) and 1.5 (g-i); (all: c(NaPSS) = 0.1 gL^{-1})

The difference in SLS also becomes evident in the characteristic R_G/R_H ratio (Figure 5.3.5). Three regimes are also obtained. The samples in the "constant" size regime give a constant characteristic ratio as well, which is around R_G/R_H = 1.1. The samples in the "increasing" size regime also exhibit constant ratio around R_G/R_H = 0.85, which is close to the theoretic R_G/R_H ratio of a homogeneous sphere (0.778).[96] The difference between them might be due to the possible polydispersity. Nevertheless, the R_G/R_H ratio in the regime 1 and 3 confirms the formation of spherical particles in the solution in accordance with the Guinier plot linearity. Furthermore, the plot also shows that even so the size of

the complexes increases in the regime 1 and 3, the structure of the complexes does not show significant changes. Again, it is evident that the samples in the regime 2 generate different structures from the samples in other regimes.

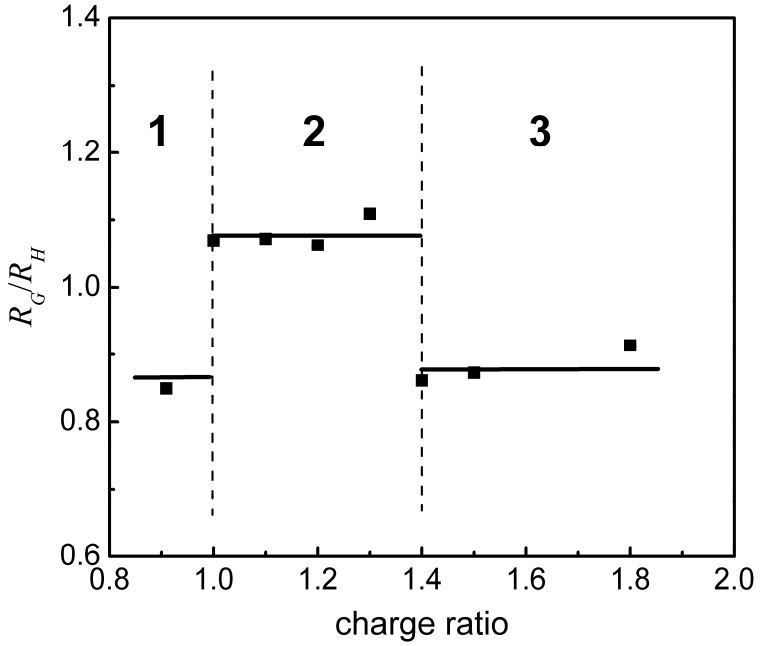

Figure 5.3.5. Characteristic R_G/R_H ratio of complexes formed with high molecular weight NaPSS and trilysine in MQ water

Zeta potential measurements reveal information about the charge of the complexes, as presented in Figure 5.3.6. All the samples show a negative zeta potential in the investigated charge ratio range. With increasing charge ratio, the zeta potential of the complex increases first, and then gradually decreases. At almost stoichiometric charge ratio l = 1.1, the zeta potential reaches the smallest magnitude of -2.1 mV. It is understandable that in the excess of NaPSS the complex becomes negatively charged (charge ratio $l \leq 1$). The first increase in zeta potential before the stoichiometric charge ratio is simply due to the continuous neutralization of the charges upon addition of counterions. However, it is surprising to obtain negative zeta potentials for samples with excess of trilysine ($l \geq 1.1$). The reason is not completely understood yet. However, an excess of negative change can only be caused by an excess of NaPSS in the

complex. Thus, despite trilysine molecules are in excess, not all polyelectrolyte charges become neutralized. It is consistent with the recent discussion of an excess of positive charge acting as stabilization force for assemblies of cationic dedrimers.[24] Therefore, the overall negative value of the zeta potential that become about constant with increasing charge ratio is understandable. It is however unclear yet, why at intermediate charge ratio more charges can be neutralized and the assembly carries a smaller net charge (even though still negative). Likely, this is due to the different architecture of the assemblies in this region as discussed above.

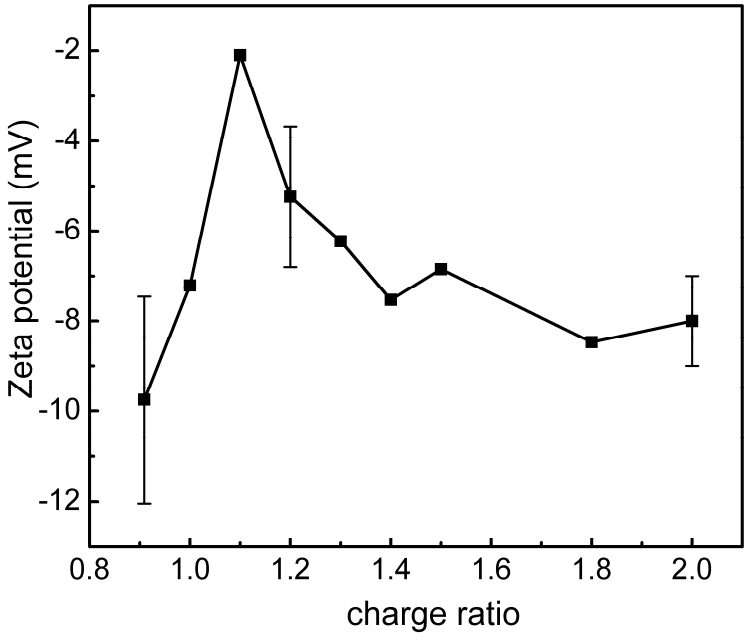

Figure 5.3.6. Zeta potential of the complexes induced by high molecular weight NaPSS and trilysine in MQ water; (all: c(NaPSS) = 0.1 gL^{-1})

To gain further insight into the assembly architecture, they were imaged by AFM. For imaging the polyelectrolyte complexes, the surface charge property of the substrate on which the particle is deposited plays a key role. Zeta potential results can provide assistance for deciding on the suitable substrate in AFM measurements, which will be focused on in more detail in Chapter 6. Figure 5.3.7a-b show images of the assemblies formed by high molecular weight NaPSS and trilysine in the regime 1 (charge ratio of 0.91) and regime 3 (charge

ratio of 1.5) on APTES modified mica. Both samples show spherical structure, which is in agreement with the results from light scattering. The spherical particles have an average height of (7.4 ± 1.5) nm and diameter of (202 ± 31) nm for aggregate with charge ratio of 0.91. The complex with charge ratio of 1.5 exhibits an average height of (8 ± 2.1) nm and diameter of (300 ± 66) nm. The heights are obviously higher than that of pure NaPSS on bare mica (0.92 ± 0.09) nm, which implies the formation of complexes from multiple polymer molecules. However, they are much smaller than the diameters, which indicates the deformation of complexes on the surface. Adhesion forces and suppression of soft particles by the AFM tip are likely the causes of that. [172] In contrast to that, the image of the sample in the regime 2 (charge ratio of 1.2) taken on APTES modified mica exhibits only disassembled polymer instead of complexes (Figure 5.2.7c), while the sample deposited on bare mica shows sphere-like aggregates (Figure 5.2.7d). The average height and diameter of the particle is (4.6 ± 1.1) nm and (221 ± 79) nm, respectively.

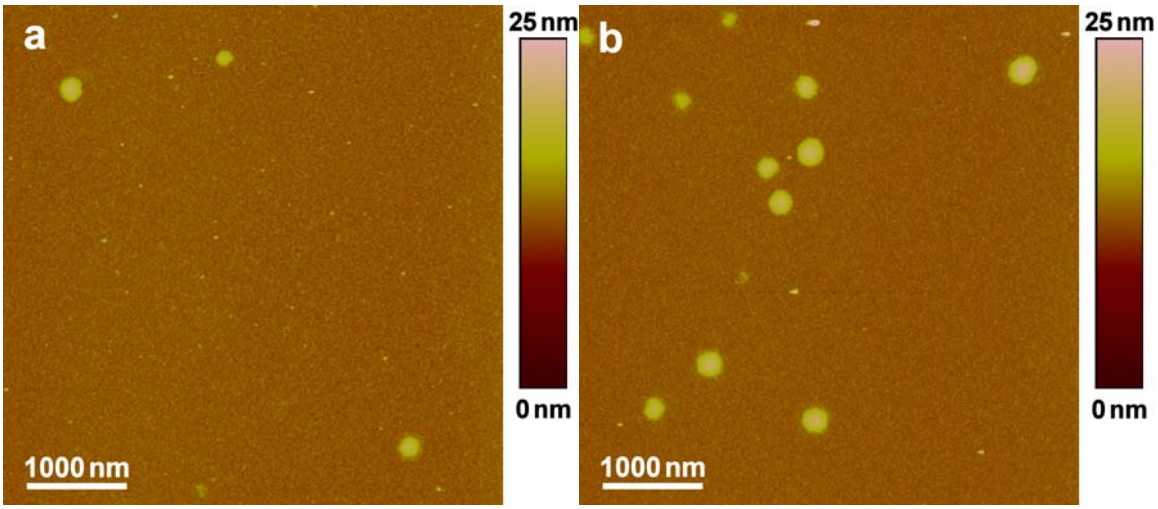

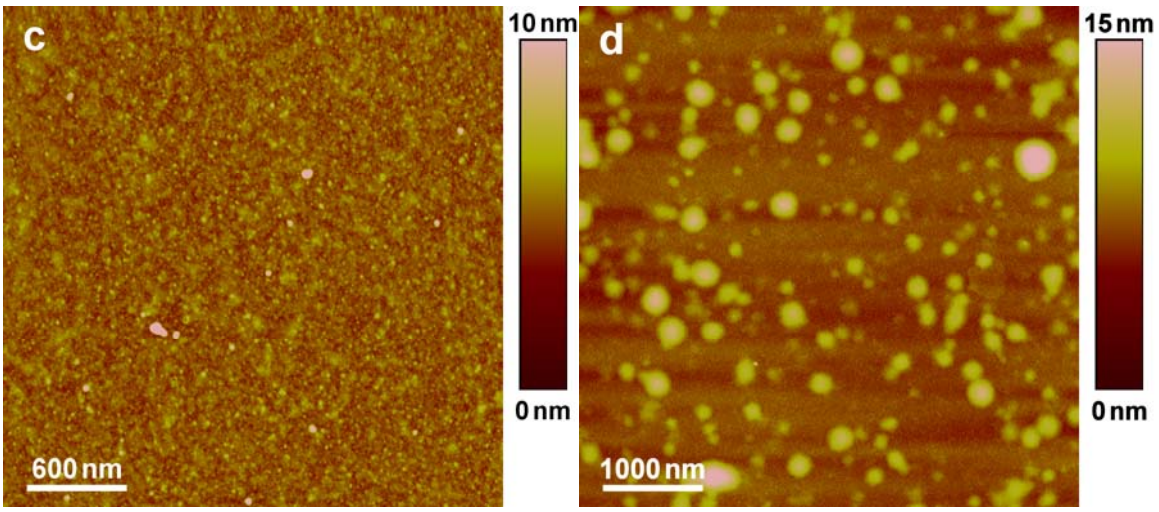

Figure 5.3.7. AFM images of complexes induced by high molecular weight NaPSS and trilysine in MQ water: (a) charge ratio of 0.91 on 1% APTES modified mica, (b) charge ratio of 1.5 on 0.1% APTES modified mica, (c) charge ratio of 1.2 on 0.1% APTES modified mica, (d) charge ratio of 1.2 on bare mica; (all: c(NaPSS) = 0.1 gL^{-1})

Due to the deformation of the particles, it is difficult to directly compare the diameter estimated from AFM with the solution value obtained from light scattering. However, a comparison of the volumes is possible. The aggregate volume in solution is calculated according to a spherical structure, which is $V_{solution}$ = 2.57·10^6 nm^3, 4.71·10^6 nm^3 and 8.58·10^6 nm^3 for samples with charge ratio of l = 0.91, 1.2 and 1.5, respectively. On the other hand, the spherical complexes deform into a “cap of a sphere” when depositing and drying on the surface. The volume for those aggregates in the dried state is thus calculated to be V_{dried} = 1.19·10^5 nm^3, 8.74·10^4 nm^3 and 2.83·10^5 nm^3. Dividing the volume of complexes in the dried state by that in solution yields a ratio of 4.6%, 1.8% and 3.3% for the samples with charge ratio of 0.91, 1.2 and 1.5, respectively. It shows that these aggregates shrink strongly upon drying, i.e. in solution they are loosely packed so that large parts of the complex volume are occupied by water. Furthermore, a somewhat smaller volume ratio is obtained for the complex with charge ratio of 1.2 as compared to the others. It indicates the different behavior of the assemblies from various regimes, which is in analogy to the light scattering results. Several possibilities could explain this difference: (i) the assembly at

charge ratio l = 1.2 has a different structure (other than the spherical structure in the other regimes) and thus rearranges differently when drying on a surface. (ii) The difference in volume ratio is caused by the different swelling of different samples in solution. (iii) The interactions between the samples and the substrate surfaces (mica or APTES modified mica) are different, which influences the volume of the sample in the dried state. However, it was shown in SLS that the sample at charge ratio of 1.2 does not show linearity in a Guinier plot and exhibits a different R_G/R_H ratio compared to the other samples. Therefore, it suggests that most likely the morphology of the assembly at charge ratio of 1.2 is different from a homogenous spherical structure.

It is expected that an oppositely charged surface with moderate charge density is required for successfully imaging the polyelectrolyte complexes on the surface according to the zeta potential results. This concept is proven by AFM measurements of the samples with charge ratio of 0.91 and 1.5. Those complexes have negative zeta potentials and can only be imaged on APTES modified mica (details see Chapter 6.2). However, the complex formed at charge ratio of 1.2 betrays the rule even though it also has a negative zeta potential. It disintegrates on positively charged surface and can only be imaged on bare mica. This result shows that the assembly formed at charge ratio of 1.2 is more stable on bare mica than the samples at charge ratio of 0.91 or at charge ratio of 1.5. It suggests that there might be an extra force in the complex at charge ratio of 1.2 to stabilize the particles against the repulsive force between surface and particles, and this sample might have positive charges on the surface due to the different architecture despite of its overall negative zeta potential. Concerning the design of the system, it is expected that hydrogen bonds are formed in the assembly with charge ratio of 1.2 and essentially contribute to the complex stabilization on bare mica. The positive charges on the surface of the complex might be the reason for the disassembly of particles on APTES modified mica.

In order to directly prove the formation of hydrogen bonds, attenuated total reflection infrared (ATR-IR) spectroscopy was applied to investigate the system. Usually the IR measurement requires a high concentration of materials ($c > 1\ gL^{-1}$), which is much higher than the normal working concentration in this study. Therefore, the concentration of NaPSS in the complex for IR measurements was increased to $1.5\ gL^{-1}$. The solution ATR-IR spectra of pure NaPSS and trilysine and their complex with charge ratio of 1.2 are shown in Figure 5.3.8. The pure NaPSS solution exhibits 4 bands, which are at wavenumber 1178 cm^{-1}, 1127 cm^{-1}, 1036 cm^{-1} and 1008 cm^{-1}. The SO_3^- group antisymmetric and symmetric vibrations are assigned to the peaks at 1178 cm^{-1} and 1036 cm^{-1}, respectively. Peaks at 1127 cm^{-1} and 1008 cm^{-1} are contributed from the in-plane skeleton vibration and in-plane bending vibration of benzene ring, respectively. The pure trilysine solution presents 2 major bands. The main peak centers at wavenumber 1553 cm^{-1}, which is caused by the antisymmetric carboxylate stretch and antisymmetric and symmetric deformations of the side-chain NH_3^+ and *N*-terminal NH_3^+. The other band is located at wavenumber 1414 cm^{-1}. This is due to the symmetric carboxylate stretch. Similar spectra of NaPSS and trilysine were also reported by other authors.[173,174].

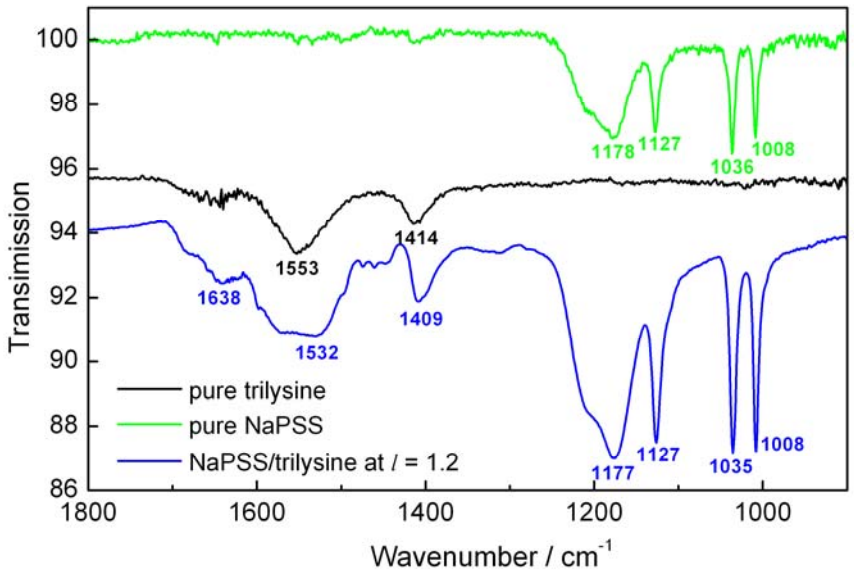

Figure 5.3.8. Solution ATR-IR spectra of pure NaPSS, pure trilysine and their complex; (the concentration of trilysine solution and NaPSS solution is 4 and 5 gL^{-1}, respectively; the concentration of NaPSS in the complex is 1.5 gL^{-1})

Compared to the IR spectra of pure NaPSS and trilysine, the spectra of their complex shows significant differences at the regime where the contributions are mainly from trilysine: the main peak of trilysine centered at 1553 cm^{-1} is shifted to lower wavenumber 1532 cm^{-1}. The band shape is changed and the band is broadened. The peak at 1414 cm^{-1} is also shifted to lower wavenumber 1409 cm^{-1}. The band at 1638 cm^{-1}, which is assigned to the amide I stretch (carbonyl stretching vibrations) of the peptide backbone, becomes much more prominent after complexation. The amide I band is normally sensitive to the peptide secondary structure due to the formation of hydrogen bonds.[175,176,177] Therefore, the increased signal at 1638 cm^{-1} is a strong evidence of the formation of hydrogen bonds through the peptide backbones, which was assumed before. Meanwhile, the shift to lower frequency and the broadening of the X-H stretch bands accompanying by an increase in intensity is normally a strong indication of formation of hydrogen bonds in the system.[178,179] It indicates that the changes of the bands at wavenumber 1532 cm^{-1} and 1414 cm^{-1} not only represent the electrostatic interactions between charged groups,[174] but also suggest possible hydrogen bonding between the carboxylic and amino groups of the trilysine molecules.[179] Therefore, the IR results here directly prove the existence of hydrogen bonds in the NaPSS/trilysine system and somehow support the explanations suggested above.

In the following, the role of hydrogen bonds in the self-assembly system is discussed. The formation of hydrogen bonds is expected to occur as follows: in the sample with charge ratio of 1.2, the negative charges of individual NaPSS chain are fully neutralized by positive charges of trilysine via electrostatic interaction around the stoichiometric ratio, so that hydrogen bonds can possibly be formed intra- and inter- NaPSS molecules and connect the chains into a more ordered structure (Figure 5.3.9 left). The hydrogen bonding stabilizes the complexes and determines the spatial arrangement of the NaPSS chain. It leads to a different behavior, e.g. possibly different structure and can only be imaged on bare mica in AFM. On the other hand, for the complexes formed at charge

ratio of 0.91 or 1.5 where more excess of NaPSS or trilysine is present, the repulsive force resulted from the higher excess charges, as revealed by zeta potential measurements, may prevent the formation of hydrogen bonds. Thus, much less hydrogen bonds are formed for the samples with charge ratio of 0.91 or 1.5. In the spherical particles, the NaPSS chains may be randomly connected by multivalent trilysine molecules and aggregated simply due to the electrostatic interactions (Figure 5.3.9 right). Therefore, the size of the spherical particles increases with increasing charge ratio.

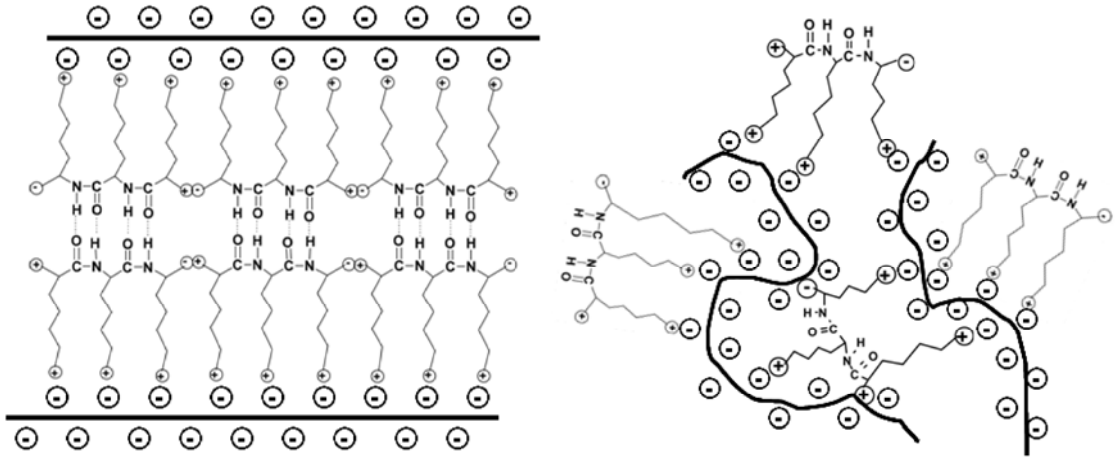

Figure 5.3.9. Schematic illustration of complex formation for sample at charge ratio of 1.2 (left) and 0.91 (right)

Further, the stability of the complexes in solution is of interest. Here the complex induced by NaPSS and trilysine at charge ratio of 1 and 1.2 were chosen as examples (Figure 5.3.10). The data for sample with charge ratio of 1 (blue and black curves) show that the hydrodynamic radius is relatively stable over 20 days. However, the scattering intensity decreases with time. Likely, this is due to some particles in the solution sedimenting because of their size, while the rest of the particles stay in solution with constant size. Similar precipitation behavior was also observed for complexes formed with DNA and pentalysine by other authors.[88] In particular, the complex with charge ratio 1 is stable within ± 6 nm in size and ± 640 kHz in scattering intensity during one week. Comparable results

are also obtained for the other sample with charge ratio of 1.2, which suggests a stable complex for at least 10 days (green and red curves).

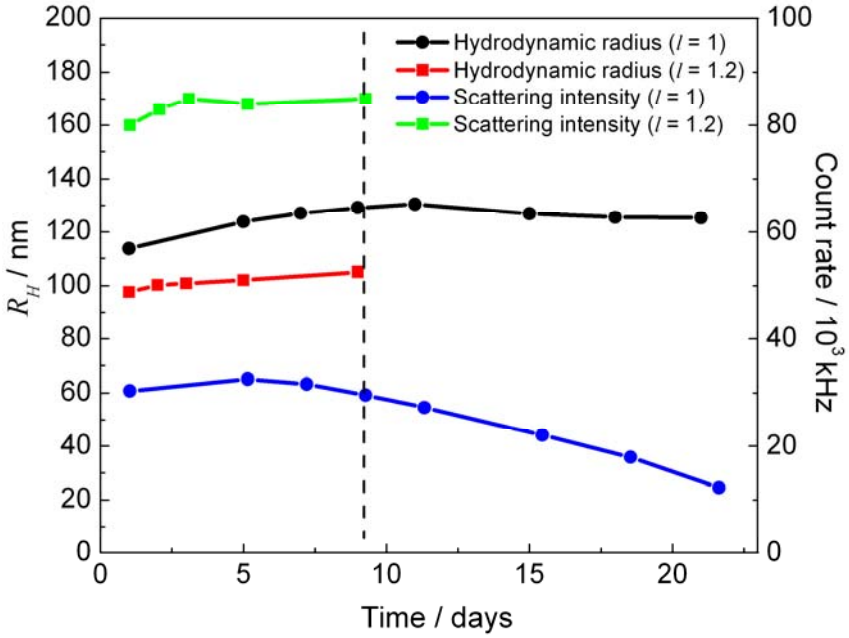

Figure 5.3.10. Stability of complexes induced by high molecular weight NaPSS and trilysine at different charge ratios in MQ water

Finally the complex induced by high molecular weight NaPSS and trilysine at charge ratio of l = 1.2 was selected to further elucidate the complexation process with respect of physical chemistry. The DLS results of the samples prepared via different mixing orders (that is to add NaPSS into trilysine solution or add trilysine into NaPSS solution) are shown in Figure 5.3.11a. Both procedures produce a monomodel narrow distribution. However a size difference between them is evident. The R_H of the assembly produced by normal procedure (adding trilysine into NaPSS solution) is about (104 ± 10) nm, while the sample prepared by the other method (adding NaPSS into trilysine solution) yields a R_H about (75 ± 6) nm. The difference of those two samples is also reflected in SLS experiments. As presented previously in Figure 5.3.4b, the SLS data of the sample prepared by adding trilysine into NaPSS solution only exhibits linearity in a Berry plot. The sample prepared in the other order shows bent curves in Zimm and Berry plot and an good linear relationship in the Guinier plot (Figure 5.3.11b-d), which

indicates a spherical structure of the assembly. Thus not only size but also structure may differ for the same sample prepared in different procedures. As discussed in Chapter 4, this result suggests that either both preparation methods generate kinetically controlled structures or at least one of the procedures yields kinetically controlled aggregates, which is different to the thermodynamically controlled assemblies produced by the other method.

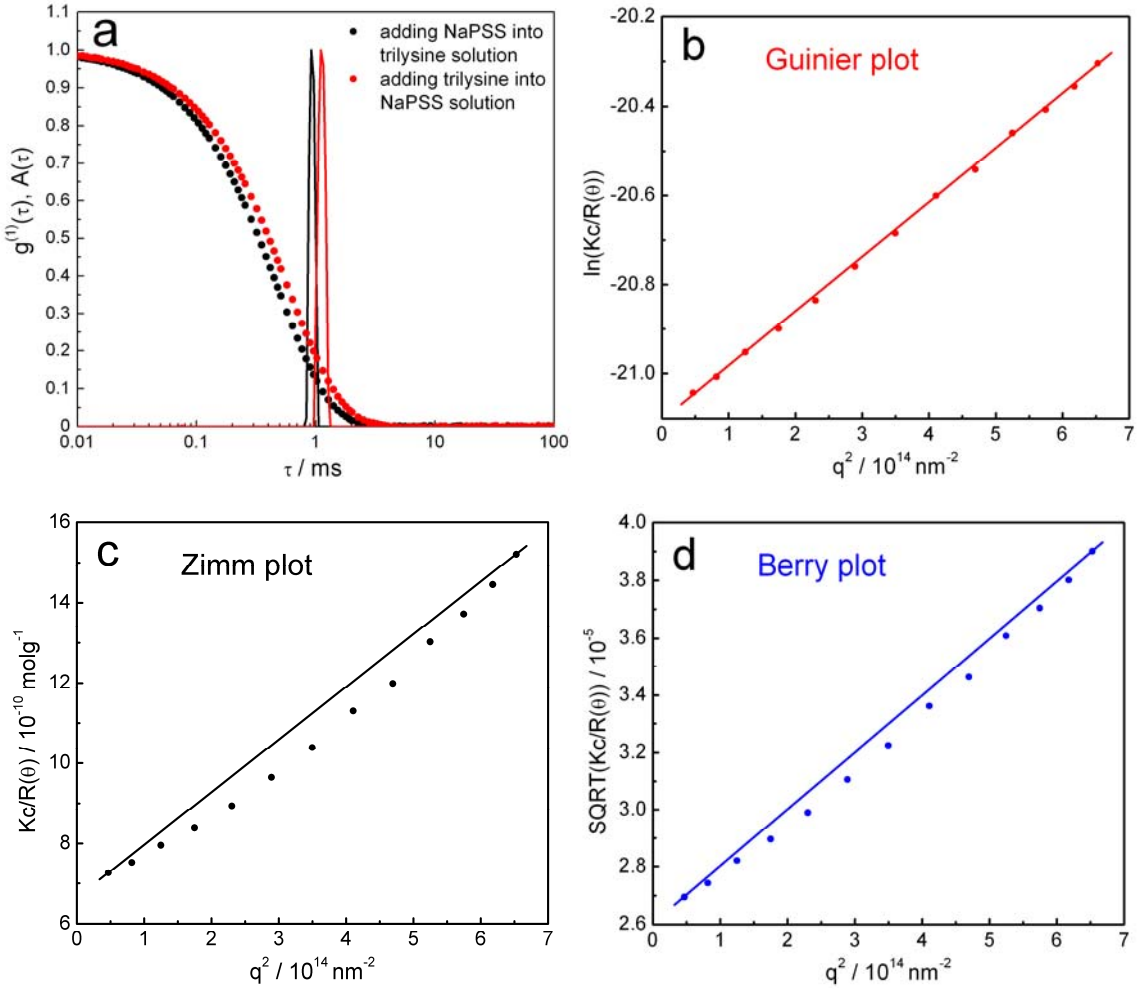

Figure 5.3.11. (a) Normalized electric field autocorrelation functions $g^{(1)}(\tau)$ and relaxation times distributions $A(\tau)$ and SLS data (b-d) for complexes prepared in the order of adding NaPSS into trilysine solution. (all: c(NaPSS) = 0.1 gL^{-1})

To elucidate the influence of polyelectrolyte concentration on the association behavior, experiments were also carried out at a NaPSS concentration of c(NaPSS) = 0.01 gL^{-1}. Figure 5.3.12a displays the autocorrelation functions and

distributions of relaxation times for various samples at a scattering angle of 90°. No defined complex is obtained at the stoichiometric charge ratio l = 1. Single narrow distributions are only observed for complexes with charge ratio $l \geq 5$. The extrapolated diffusion coefficient gives $R_H \approx 65$ nm and $R_H \approx 127$ nm for the aggregates at charge ratio of 5 and 10, respectively (Figure 5.3.12b). In addition, the small slope of the plot confirms a well defined size distribution. The result obtained at the stoichiometric charge ratio is in difference to that obtained at NaPSS concentration of c(NaPSS) = 0.1 gL^{-1}.

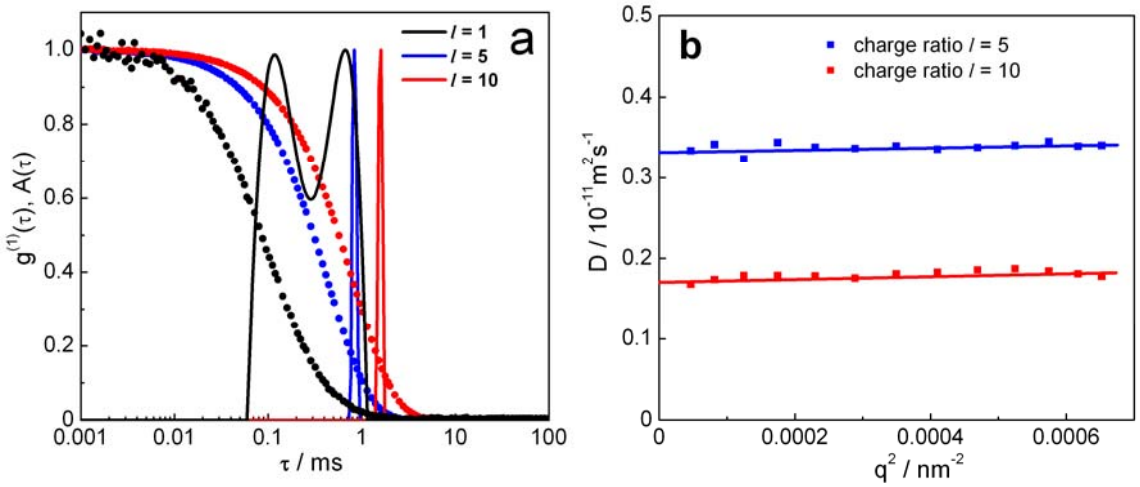

Figure 5.3.12. (a) Normalized electric field autocorrelation functions $g^{(1)}(\tau)$ and relaxation times distributions $A(\tau)$ at a scattering angle of 90° and (b) diffusion coefficient as a function of scattering vector square for complexes induced by high molecular weight NaPSS and trilysine at different charge ratios; (all: c(NaPSS) = 0.01 gL^{-1})

Figure 5.3.13 presents the SLS data for the samples mentioned above. Zimm plot and Berry plot (not shown) do not show linear behavior of the SLS data, which is even more obvious at higher charge ratio l = 10. Only a Guinier plot exhibits linearity. It shows again that the complexes formed at low NaPSS concentration might be also in spherical structure.

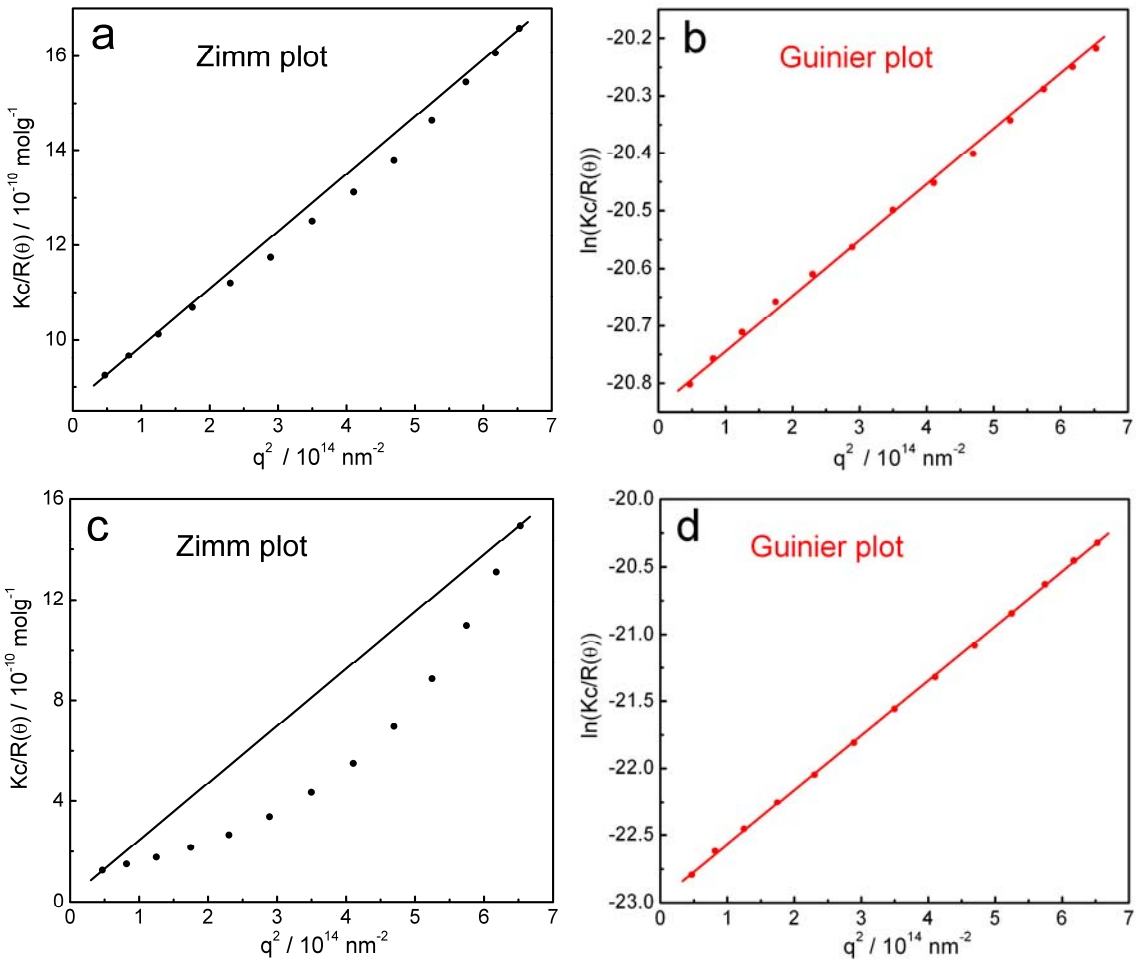

Figure 5.3.13. Static light scattering data for complexes formed with high molecular weight NaPSS and trilysine at charge ratio of 5 (a-b) and charge ratio of 10 (c-d); (all: c(NaPSS) = 0.01 gL^{-1})

The complexes formed at low NaPSS concentration (c(NaPSS) = 0.01 gL^{-1}) were further investigated in AFM. Figure 5.3.14 shows the images of samples with charge ratio l = 5 and 10 on APTES modified mica, which is appropriate according to their negative zeta potential results. Spherical particles are found for both samples, which is in agreement with the structural indication from SLS data. The average height and diameter for complexes at charge ratio of l = 5 is (17 ± 1.4) nm and (240 ± 32) nm, and those for sample with charge ratio l = 10 is (25 ± 3.7) nm and (500 ± 77) nm. Applying the same strategy mentioned before, the ratio of the complex volume in dried state and in solution is calculated to be 34% and 29% for the sample with charge ratio l = 5 and 10, respectively. Compared to

the volume ratios obtained for complexes at higher polymer concentration (c(NaPSS) = 0.1 gL^{-1}), the results received here are one magnitude bigger, which implies less water molecules are present in the aggregates in solution. This can be explained by the higher charge ratios required at lower polymer concentration. There are certainly more lysine molecules in one assembly with increasing charge ratios, which accordingly leaves less space for water molecules. The smaller water content in the complexes is also equivalent to a denser aggregate structure.

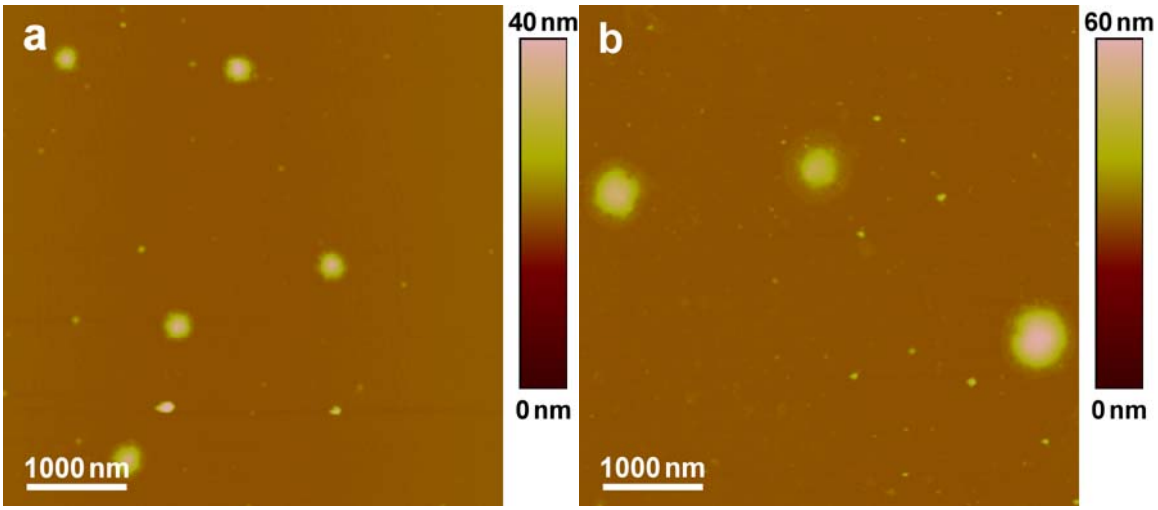

Figure 5.3.14. AFM images of complexes induced by high molecular weight NaPSS and trilysine at (a) charge ratio of 5 on 0.1% APTES modified mica and (b) charge ratio of 10 on 0.01% APTES modified mica; (all: c(NaPSS) = 0.01 gL^{-1})

The comparison of complexes formed at different NaPSS concentration is summarized in Table 5.3.1. At c(NaPss) = 0.1 gL^{-1}, the aggregates are induced at stoichiometric ratios. Different supramolecular structures are obtained dependent on the charge ratio. While for the samples at a NaPSS concentration of 0.01 gL^{-1}, the complexes are only formed at much higher charge ratio ($l \geq 5$). Spherical particles are observed. It is evident that the overall polymer concentration plays a crucial role in the complexation of NaPSS and trilysine. The formation of assemblies is shifted to higher charge ratio by reducing the

polyelectrolyte concentration, which will be further discussed in the following chapters.

c(NaPSS)	0.01 gL^{-1}		0.1 gL^{-1}		
Charge ratio	l = 5	l = 10	0.91 ≤ l ≤ 1	1 ≤ l ≤ 1.4	1.4 ≤ l ≤ 2
DLS	monomodel narrow distribution		monomodel narrow distribution		
R_H (nm)	65	127	85 ~ 108	~ 111	114 ~241
SLS	linearity in Guinier plot		linearity in Guinier plot	linearity in Berry plot	linearity in Guinier plot
R_G (nm)	53	110	72 ~115	~ 115	115 ~171
R_G/R_H	0.82	0.87	~ 0.87	~ 1.08	~ 0.87
Structure	Spherical	Spherical	Spherical	Non spherical	Spherical

Table 5.3.1. Summary of complexation of high molecular weight NaPSS with trilysine

Complexation of trilysine with low molecular weight NaPSS was also investigated. Light scattering results are shown in Figure 5.3.15. The autocorrelation function of the aggregate at charge ratio l = 10 gives a main distribution with a mean relaxation time around (1.6 ~ 1.9) ms, plus a small second peak at relaxation time around 0.05 ms (Figure 5.3.15a). The bimodal distribution could be caused by polyelectrolyte effects or two species with distinct size. However, the relative contribution of the smaller peak increases with time. This implies that the bimodal distribution most likely is due to two species in the solution that changes with time. The major peak yields a $R_H \approx$ 180 nm, which may be considered as the size of the complex. The small second peak results in a R_H of (3.9 ± 0.2) nm, which corresponds to the size of single NaPSS molecule with this molecular weight. It shows that with low molecular weight NaPSS not all the polymers are associated into the aggregates, even at charge ratio of 10. The increasing smaller peak indicates that free NaPSS contributes more and more to the autocorrelation function. This observation is also evident in Figure 5.3.15b. The scattering

intensity of the complex continuously decreases, while R_H increases. It reveals that the assembly induced by low molecular weight NaPSS and trilysine continuously precipitates or decomposes/rearranges. Therefore, increasing amount of free NaPSS is found in the solution. All evidence shows that the aggregates produced by low molecular weight NaPSS and trilysine are not as stable as those with high molecular weight NaPSS.

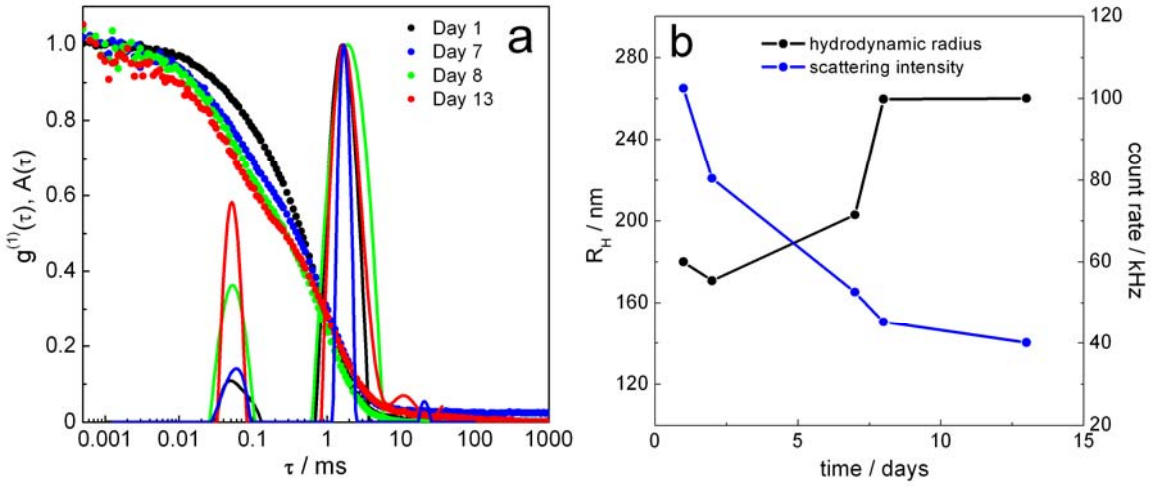

Figure 5.3.15. (a) Normalized electric field autocorrelation functions $g^{(1)}(\tau)$ and relaxation times distributions A(τ) at a scattering angle of 90° and (b) stability of complex induced by low molecular weight NaPSS and trilysine at charge ratio of 10; (c(NaPSS) = 0.05 gL^{-1})

5.4 Association of NaPSS with Different Oligolysines

5.4.1 Association of NaPSS with Dilysine

To investigate the influence of the oligolysine chain length on the complexation behavior, both low and high molecular weight NaPSS were first combined with dilysine. Figure 5.4.1.1a shows the electric field autocorrelation functions and relaxation times distributions of complexes composed of low molecular weight NaPSS. Both charge ratio and polymer concentration were varied. At c(NaPSS) = 0.1 gL^{-1} and l = 50 (black line), the decay time is around 0.04 ms, resulting in a $R_H \approx$ (3.3 ± 0.3) nm, which likely represents the free NaPSS in the solution. At c(NaPSS) = 0.01 gL^{-1} even with charge ratio l = 100 (red line), no detectable autocorrelation function is obtained. Therefore, for the low molecular weight NaPSS/dilysine system, under the mentioned conditions, no aggregates are formed.

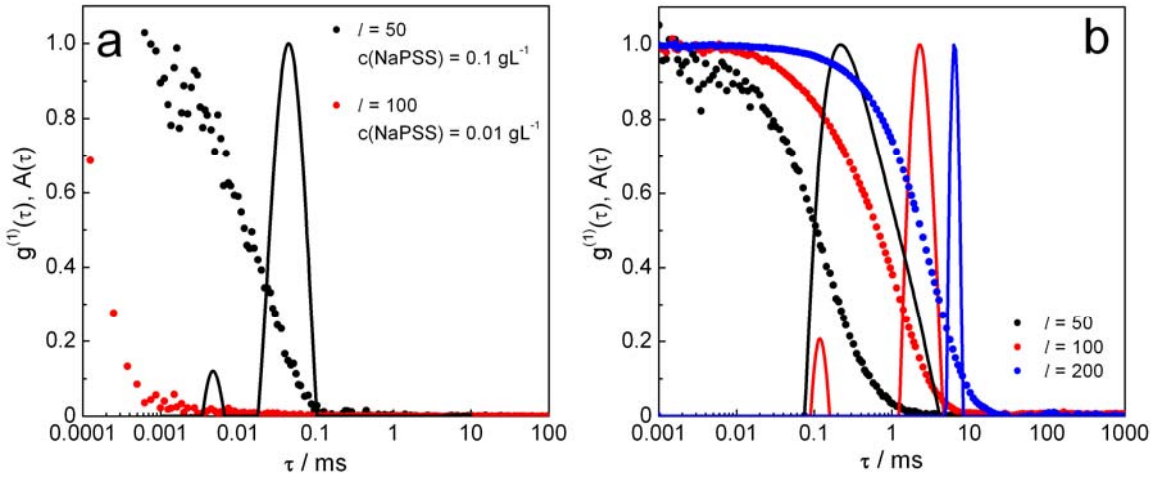

Figure 5.4.1.1 Normalized electric field autocorrelation functions $g^{(1)}(\tau)$ and relaxation times distributions $A(\tau)$ at a scattering angle of 90° of complexes formed with (a) low molecular weight NaPSS or (b) high molecular weight NaPSS and dilysine in MQ water

Figure 5.4.1.1b shows the autocorrelation functions and distributions of relaxation times for aggregates formed by high molecular weight NaPSS. A clear shift is found in the plot. The extrapolated R_H increases from around 50 nm at charge ratio l = 50 to around 500 nm at charge ratio l = 200. The higher the charge ratio, the more narrow distribution is. It shows that complexes are formed with high molecular weight NaPSS at charge ratio $l \geq 100$. This result is comparable to the findings of the association behavior of DNA with divalent counterions. It indicates that dilysine has rather lower efficiency to induce aggregation of multiple polymer chains. The possible reason is due to its low valence and possibly the smaller ratio of peptide bonds to charges, which will be discussed in more details later. The complexation at these extreme non-stoichiometric ratios was already studied for DNA/divalent counterion system in the last chapter and is not completely understood for this system either. However, at this point, the further focus thus is on higher valent oligolysines.

5.4.2 Association of NaPSS with Tetralysine

The association of tetralysine with low molecular weight NaPSS was also carried out in different polymer concentrations (c(NaPSS) = 0.01 gL^{-1} and 0.05 gL^{-1}). Examples of complexation at c(NaPSS) = 0.05 gL^{-1} are presented in Figure 5.4.2.1. Well defined distributions are observed in light scattering at charge ratios of 0.43 and 0.67 (black curves) after sample preparation. However, significant changes in the autocorrelation function are detected when the same sample is measured the next day (red curves). The appearance of a second peak at faster relaxation time again indicates the presence of uncomplexed polymer molecules. It implies that the complex decomposes or precipitates on a time scale of one day. The aggregation that occurs at c(NaPSS) = 0.01 gL^{-1} exhibits similar behavior. These results suggest that the complexes produced by low molecular weight NaPSS and tetralysine are not as stable as the aggregates formed by high molecular weight NaPSS and trilysine.

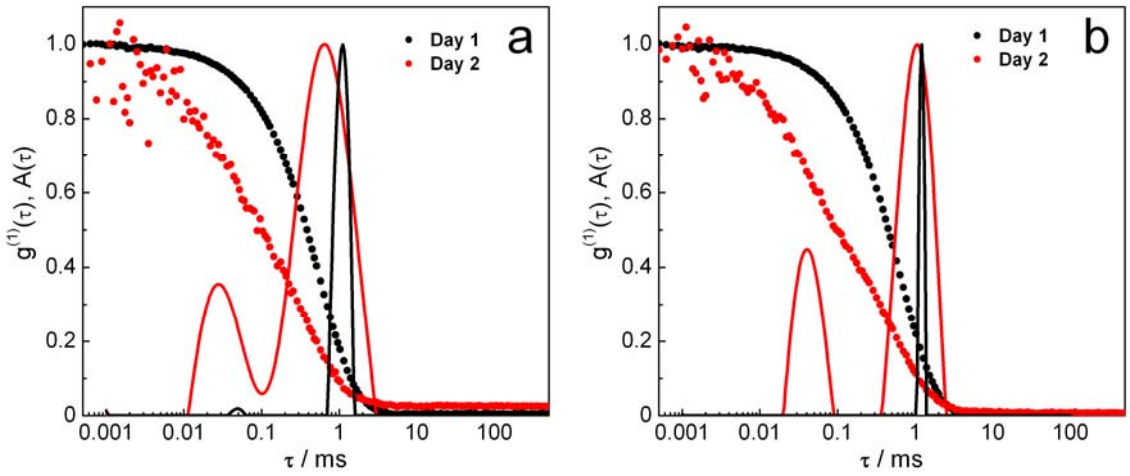

Figure 5.4.2.1 Normalized electric field autocorrelation functions $g^{(1)}(\tau)$ and relaxation times distributions $A(\tau)$ at a scattering angle of 90° of complexes induced by low molecular weight NaPSS and tetralysine at charge ratio of (a) 0.43 and (b) 0.67; (all: c(NaPSS) = 0.05 gL^{-1})

Furthermore, the light scattering results of the aggregation of high molecular weight NaPSS with tetralysine are shown in Figure 5.4.2.2. The concentration of NaPSS applied here is 0.01 gL^{-1}. Monomodel narrow distributions are obtained for samples at charge ratio $l \geq 5$. The R_H of those samples is around 84 nm and 145 nm for complex at charge ratio l = 5 and l = 10, respectively. The association behavior, as well as the size of the complex is comparable to those observed for high molecular weight NaPSS/trilysine system at the same NaPSS concentration. It is thus expected that complexes at stoichiometric ratio can also be obtained by increasing the polymer concentration for this combination. The influence of the polymer concentration was already demonstrated for high molecular weight NaPSS/trilysine system in Chapter 5.3.

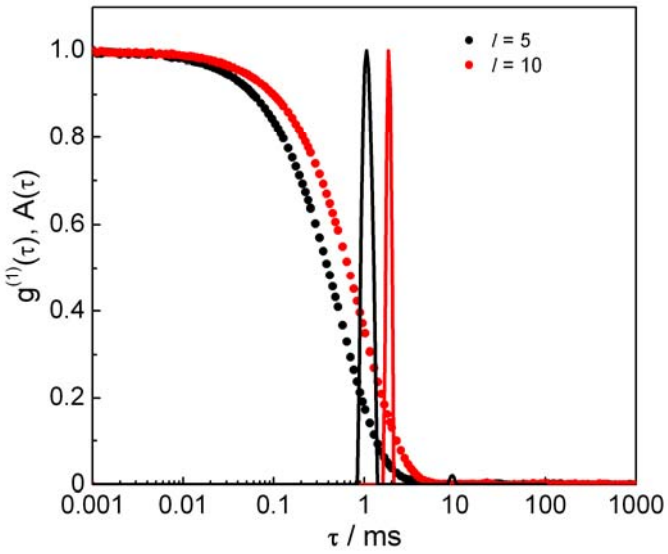

Figure 5.4.2.2 Normalized electric field autocorrelation functions $g^{(1)}(\tau)$ and relaxation times distributions $A(\tau)$ at a scattering angle of 90° for assemblies composed of high molecular weight NaPSS and tetralysine at different charge ratios; (all: c(NaPSS) = 0.01 gL^{-1})

5.4.3 Association of NaPSS with Pentalysine

Finally, pentalysine was combined with the different molecular weight NaPSS. Figure 5.4.3.1a shows the autocorrelation functions and relaxation times distributions of the sample induced by pentalysine and different NaPSS. Complexes with narrow size distributions are obtained for low molecular weight NaPSS at charge ratio l = 0.77, while well defined aggregates are observed for high molecular weight NaPSS at charge ratio $l \geq 0.77$. The diffusion coefficients as function of scattering vector square for complexes induced by pentalysine and both NaPSS are shown in Figure 5.4.3.1b as an example. Extrapolating the diffusion coefficient to zero scattering vector yields a hydrodynamic radius around 63 nm and 256 nm for low and high molecular weight NaPSS, respectively. Furthermore, both samples are stable for at least few days.

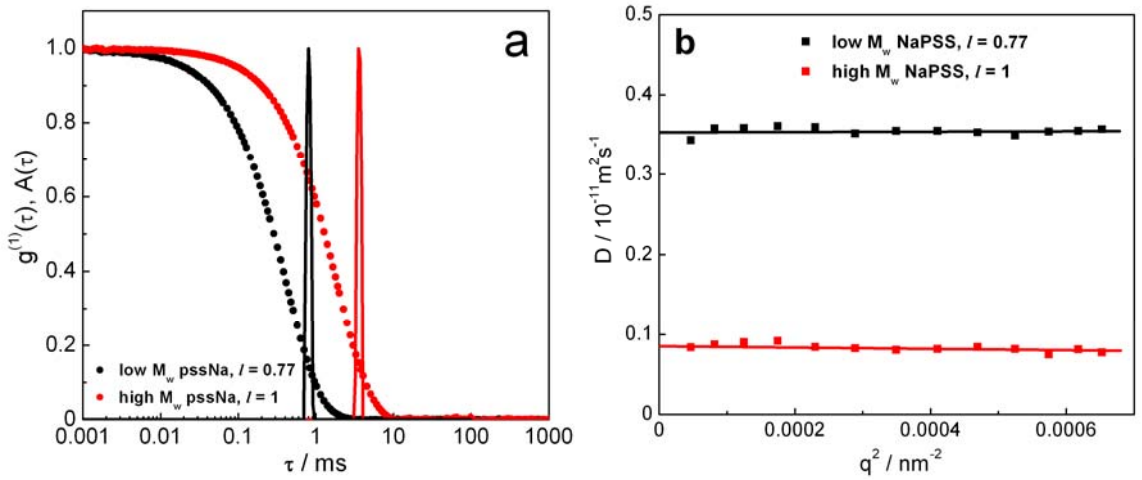

Figure 5.4.3.1 (a)Normalized electric field autocorrelation functions $g^{(1)}(\tau)$ and relaxation times distributions $A(\tau)$ at a scattering angle of 90° and (b) diffusion coefficient as a function of scattering vector square for aggregates produced by pentalysine and different molecular weight NaPSS; (all: c(NaPSS) = 0.01 gL^{-1})

Figure 5.4.3.2 displays the SLS data of the assembly formed by low molecular weight NaPSS and pentalysine at charge ratio of I = 0.77. Curved data are again found in Zimm and Berry plot (not shown), linear data is only obtained in a Guinier plot. From the latter, a radius of gyration $R_G \approx$ 52 nm and thus R_G/R_H ratio around 0.83 is calculated. This value is similar to that found for high molecular weight NaPSS/trilysine complexes in the regime 1 and 3 ($R_G/R_H \approx$ 0.85) and comparable to the typical value of a homogenous sphere (R_G/R_H = 0.778, considering the possible polydispersity). It thus indicates that the complex obtained here might have similar structure to that of high molecular weight NaPSS/trilysine aggregates in the regime 1 and 3, which was proven to be homogenous sphere.

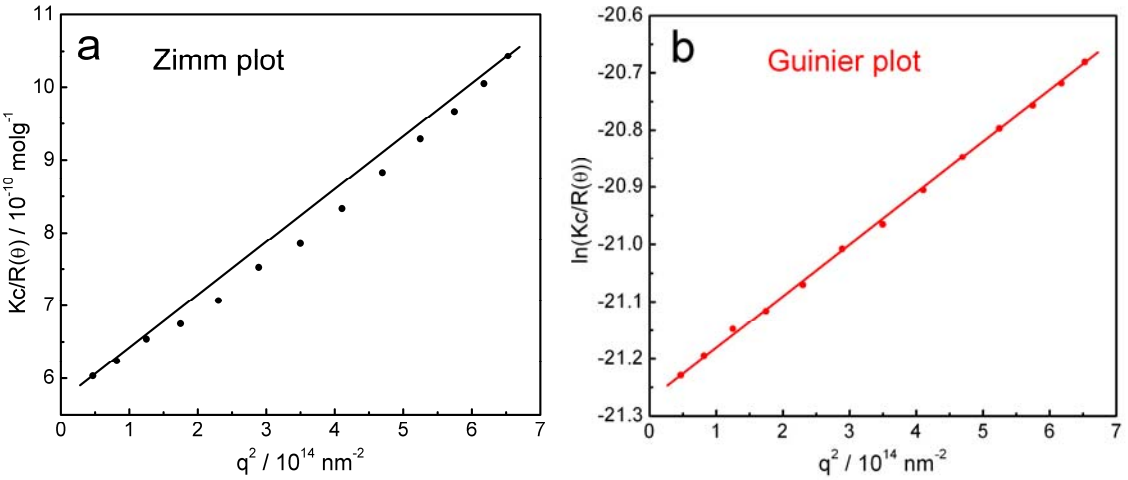

Figure 5.4.3.2 Static light scattering data for complex induced by low molecular weight NaPSS and pentalysine at charge ratio of 0.77; (a) Zimm plot, (b) Guinier plot

A summary of the series of experiments of complexation of oligolysine with NaPSS is listed in Table 5.4.3.1. It shows that high molecular weight NaPSS can form stable complexes with oligolysine for $n \geq 3$ under various conditions, while stable aggregates of low molecular weight NaPSS is only induced by pentalysine. It is evident that the complexation capability of high molecular weight NaPSS is better than that of low molecular weight NaPSS. On the other hand, pentalysine can induce stable assemblies with both high and low molecular weight NaPSS. Tetralysine and trilysine form stable complexes with high molecular weight NaPSS, but not stable complexes with low molecular weight NaPSS. Dilysine only induces aggregation of high molecular weight NaPSS at large excess amount of counterions, while it fails to form complexes with low molecular weight NaPSS. It thus clearly shows that the complexation ability of oligolysine decreases with reducing chain length of oligolysine. This behavior is in analogy to the results of complexation of oligolysine with DNA reported by Thomas et al., while they only investigated the oligolysine with $n \geq 3$ and found that trilysine failed to provoke the aggregation of DNA.[88]

NaPSS	High molecular weight NaPSS (M_w = 9.4·10^5 gmol^{-1})					Low molecular weight NaPSS (M_w = 3.3·10^4 gmol^{-1})					
oligolysine	Lys_2	Lys_3		Lys_4	Lys_5	Lys_2		Lys_3	Lys_4		Lys_5
c(NaPSS)	0.01	0.01	0.1	0.01	0.01	0.01	0.1	0.05	0.01	0.05	0.01
charge ratio	$l \geq 50$	$l \geq 5$	$0.91 \leq l \leq 2$	$l \geq 5$	$l \geq 0.77$	$l \geq 50$	$l = 50$	$l = 10$	$0.5 \leq l \leq 1$	$0.43 \leq l \leq 0.67$	$l = 0.77$
complexation	complexes formed at $l \geq 100$	stable complexes with monomodel distribution, R_H is in the range between 65 nm to 256 nm				no complexes		no stable complex			stable complexes with monomodel distribution R_H= 67 nm

Table 5.4.3.1. Summary of a series of experimental results

As already addressed before, an electrostatic self-assembly process exhibits negative free energy which consists of entropic and enthalpic contributions. The entropic contribution (ΔS) could be positive (entropy gain) due to the release of counterions and/or water molecules from the hydration shells of the components [180, 181] or negative (entropy loss) due to the rearrangement of molecules into an ordered structure.[24] The enthalpy change (ΔH) contains the contributions from all kinds of interactions, such as hydrogen bonding, π-π stacking and electrostatic interaction. The formation of hydrogen bonding and π-π stacking are all exothermic, which brings a negative enthalpy change. However, depending on the system, the electrostatic interaction could be endothermic or exothermic. For example, it was shown that binding of trilysine and oligolysines to DNA[86] or binding of Ca^{2+} ions to NaPAA[181] is an endothermic process. In contrast to that, the electrostatic interaction in the dendrimer/dye system is exothermic.[24]

Although it is difficult to conclude whether the system considered here is entropically and/or enthalpically driven, it is possible to explain the experimental findings above. It is evident that under otherwise same conditions (salt concentration, counterion type etc.), higher molecular weight NaPSS contains more charges and binding sites for its counterions (Na^+) on each chain. The higher valence generates stronger electrostatic attractive force and more binding

sites allow more counterions to be released from one polymer chain. Thus, both increase in electrostatic attraction and entropy gain enhance the tendency of complexation with higher molecular weight NaPSS, as is found experimentally in this chapter. The better complexation ability for oligolysine with increasing chain length is simply due to the increase of the valence (same reason as for the polyelectrolyte) and the increase of the ratio of peptide bonds to charges (for oligolysine with chain length n, there are n net positive charges and (n - 1) sites for possible hydrogen bonds). It has been reported that the enthalpy change for the conformation transition of oligopeptides and polypeptides is in-between -3.8 kJ/mol to -4.6 kJ/mol per residue and the major contribution to this enthalpy change comes from the peptide hydrogen bonds.[166, 182 , 183] Therefore, the enthalpy change of forming one hydrogen bond in oligopeptides can be estimated approximately in-between -7.6 kJ/mol to -9.2 kJ/mol. On the other hand, the enthalpy change of small organic counterions (such as trilysine, cobalt hexamine and spermidine) binding to DNA due to the electrostatic interaction is in the range of $1.25 \cdot 10^{-3}$ kJ/mol to $4.91 \cdot 0^{-3}$ kJ/mol per charge.[86,184] Considering these systems as references, the binding of oligolysines to NaPSS likely is also an exothermic process when hydrogen bonds are formed. The increasing amount of peptide bonds may provide more possibilities for hydrogen bonds, which increases the negative enthalpy change and thus enhances the tendency of complexation. In addition, the higher valency again provides a stronger electrostatic force. Both effects thus lead to a better association ability for oligolysine with longer chain length. This is also the explanation for the observation that with the same molecular weight of NaPSS, increasing the polymer concentration requires a smaller charge ratio (less lysine molecules) for compelxation.

5.5 Conclusions

In this study, the association of NaPSS with oligolysines was investigated. Different molecular weights of NaPSS and oligolysine with various lengths were compared. For high molecular weight NaPSS (M_w = 9.4·10^5 gmol^{-1}), complexation with dilysine only occurred at high charge ratio (l ≥ 100), which is in analogy to that of DNA/divalent counterion system. Stable and well defined complexes were obtained at stoichiometric ratio for oligolysines with $n \geq 3$. For low molecular weight NaPSS (M_w = 3.3·10^4 gmol^{-1}), stable complexes only resulted with pentalysine. The association behavior is similar to that of high molecular weight NaPSS/trilysine system. Assemblies formed with low molecular weight NaPSS and oligolysine with lysine units less than 5 were not stable on the time scale of a few days. Thus, the higher molecular weight NaPSS exhibited a stronger complexation capability. This can be well explained by thermodynamics. On the other hand, oligolysine with increasing lysine unit showed better complexation ability with NaPSS, which is due to the increase of electrostatic attraction and potential hydrogen bonding between the molecules.

Complexes formed by high molecular weight NaPSS and trilysine in salt free solution were studied in detail. The light scattering and atomic force microscopy revealed different behaviors and supramolecular structures formed according to the charge ratio. Spherical particles were obtained on APTES modified mica for sample with charge ratio l = 0.91 (regime 1) and l = 1.5 (regime 3), while the complex at charge ratio l = 1.2 (regime 2) can only be imaged on bare mica and exhibited a somehow different structure by comparing the ratio of the aggregate volume in dried state and in solution. ATR-IR measurements directly proved the formation of hydrogen bonds in the NaPSS/trilysine system. The hydrogen bonding was suggested to play an important role in causing the different behaviors of the aggregates with various charge ratios. In addition, the overall polyelectrolyte concentration also exhibited essential influence on the association

behavior. The aggregation of NaPSS and trilysine at c(NaPSS) = 0.01 gL^{-1} only occurred at charge ratio $l \geq 5$, while the complexation at c(NaPSS) = 0.1 gL^{-1} took place at stoichiometric ratios.

The systematic study in this chapter extended the concept of complexation of oligolysine to a synthetic polyelectrolyte (NaPSS) with different molecular weights. The shortest oligolysine molecule which could induce aggregation of NaPSS was extended to dilysine (under certain conditions). It is also the first time that supramolecular structures formed by a simple linear polyelectrolyte and trilysine at stoichiometric ratios are reported. The existence of hydrogen bonds in such system, which likely caused the different association behaviors as revealed in light scattering and AFM, might attract new attentions in designing supramolecular structures with more complicate oligopeptides. The high water content in the resulted complexes indicated a big space in the particle, which might be used for delivery system. The results of this model system presented here are also helpful for understanding of DNA/protein interactions and for further study on complexation of DNA/oligopeptide system.

However, there is still a question remaining in this study. The exact assembly structure of the sample with charge ratio of 1.2 (regime 2) is not confirmed yet. More detailed information about the structure might be obtained from small angle neutron scattering (SANS).

CHAPTER 6. POLYELECTROLYTE ASSEMBLIES IN AFM

6.1 Introduction

AFM is a powerful and relatively new technique for imaging nano objects, especially biological molecules and their complexes. However, investigating complex morphology requires extra considerations. Unlike other particles governed by covalent bond, the polyelectrolyte complexes are formed by self-assembly via electrostatic interaction, hydrogen bonding, π-π interaction and/or hydrophobic interaction. It means that the conformation of charged polyelectrolyte and the morphology and composition of polyelectrolyte complexes may change significantly when interacting with a charged surface. Although there have been plenty of studies on the effects of substrate on the conformation of polyelectrolyte,[185,186,187] few of them focused on the influence on complexes. Besteman et al. reported the morphology difference of DNA assemblies on bare mica, graphite and polylysine coated mica.[137] They showed that among those chemically distinct surfaces, negatively charged bare mica disturbed the bulk condensate morphology the most and resulted in the most flattened structure. Klinov et al. investigated the effect of supporting substrates on the structure of DNA/trivaline complexes.[188] It was found that DNA complexes undergo significant structural distortions on bare mica, while regular structure remained intact on a glow discharged highly ordered pyrolytic graphite (HOPG) surface. However, no general results existed allowing to select the appropriate surface, which should minimize the influence on the morphology of self-assembly polyelectrolyte complexes.

In this chapter, both positively and negatively charged aggregates, the charge of which is indicated by zeta potential measurements, are chosen as model systems for AFM study. The negatively charged systems are NaPSS/trilysine assemblies which were introduced in Chapter 5. The positively charged system involves cationic generation 4 poly(amidoamine) dendrimer (PAMAM G4) and oppositely charged aromatic azo-dye acid red 27 (Ar27). Their molecular structures are shown in Figure 6.1.1. The compelxation behaviors of this system were described elsewhere.[24] We herein only focus on the morphology changes of the positive particles due to the various charge properties of the interacting surface. Based on those results, a general rule for the surface selection is proposed. In addition, other influences, such as sample preparation methods and salt effect, are investigated.

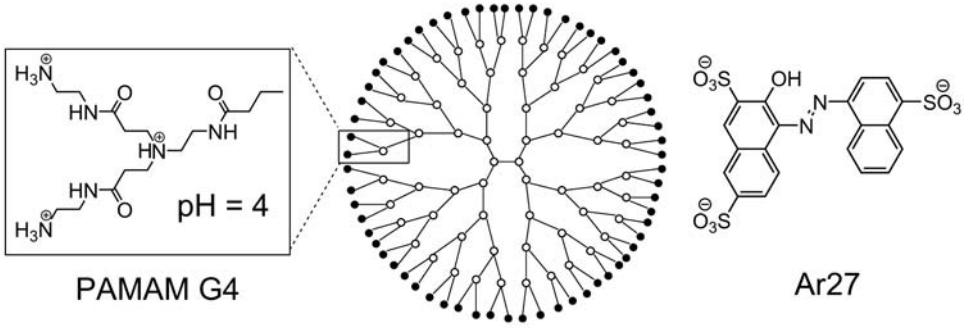

Figure 6.1.1. Molecular structures of PAMAM G4 dendrimer and counterion AR27[189]

Mica is the most commonly used substrate in AFM measurements. It has a negatively charged surface. Therefore in this study, APTES solution is applied to modify the mica if a positively charged surface is required. The surface charge density can be easily controlled by the concentration of the applied APTES solution.

6.2 Influence of Surface Charge

In Chapter 4 and 5, the influence of surface charge properties on the structure of polyelectrolytes (supercoiled pUC19, NaPSS) was already demonstrated. In this section, the emphasis is on assembly morphology changes caused by different surfaces which differ in their charge properties. First, a NaPSS/trilysine complex with negative zeta potential of ζ = -6.85 mV was investigated. The charge ratio of this sample is l = 1.5 and the structure of the particle was shown to be spherical (see Chapter 5.2). The AFM images of this sample on surfaces with different charge properties are presented in Figure 6.2.1. It is evident that mostly disassembled polymers, as well as few residuals of broken complexes (marked with arrows), are observed on the negatively charged mica surface (Figure 6.2.1a). As shown in Figure 6.2.1b, spherical aggregates (marked with black arrows) as well as some particles with distinct lower height (marked with white arrows) are coexisting on a positively charged surface with low charge density (0.01% APTES modified mica). The “unsharp” particles likely are incompletely disassembled complexes. When the surface is modified with 0.1% APTES solution, i.e. somewhat more positively charged, spherical particles and no broken complexes are visible in the image (Figure 6.2.1c). Further increasing the surface charge density by modifying the mica with 1% APTES solution does not show spherical complexes again. Only clusters of NaPSS molecules are found on this surface. It is evident from the results that the complexes are most stable on 0.1% APTES modified mica than any other surfaces. When the surface is negatively charged, the complexes do not attach to the surface and/or become decomposed due to the repulsive interaction between surface and negative particles. On 0.01% APTES modified mica, the positively charged surface enables to stabilize some spherical particles, however, the low surface charge density is not sufficient to stabilize all the particles. Therefore incompletely broken complexes are also present. On the surface with highest positive charge density (1% APTES modified mica), almost all the aggregates are disintegrated

because of the strong attractive interaction between the surface and the NaPSS molecules in the aggregates. This interaction is sufficiently strong to break the complexes and keep the clusters of NaPSS molecules on the surface.

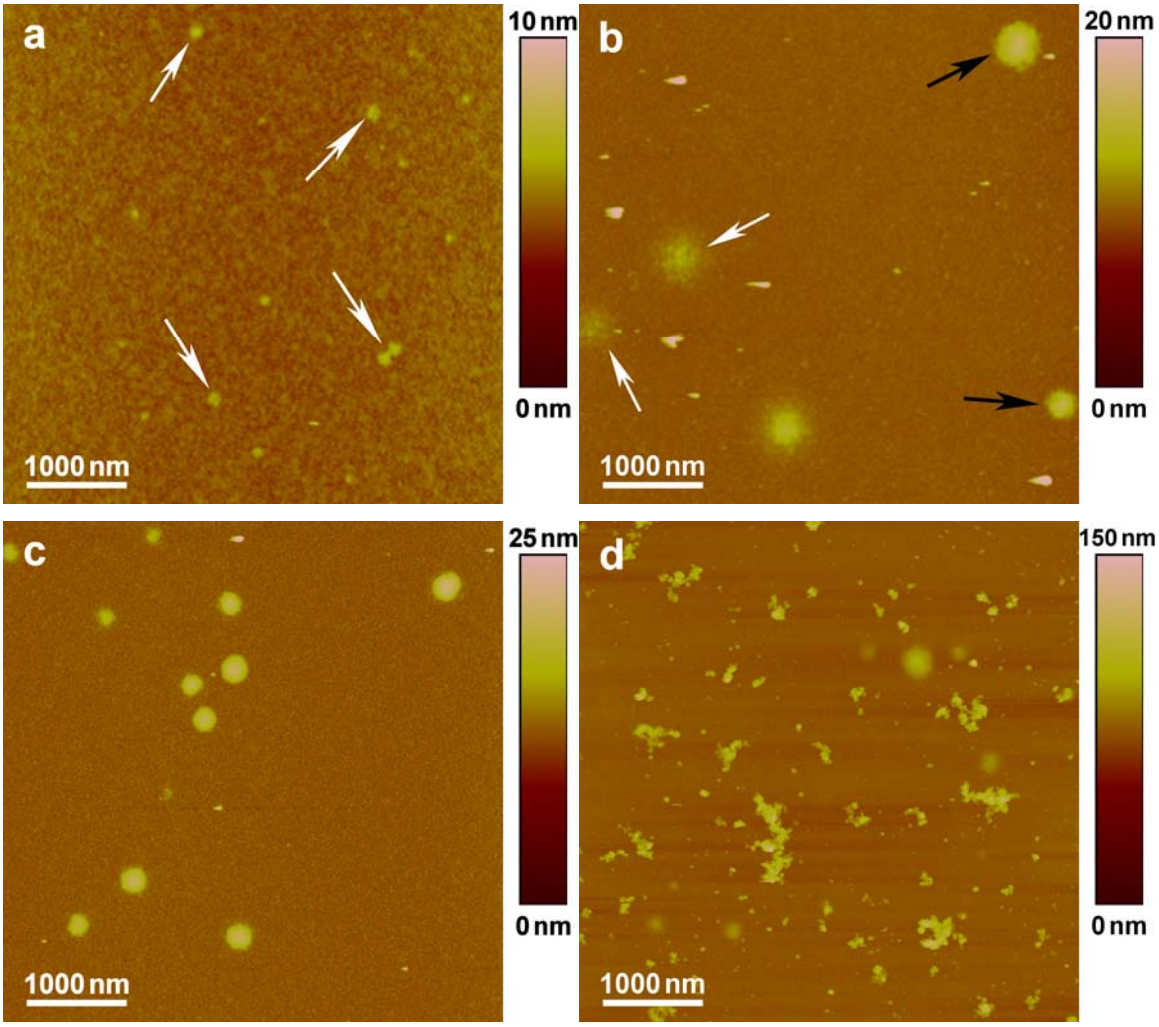

Figure 6.2.1. AFM images of complexes induced by NaPSS and trilysine at charge ratio of 1.5 on (a) bare mica, (b) 0.01% APTES modified mica, (c) 0.1% APTES modified mica and (d) 1% APTES modified mica; (all: M_w(NaPSS) = $9.4 \cdot 10^5$ gmol^{-1}, c(NaPSS) = 0.1 gL^{-1} in MQ water)

Secondly, another NaPSS/trilysine aggregate with a more negative zeta potential (ζ = -9.75 mV) was investigated. The charge ratio of the sample is l = 0.91 and the structure of the assembly was also shown to be spherical in solution by light scattering. The AFM image of this sample taken on bare mica does not show aggregated particles at all (Figure 6.2.2a). Some intermediate complexes are

observed in the images taken on 0.01% and 0.1% APTES modified micas (Figure 6.2.2b, c). Spherical assemblies are obtained only on 1% APTES modified mica (Figure 6.2.2d). These results prove again that negatively charged particles are possibly imaged on positively charged surface. However, compared to the sample before, a surface with higher charge density (1% APTES modified mica) is required for imaging the similar spherical structure due to the more negative zeta potential of this complex. It is understandable that higher positive charges are necessary to stabilize the more negatively charged aggregates.

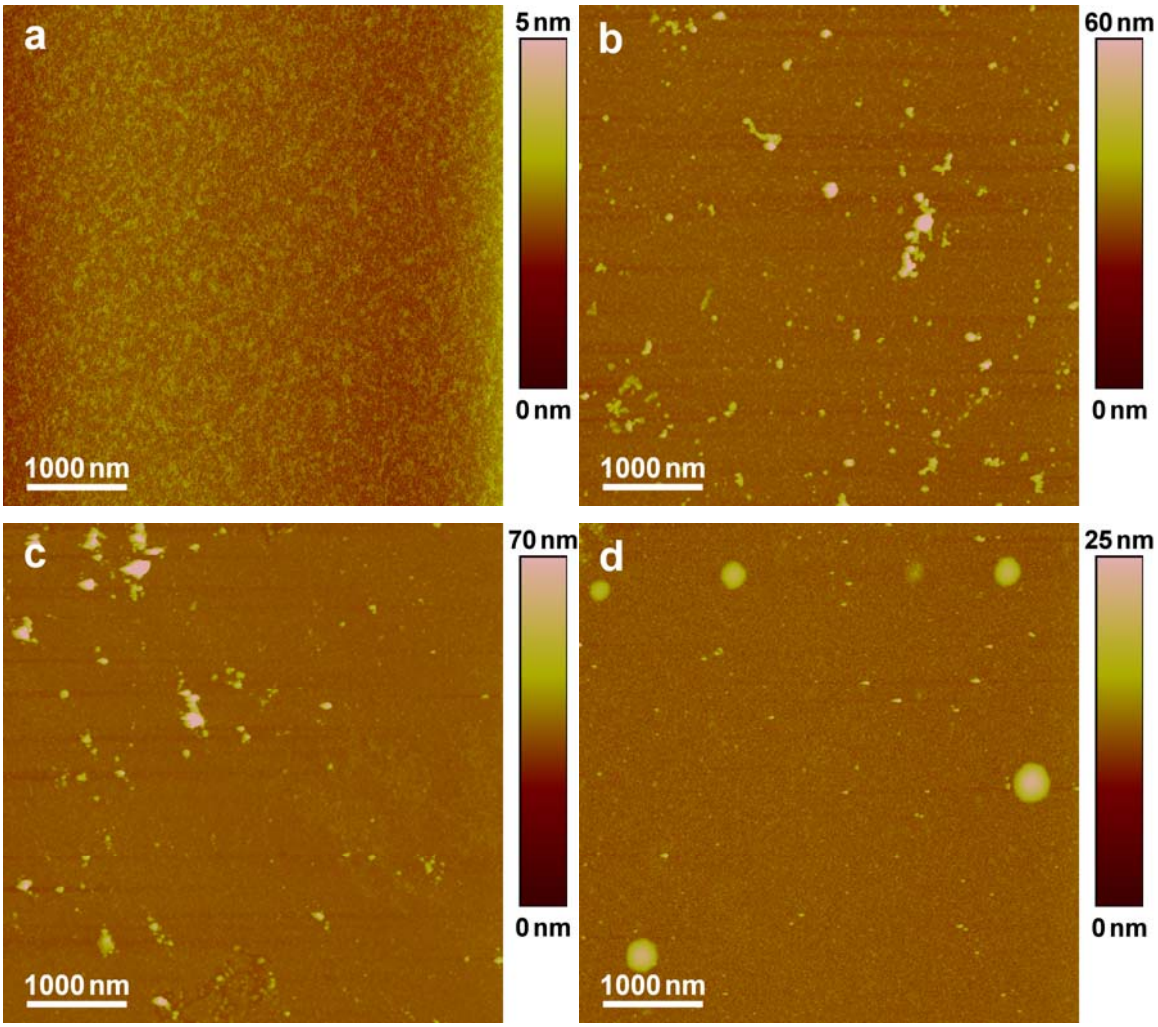

Figure 6.2.2. AFM images of aggregate formed with NaPSS and trilysine at charge ratio of 0.91 on (a) bare mica, (b) 0.01% APTES modified mica, (c) 0.1% APTES modified mica and (d) 1% APTES modified mica; (all: M_w(NaPSS) = $9.4 \cdot 10^5$ $gmol^{-1}$, c(NaPSS) = 0.1 gL^{-1} in MQ water)

Finally, a positively charged PAMAM G4/Ar27 complex (ζ = 20 mV) was investigated in AFM. The charge ratio of the sample is l = 0.91 and SANS result revealed a core-shell structure of this sample.[24] Figure 6.2.3 shows a series of AFM measurements of this sample on surfaces with different charge properties. Spherical particles are found on the negative mica surface (Figure 6.2.3a). The steps marked with arrows in the section analysis plot below indicate the core-shell structure of the assembly. When the mica surface is modified with 0.01% APTES solution, some of the complexes start to disassemble (Figure 6.2.3b, marked with arrows). If the concentration of APTES solution is increased to 0.1%, more free dendrimers are present, although spherical particles still exist (Figure 6.2.3c). On the surface with highest charge density employed in this work (1% APTES modified mica), only clusters of disintegrated dendrimers are observed (Figure 6.2.3d). It is obvious that the positively charged complexes exhibit the highest stability on negatively charged mica surface. A positively charged surface can destroy the aggregate structure due to the repulsive interactions. The higher the positive charge density, the more particles are destroyed. The result obtained here also complementarily confirms the previous findings for negatively charged complexes.

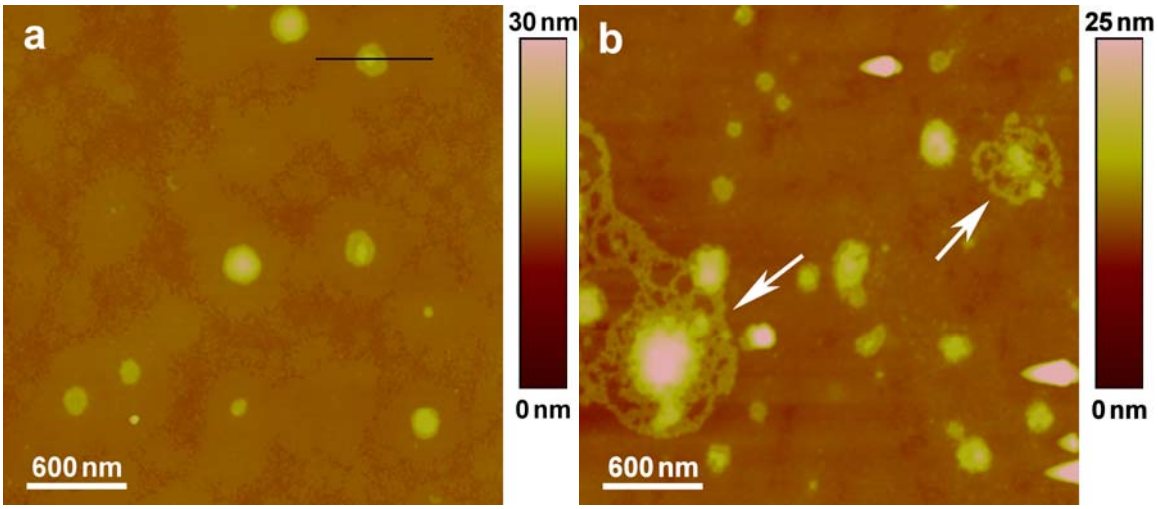

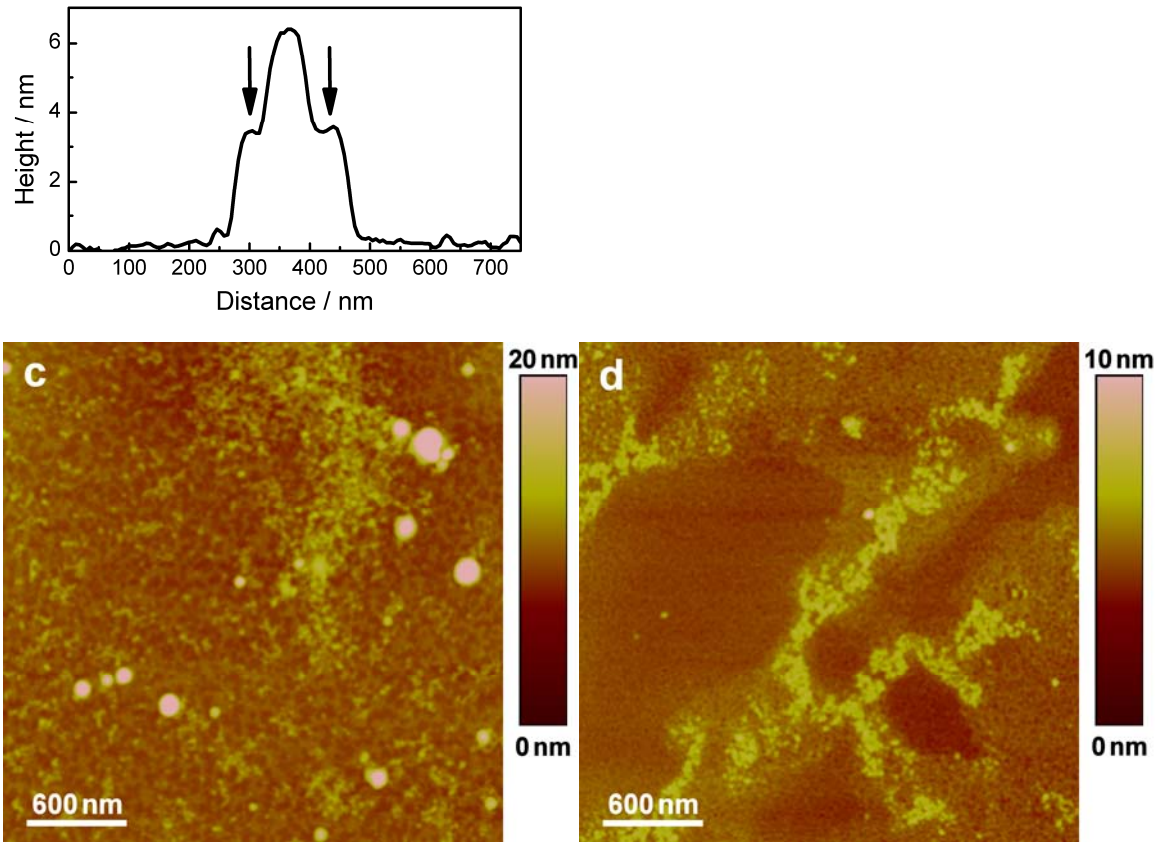

Figure 6.2.3. AFM images of aggregates induced by PAMAM G4 and Ar27 at charge ratio of 0.91 on (a) bare mica, (b) 0.01% APTES modified mica, (c) 0.1% APTES modified mica and (d) 1% APTES modified mica; (all: c(PAMAM G4) = 3.4 μM in MQ water, pH = 3.5). The section analysis plot represents the indicated lines in image (a)

Combining the results obtained from both negative and positive complexes, a general rule of selecting an appropriate surface for imaging charged aggregates can be suggested. Normally, an oppositely charged surface with moderate charge density is required to successfully image the complexes according to their zeta potential results. The oppositely charged surface is needed to immobilize and stabilize the charged self-assembly complexes, and the moderate charge density minimizes the influence of the interactions between surface and samples.

6.3 Influence of Preparation Method

There are two methods usually used to prepare a sample for AFM, which are known as drop casting and spin coating. Spin coating has a faster film formation rate and yields a more uniform thin film or well distributed particles on the surface than drop casting.[190] However, an inappropriate rotation speed can influence the complex morphology in spin coating.

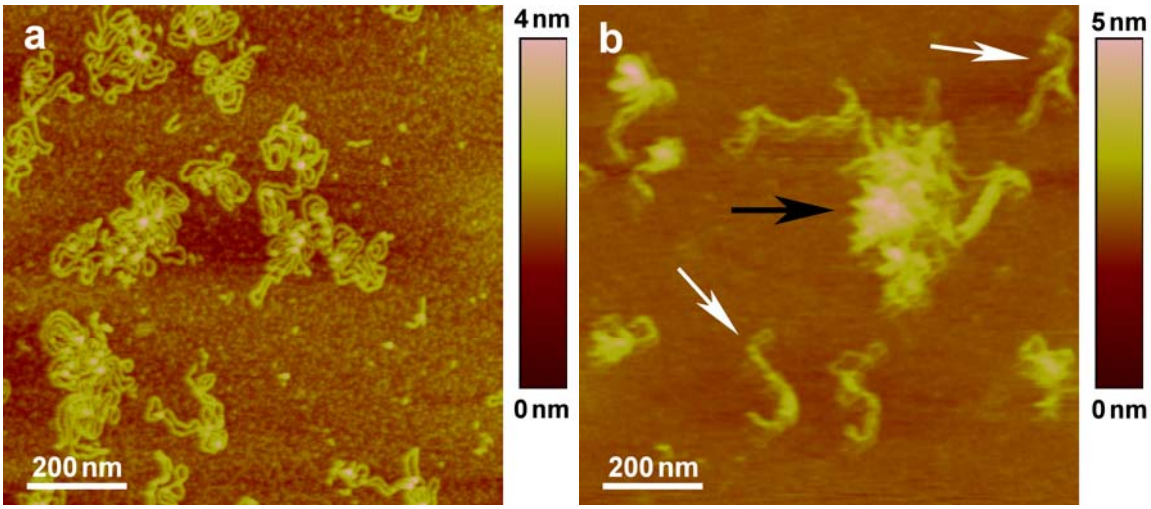

Figure 6.3.1. AFM images of complexes produced by supercoiled pUC19 and $C6T^{4+}$ at charge ratio of 1.5; (a) sample prepared by drop casting, (b) sample prepared by spin coating at 1500 rpm for 2 minutes; (all: c(DNA) = 0.01 gL^{-1} in TE buffer)

Figure 6.3.1 shows AFM images of the same sample (supercoiled pUC19/$C6T^{4+}$ at charge ratio of 1.5) prepared by different methods. It is found that the sample prepared by drop casting exhibits flower-like aggregates (Figure 6.3.1a), while the spin coated sample also presents single DNA molecules (marked with white arrows) in addition to flower-like aggregate (marked with black arrow) (Figure 6.3.1b). It shows that the drop casted sample suffers less deformation during preparation than spin coated one. The rotation speed in spin coating should thus be optimized to minimize the disturbing for the complexes. In this study, all the AFM samples in dried state were prepared by drop casting.

6.4 Influence of Added Salt

Low molecular mass salt, such as NaCl or organic ions, are usually present in polyelectrolyte solutions and later stay in its complex solution. However, the salt in the solution might interfere in AFM measurements. It could mislead the conclusion concerning the structure of the complex and/or change the size of the particles. Figure 6.4.1a shows an AFM image of a complex formed with supercoiled pUC19 and TAPP at charge ratio of 1.5 with 50 µM toluenesulfonate, which is the initial counterion of TAPP. The particles show bright area in the center. However, the edges of the particles indicate flower-like aggregates. After rinsing the sample with water, clear flower-like aggregates are observed (Figure 6.4.1b). The height of the particles after rinsing is lower than the before rinsing, which is comparable with that of DNA complexes shown in Chapter 4. It indicates that the bright area is the consequence of the aggregate covered by the toluenesulfonate ions. The structure of the complex is somehow blocked by the organic salt and better result is achieved after removing the salt by rinsing procedure.

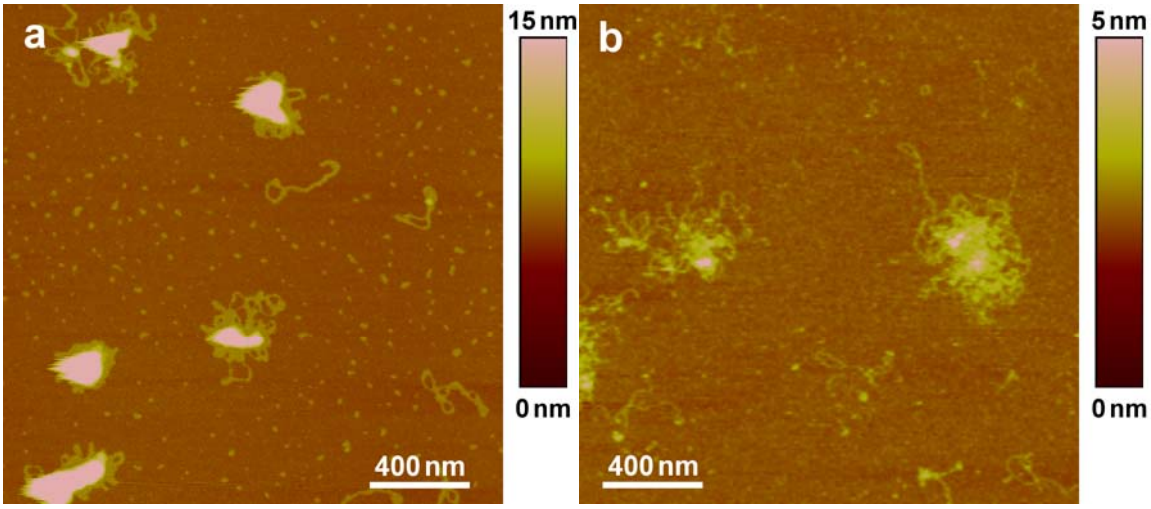

Figure 6.4.1. AFM images of complexes formed with supercoiled pUC19 and TAPP at charge ratio of 1.5 on bare mica; (a) non-rinsed sample and (b) rinsed sample; (all: c(DNA) = 0.01 gL^{-1} in MQ water)

It needs to be remarked here that the rinsing process is important for imaging polyelectrolyte complexes containing salt. However, the concentration of the complex solution changes during a rinsing process and the dilution may cause unwanted changes in the complex morphology. Apart from that, the rinsing process might also wash some of the sample off. Therefore, possible changes of the complex (morphology, size) should be considered due to the rinsing procedure. Furthermore, it also raises the question of how to immobilize the complex particles on the surface when the rinsing procedure is necessary. If a modified surface is required for immobilization, the influence of the surface charge properties should be taken into account, as discussed in the previous section.

6.5 Conclusion

In this chapter, various influences in AFM on the morphology of the charged self-assembly complexes were discussed. Series of measurements were performed for systems with either negative or positive zeta potential on substrate surfaces with different charge properties. The experimental findings supported the hypothesis that an oppositely charged surface with moderate charge density is essential for successfully imaging the self-assembly complex as it is present in solution. It showed that the selection of a suitable surface for different charged systems is an important point in AFM analysis. The conclusion drawn here might be considered as a guidance or reference for choosing the appropriate substrate for future AFM measurements.

It should be noted that although mica was only modified with APTES solution to achieve positively charged surface in this study, there are other possibilities. For example, it has been reported that mica or glass substrates can be negatively modified with reagents containing COOH group or OH group.[191,192] It might also be useful to produce surfaces with both positive and negative charges by mixing up the modification agents. Varying the sign of the charge and/or changing the surface charge density is not only valuable in AFM measurements, but also brings numerous potential applications, such as building multilayer thin film with distinct properties by layer-by-layer adsorption.

Furthermore, the same sample prepared by drop casting and spin coating were both tested in AFM. The results suggested that it needs to pay more attentions in spin coating with respect to the rotation speed. Finally, a rinsing procedure was shown to be helpful in AFM for the sample containing salt.

These results shown here demonstrated that it is possible to image electrostatically self-assembled complexes as they are present in solution but the

surface and preparation procedures need to be carefully chosen. In any case, an AFM study should be complemented by direct solution measurements where no surface interactions may change the particle morphology, such as light scattering.

CHAPTER 7. SUMMARY

In this work, two different systems were investigated to develop fundamental understanding of the self-assembly behavior of polyelectrolytes and small organic counterions with a certain geometry. Complexes formed were characterized by light scattering in solution, as well as UV-Vis spectroscopy, analytical ultracentrifugation, gel electrophoresis, zeta potential and IR spectroscopy. The morphologies of the aggregates were observed by AFM in dried state on surface. The charge ratio, the valence and the structure of the counterion were shown to represent key parameters in the complexation. The influence of polyelectrolyte type and molecular weights was also determined for the structure formed.

The association of double-strand DNA was mainly focused on non-intercalating divalent and tetravalent organic counterions. Results revealed that the divalent counterions methyl viologen (MV^{2+}) and 1,1'-(hexane-1,6-diyl)bis(4-aza-1-azoniabicyclo[2.2.2]octane ($C6D^{2+}$) only induced the assembly of DNA molecules into flower-like aggregates at very high counterion excess. It was shown that the separation of two charges of the organic molecule is essential here. The same effect was not observed for Ca^{2+} or Mg^{2+}. The tetravalent counterion 4,4-(hexane-1,6-diyl)bis(1-ethyl-1,4-diazoniabicyclo[2.2.2]octane ($C6T^{4+}$) caused aggregation at much lower charge ratios, that is around charge stoichiometry. The assemblies induced by both divalent counterions and $C6T^{4+}$ were shown to be thermodynamically controlled and yielded equilibrium structures. The aggregate morphology with these counterions was flower-like. In these aggregates, multiple DNA molecules were connected by the counterions.

The tetravalent counterion pyridinium-substituted perylene-3,4,9,10-tetra-carboxylic acid diimide (PSPDI) showed different complexation behavior than the other counterions. It exhibited a bimodal distribution at charge ratios over 1. A complete complexation process was demonstrated by visualizing the transition of complex morphologies, from non-aggregated DNA over flower-like structure to coexisting well-defined rods and toroids with mixture of those morphologies as intermediates. The comparative experiment of DNA/TAPP (meso-tetrakis(4-(*N*-trimethylammonium)phenyl)porphyrin) system did not yield rodlike or toroidal aggregates and thus suggested that the structure of PSPDI with the closest distance between positive charges of the dye molecule (0.51 nm ~ 0.54 nm) corresponding to the distance of phosphate groups on the DNA backbone may be responsible for this behavior. In contrast to other systems, DNA/PSPDI complexes generated also kinetically controlled structures. Also rods and toroids were shown to consist of multiple DNA molecules. Likely, only PSPDI has sufficient power to connect DNA molecules to its tetravalency and allows for a parallel arrangement of DNA strands due to its geometry at the same time. Supercoiled and linear DNA of the same molecular weight were compared for all counterions. The type of DNA (supercoiled or linear) showed more influence on the assemblies morphology for tetravalent counterions than divalent counterions. The association of $C6T^{4+}$ and linear DNA produced more compact structures than that with supercoiled DNA for charge ratio over 2. More rodlike particles (accordingly less amount of toroidal aggregates) was observed for the complexes induced by PSPDI and linear DNA compared to that with supercoiled DNA.

The study on the aggregation of DNA and organic counterions demonstrated the importance of valence and geometry of the counterion in the complexation. This is the first time that flower-like structures are reported for the assembly of DNA with only divalent counterions. The complete process of DNA aggregation from flower-like aggregates to rods and toroids, as revealed by AFM, was observed for the first time. The stability of the complexes with a certain size and shape in solution, i.e. the stop of growth at a finite size was explained by the charged

nature of the assemblies. It is in accordance with theoretical considerations on the formation of biomacromolecule bundles, e.g. by Pincus. The DNA-counterion system thus can be regarded as a model system for electrostatic self-assembly of polyelectrolytes and stiff counterions that do not interact mutually (i.e. no π-π stacking or hydrogen bonding can be formed in-between counterions). Electrostatics and geometric factors can direct the structure formation and cause the formation of stable assemblies with finite size. This establishes a new brand of electrostatic self-assembly and may be the key to versatile and functional supramolecular structures.

Along these lines, such composite assemblies of DNA and synthetic counterions representing defined entities on a surface may be of interest for further kinds of applications by taking advantage of optical and electrical properties of the counterions. The findings of this study are thus not only of importance for a basic understanding of formation of DNA complexes with small synthetic counterions, but may also have an impact on various applications of ionic DNA assemblies, for example, in gene therapy or drug delivery systems.

The other model system investigated in this work involved linear NaPSS and oligolysine. Different molecular weights of NaPSS and oligolysine with various lengths were compared. For high molecular weight NaPSS (M_w = 9.4·10^5 gmol^{-1}), complexation with dilysine only occurred at high charge ratio (l ≥ 100). Stable and well defined complexes were obtained at stoichiometric ratio for oligolysines with $n \geq 3$. For low molecular weight NaPSS (M_w = 3.3·10^4 gmol^{-1}), stable complexes only resulted with pentalysine. Thereby, the higher molecular weight NaPSS exhibited a stronger complexation capability, which can be well explained by the increase of electrostatic interaction and entropy gain with the number of charges. On the other hand, oligolysine with increasing lysine unit also showed better complexation ability with NaPSS, which is due to the increase of electrostatic attraction and of potential hydrogen bonding between the molecules. Complexes formed with high molecular weight NaPSS and trilysine were studied

in detail. The light scattering and atomic force microscopy revealed different association behavior and supramolecular structures according to the charge ratio. Spherical particles were obtained on APTES modified mica for sample with charge ratio l = 0.91 (regime 1) and l = 1.5 (regime 3), while the complex at charge ratio l = 1.2 (regime 2) can only be imaged on bare mica and exhibited a different structure. The ATR-IR measurements directly proved the formation of hydrogen bonds in the NaPSS/trilysine system. The hydrogen bonding was suggested to play an important role in causing the different behaviors of the aggregates with various charge ratios.

The systematic study of NaPSS/oligolysine system successfully extended the concept of complexation of oligolysine from DNA to a synthetic polyelectrolyte (NaPSS) and in particular to the structural analysis of the resulting aggregates. The shortest oligolysine molecule which can induce aggregation of NaPSS was shown to be dilysine under certain conditions. It is also the first time that the supramolecular structures formed by simple polyelectrolyte and trilysine at stoichiometric ratios are investigated. The existence of hydrogen bonds in such system, which likely caused the different association behaviors as revealed in light scattering and AFM, opens a further route to design supramolecular structures and may be extended for example to more complicate oligopeptides. The high water content in the resulting complexes indicated a large available space in the particle, which might be used for delivery system. The results of this model system presented here may also be of value for understanding of DNA/protein interactions.

Finally, various influences on the morphology of the charged self-assembly complexes in AFM studies were discussed. A series of measurements were performed for systems with either negative or positive zeta potential on substrate surfaces with different charge properties. The experimental findings supported the hypothesis that an oppositely charged surface with moderate charge density is essential for successfully imaging the electrostatically self-assembled complex

as it is present in solution, although an exception was also observed, possibly due to a secondary interaction in addition to electrostatic force. It showed that the selection of a suitable surface for different charged systems is an important point in AFM analysis. The conclusion drawn here might be considered as a guidance or reference for choosing the appropriate substrate in AFM for different charged self-assembly samples, while it also demonstrated the advantage of complementary light scattering and AFM studies.

In conclusion, it was shown that electrostatic self-assembly of DNA and non-intercalating counterions as well as of a linear synthetic polyelectrolyte with oligolysine counterions that can build mutual hydrogen bonds can yield supramolecular aggregates of a defined size. Results presented in this work are of importance for the fundamental understanding of the association behavior of various polyelectrolytes and organic counterions. The selection of biopolymers for the study may give an opportunity to transfer the basic research results into biological applications, such as gene therapy or drug delivery.

CHAPTER 8. EXPERIMENTAL SECTION

Chemicals

Methyl viologen dichloride hydrate, dilysine, trilysine, tetralysine, pentalysine (Sigma-Aldrich) and sodium polystyrene sulfonate (Polymer Standards Service GmbH, Germany) were used as received. The synthesis of counterions 1,1'-(hexane-1,6-diyl)bis(4-aza-1-azoniabicyclo[2.2.2]octane) ($C6D^{2+}$), 4,4'-(hexane-1,6-diyl)bis(1-ethyl-1,4-diazoniabicyclo[2.2.2]octane) ($C6T^{4+}$) and pyridinium-substituted perylene-3,4,9,10-tetracarboxylic acid diimide chromophore (PSPDI) were described elsewhere.[107]

Unless otherwise stated, all other solvents and reagents were obtained from commercial suppliers: Sigma-Aldrich, GE Healthcare, Pierce and Fermentas and used without further purification. In all experiments MQ standard water (Millipore Inc., USA) with a typical resistivity of 18.2 MΩ/cm was used.

Supercoiled pUC19

The pUC19 supercoiled DNA (Elim-Biopharmaceuticals, Inc., USA) was used as received. The degree of supercoiling is higher than 90% as specified by the supplier. pUC19 DNA contains 2686 base pairs and has a theoretical molar mass of $1.74 \cdot 10^6$ g mol^{-1}.

Linear pUC19

The pUC19 linear DNA was obtained from the same supercoiled DNA by incubation with restriction enzyme BamHI (Fermentas, Germany) at 37°C for 1 hour. The composition of the scale-up digestion reaction is shown in Table 8.1

Composition	Supercoiled pUC19	10 x Fast Digest Buffer	Enzyme BamHI	MQ water
Amount	500 µg	500 µL	200 µL	up to 5000 µL

Table 8.1. Composition of the scale-up digestion reaction

The digestion mixture was characterized and confirmed by agarose gel electrophoresis. Then the DNA solution was purified by phenol/chloroform extraction and precipitated with ethanol. The purification procedure was followed as below:

- Mix the solution with 0.5 volume of TE-saturated phenol and 0.5 volume of chloroform. Centrifuge the mixture at 10000 rpm for 5 min (room temperature).
- Transfer the upper phase to a fresh tube. Add an equal volume of chloroform and mix the solution thoroughly. Centrifuge the mixture at 10000 rpm for 5 min (room temperature).
- Transfer the upper phase to a fresh tube. Add 1/10 volume of 3 M sodium acetate or 2 M sodium chloride.
- Add 2.5 volumes of ethanol to precipitate DNA.
- Incubate the mixture for 30-60 min at -20°C.
- Centrifuge the mixture for 10 min at 10000 rpm, then discard the supernatant and rinse the pellet twice with 70% cold ethanol.
- Air-dry the pellet. Dissolve in water, nuclease-free or TE buffer for further use.

Complex Preparation

The polyelectrolytes and the respective counterions were dissolved in either 1 x TE buffer (10 mM tris(hydroxymethyl)aminomethane(Tris)-HCl, 1 mM ethylene diamine tetra acetic acid (EDTA), pH = 7.5) or MQ-water. For DNA complexes, a counterion stock solution was added dropwise into the DNA solution to result in a desired DNA concentration and charge ratio. The typical concentration of the

counterion stock solution was: c(MV^{2+}) = (1 ~ 7) gL^{-1}, c($C6D^{2+}$) = (2 ~ 14) gL^{-1}, c($C6T^{4+}$) = (0.2 ~ 0.3) gL^{-1}, c(PSPDI) = (0.07 ~ 0.3) gL^{-1}. For NaPSS/oligolysine complexes, the NaPSS solution was first prepared at a desired concentration and then a tiny amount (few microliter) of counterion stock solution was added into the NaPSS solution by pipette to result in a desired charge ratio. The typical concentration of the oligolysine stock solution was in the range of 1 gL^{-1} to 4 gL^{-1}. The mixed solution was normally incubated overnight before further characterizations. The opposite mixing order was also tested.

Dynamic and Static Light Scattering

Light scattering experiments were performed with an ALV set up with goniometer and an ALV 5000 full digital correlator (ALV-GmbH, Germany). A Uniphase He-Ne laser (22 mW output power, 632.8 nm wavelength) or a infrared laser (80 mW output power, 831.5 nm wavelength) was used. The scattered intensity was divided by a beam splitter (approximately 55:45), each portion of which was detected by a photomultiplier. The two signals were cross-correlated in order to eliminate nonrandom electronic noise. Both dynamic and static light scattering were carried out at a temperature T = 20°C and in a scattering angle range 30° ≤ θ ≤ 150° (50° ≤ θ ≤ 110° for the IR laser) in steps of 10°. Dynamic light scattering data were analyzed by inverse Laplace Transformation of the electric field autocorrelation function using a constrained regularization method (CONTIN).

For DNA complexes, the samples were prepared in dust-free Ø 20 mm quartz cuvettes (Hellma) by either filtering the sample solutions with 0.45 µm LCR filters (Millipore Inc., USA) or in case of the PSPDI complexes by mixing the pre-filtered stock solutions. UV-Vis absorption measurements were used to check for sample loss upon filtration. For NaPSS/oligolysine complexes, the NaPSS and oligolysine stock solutions were pre-filtrated with 0.45 µm LCR filters and then the samples were prepared in Ø 20 mm dust-free quartz cuvettes by adding the

counterion stock solution into the NaPSS solution with pipette without further filtrations.

AFM imaging

AFM images were taken both in air and liquid. All the measurements were recorded on a MultiMode Nanoscope IIIa Atomic Force Microscope (Veeco Instruments, California, USA) in tapping mode at room temperature. Typical imaging parameters were: (1) working oscillation amplitude: 1.0 V ~ 1.5 V; (2) scan rate: 0.5 Hz ~ 1 Hz; (3) image resolution: 512x512 pixels. For imaging in air, a silicon cantilever (OMCLAC 160 TS-W, Olympus, Japan) with 42 Nm^{-1} spring constant and nominal tip radius < 10 nm was used. The working frequencies of the cantilever were between 300 kHz to 400 kHz. For imaging in liquid, a silicon cantilever (OMCLAC 240 TS, Olympus, Japan) with 2 Nm^{-1} spring constant and nominal tip radius < 10 nm was selected. The working frequencies of this cantilever were in the range of (20 ~ 40) kHz. The raw topography data were processed by flattening to remove the background slope.

For imaging complexes in air, the sample preparation was carried out as following: normally, a (3 ~ 5) μL sample aliquot was dropped onto either 3-aminopropyltriethoxy-silane (APTES) modified mica or freshly cleaved mica, then either blow dried with N_2 directly or rinsed with 5 mL MQ-water immediately and blow dried with N_2. For imaging particles in liquid, 60 μL complex solution was usually injected into a liquid cell and then incubated for 30 ~ 60 minutes before measuring. The substrate used was also APTES modified mica.

The APTES modified mica was prepared as following: 15 μL aqueous APTES solution with various concentrations was dropped on a freshly cleaved mica surface and incubated for 10 minutes, then the surface was rinsed with 5 mL MQ water and finally air dried.

UV-Vis Spectrometry

Absorption spectra were recorded with a UV-Vis Perkin-Elmer Lambda 2 spectrometer. A stock dye solutions with c(positive charges, dye) = $1.24 \cdot 10^{-5}$ M was prepared and titrated with DNA solution with c(negative charges, DNA) = $3.1 \cdot 10^{-3}$ M.

Agarose Gel Electrophoresis

Agarose gel electrophoresis was performed with the equipments from Bio-RAD (USA). The gel composition used is shown in the Table 8.2.

1% Gel composition	Total volume	Agarose	1 x TBE Buffer	Ethidium Bromid 10 mg/mL
Amount	50 mL	0.5 g	50 mL	10 µL

Table 8.2. Composition of 1% agarose gel

Typically a (15 ~ 20) µL sample aliquot containing (10 ~ 15) µL complex solution and 5 µL loading buffer (50% aqueous glycerol solution) was injected into the slot of the gel. Normally a 100 V voltage was applied to run the gel for 70 ~ 200 minutes.

Zeta potential

Zeta potential measurements were carried out on a NICOMP™ 380 Submicron Particle Sizer (California, USA). Generally, a (2 ~ 2.5) mL complex solution was used for measurements. Each sample was measured 180 s for 3 times and the result was obtained by calculating the average value of all the measurements.

ATR-IR measurements

The ATR-IR transmission spectra were recorded using a Nicolet 730 FT-IR spectrometer (Thermo Fisher Scientific Inc.). All solution spectra represented a 256 scans with a frequency resolution of 2 cm^{-1} with respect to MQ water. Normally a 1 mL sample solution was dropped on a ZnSe crystal IR window for measurements.

LIST OF ABBREVIATIONS

AFM	Atomic Force Microscopy
APTES	3-aminopropyltriethoxysilane
Ar27	Aromatic azo-dye acid red 27
ATR-IR	Attenuated Total Reflection Infrared
bp	base pair
c	concentration
Cys	Cysteine
$C6D^{2+}$	1,1'-(hexane-1,6-diyl)bis(4-aza-1-azoniabicyclo[2.2.2]octane
$C6T^{4+}$	4,4-(hexane-1,6-diyl)bis(1-ethyl-1,4-diazoniabicyclo[2.2.2]octane
DNA	Deoxyribonucleic acid
dn/dc	refractive index increment
DP	Degree of Polymerization
DLS	Dynamic Light Scattering
EDTA	Ethylenediamine Tetraacetate
HOPG	Highly Ordered Pyrolytic Graphite
l	Charge ratio
Lys	Lysine
MQ-water	MilliQ water
M_w	Molecular weight
MV^{2+}	Methyl Viologen
NaPSS	Sodium Polystyrene Sulfonate
PAMAM G4	Generation 4 poly(amidoamine) dendrimer
PSPDI	Pyridinium-Substituted Perylene-3,4,9,10-tetracarboxylic acid diimide
pUC19	Template DNA for complexation
q	Scattering vector

R_G	Radius of gyration
R_H	Hydrodynamic radius
SANS	Small Angle Neutron Scattering
SLS	Static Light Scattering
TAPP	Meso-tetrakis(4-(*N*-trimethylammonium)phenyl)porphyrin
TEPyP	Meso-tetrakis(4-*N*-ethylpyridiumyl)porphyrin
TMPyP	Meso-tetrakis(4-*N*-methylpyridiumyl) porphyrin
TRIS	Tris(hydroxymethyl) aminomethane
Trp	Tryptophan
UV/VIS	Ultraviolet/Visible

REFERENCES AND NOTES

1. Lehn, J. M. *Science*, **1993**, *260*, 1762-1763.

2. Tecila, P.; Dixon, R. P.; Slobodkin, G.; Alavi, D. S.; Waldeck, D. H.; Hamilton, A. D. *J. Am. Chem. Soc.* **1990**, *112*, 9408.

3. Whitesides, G. M.; Mathias, J. P.; Seto, C. T. *Science* **1991**, *254*, 1312.

4. Lindsey, J. S. *New J. Chem.* **1991**, *15*, 153.

5. Gröhn, F. *Macromol. Chem. Phys.* **2008**, *209*, 2295-2301.

6. Tanford, C. *J. Mol. Biol.* **1972**, *67*, 59-74.

7. Tanford, C. *J. Phys. Chem.* **1974**, *78*, 2469-2479.

8. Zhang, L. F.; Eisenberg, A. *Science*, **1995**, *268*, 1728.

9. Discher, D. E.; Eisenberg, A. *Science*, **2002**, *297*, 967.

10. Antonietti, M.; Förster, S. *Adv. Mater.* **2003**, *15*, 1323.

11. Li, Z.; Fullhart, P.; Mirkin, C. A. *Nano Letters* **2004**, *4*, 1055.

12. Alemdaroglu, F. E; Alemdaroglu, N. C.; Langguth, P.; Herrmann, A. *Adv. Mater.* **2008**, *20*, 899–902.

13. Lehn, J. M. *Pure and Applied Chemistry*, **1980**, *52*, 2303-2319.

14. Kurth, D. G.; Fromm, K. M.; Lehn, J. M. *European Journal of Inorganic Chemistry* **2001**, *6*, 1523-1526.

15. Kolomiets, E.; Buhler, E.; Candau, S. J.; Lehn, J. M. *Macromolecules* **2006**, *39*, 1173-1181.

16. Sauvage, J. P.; Hosseini, M. W. *Comprehensive Supramolecular Chemistry, Vol 9,* Elservier Science Ltd., **1996**.

17. Li, Y.; Yildiz, U. H.; Müllen, K.; Gröhn, F. *Biomacromolecules* **2009**, *10*, 530-540.

18. Caruso, F.; Lichtenfeld, H.; Giersig, M.; Mohwald, H. *J. Am. Chem. Soc.* **1998**, *120*, 8523–8524.

19. Ladam, G.; Gergely, C.; Senger, B.; Decher, G.; Voegel, J. C.; Schaaf, P.; Cuisinier, F. J. G. *Biomacromolecules* **2000**, *1*, 674–687.

20. Dronov, R.; Kurth, D. G.; Mohwald, H.; Scheller, F. W.; Friedmann, J.; Pum, D.; Sleytr, U. B.; Lisdat, F. *Langmuir*, **2008**, *24*, 8779-8784.

21. Willerich, I.; Gröhn, F. *Chem. Eur. J.* **2008**, *14*, 9112–9116.

22. Ruthard, C.; Maskos, M.; Kolb, U.; Gröhn, F. *Macromolecules* **2009**, *42,* 830-840.

23. Reinhold, F.; Kolb, U.; Lieberwirth, I.; Gröhn, F. *Langmuir* **2009**, *25*, 1345-1351.

24. Willerich, I.; Ritter, H.; Gröhn, F. *J. Phys. Chem. B* **2009**, *113*, 3339-3354.

25. Radeva, T. *Physical Chemistry of Polyelectrolytes,* Marcel Dekker, Inc., **2001**.

26. Ma, Y. J.; Dong, W. F.; Hempenius, M. A.; Mohwald, H.; Vancso, G. J. *Nature Materials* **2006**, *5*, 724-729.

27. Heuberger, R.; Sukhorukov, G.; Voros, J.; Textor, M.; Mohwald, H. *Adv. Func. Mater.* **2005**, *15*, 357-366.

28. Crespo-Biel, O.; Dordi, B.; Reinhoudt, D. N.; Huskens, J. *J. Am. Chem. Soc.* **2005**, *127*, 7594–7600.

29. Ikeda, Y.; Beer, M.; Schmidt, M.; Huber, K. *Macromolecules* **1998**, *31*, 728–733.

30. Peng, S. F.; Wu, C. *Macromolecules* **1999**, *32*, 585–589.

31. Schweins, R.; Huber, K. *Eur. Phys. J. E* **2001**, *5*, 117–126.

32. Schweins, R.; Lindner, P.; Huber, K. *Macromolecules* **2003**, *36*, 9564–9573.

33. Koltover, I.; Salditt, T.; Rädler, J. O.; Safinya, C. R. *Science* **1998**, *281*, 78–81.

34. Zhou, S. Q.; Burger, C.; Yeh, F. J.; Chu, B. *Macromolecules* **1998**, *31,* 8157-8163.

35. Schneider G. F.; Decher G. *Nano Letters* **2008**, *8*, 3598-3604.

36. Caruso, F.; Mohwald, H. *J. Am. Chem. Soc.* **1999**, *121*, 6039–6046.

37. Gabriel, G. J.; Iverson, B. L. *J. Am. Chem. Soc.* **2002**, *124*, 15174–15175.

38. Skowronek, M.; Stopa, B.; Konieczny, L.; Rybarska, J.; Piekarska, B.; Szneler, E.; Bakalarski, G.; Roterman, I. *Biopolymers* **1998**, *46*, 267–281.
39. Gröhn, F.; Klein, K.; Brand, S. *Chem. Eur. J.* **2008**, *14*, 6866–6869.
40. Yildiz, U. H.; Koynov, K.; Gröhn, F. *Macromol. Chem. Phys.* **2009**, *210*, 1678-1690.
41. Schmuck, C.; Rehm, T.; Klein, K.; Gröhn, F. *Angew. Chem. Int. Ed.* **2007**, *46*, 1693–1697.
42. Reches, M.; Gazit, E. *Science* **2003**, *300*, 625–627.
43. Bustamante, C.; Marko, J. F.; Siggia, E. D.; Smith, S. *Science* **1994**, *265*, 1599–1600.
44. Gosule, L. C.; Schellman, J. A. *Nature* **1976**, *259*, 333–335.
45. Richards, K. E.; Williams, R. C.; Calendar, R. *J. Mol. Biol.* **1973**, *78*, 255-259.
46. Earnshaw, W. C.; King, J.; Harrison, S. C.; Eiserling, F. A. *Cell* **1978**, *14*, 559–568.
47. Rao, V. B.; Black, L. W. *J. Mol. Biol.* **1985**, *185*, 565-578.
48. Kawabe, Y.; Wang, L.; Horinouchi, S.; Ogata, N. *Adv. Mater.* **2000**, *12*, 1281–1283.
49. Suwalsky, M.; Traub, W.; Shmueli, U.; Subirana, J. A. *J. Mol. Biol.* **1969**, *42*, 363-373.
50. Laemmli, U. K. *Proc. Nat. Acad. Sci.* **1975**, *72*, 4288-4292.
51. Plum, G. E.; Arscott, P. G.; Bloomfield, V. A. *Biopolymers* **1990**, *30*, 631–643.
52. Chattoraj, D. K.; Gosule, L. C.; Schellman, J. A. *J. Mol. Biol.* **1978**, *121*, 327–337.
53. Vijayanathan, V.; Thomas, T.; Antony, T.; Shirahata, A.; Thomas, T. J. *Nucl. Acid Res.* **2004**, *32*, 127–134.
54. Arscott, P. G.; Li, A. Z.; Bloomfield, V. A. *Biopolymers* **1990**, *30*, 619–630.
55. Danielsen, S.; Varum, K. M.; Stokke, B. T. *Biomacromolecules* **2004**, *5*, 928-936.
56. Fang, Y.; Hoh, J. H. *J. Am. Chem. Soc.* **1998**, *120*, 8903–8909.
57. Manning, G. S. *Cell Biophys.* **1985**, *7*, 57–89.

58. Wilson, R. W.; Bloomfield, V. A. *Biochemistry* **1979**, *18*, 2192–2196.

59. Kelly, J. M.; Tossi, A. B.; McConnell, D. J.; OhUigin, C. *Nucl. Acid. Res.* **1985**, *13*, 6017–6034.

60. Zinchenko, A. A.; Sergeyev, V. G.; Yamabe, K.; Murata, S.; Yoshikawa, K. *ChemBioChem* **2004**, *5*, 360–368.

61. Yoshikawa, Y.; Yoshikawa, K. *FEBS Lett.* **1995**, *361*, 277–281.

62. Moreno-Herrero, F.; Herrero, P.; Moreno, F.; Colchero, J.; Gomez-Navarro, C.; Gomez-Herrero, J.; Baro, A. M. *Nanotechnology* **2003**, *14*, 128–133.

63. Pasternack, R. F.; Bustamante, C.; Collings, P. J.; Giannetto, A.; Gibbs, E. J. *J. Am. Chem. Soc.* **1993**, *115*, 5393–5399.

64. Pasternack, R. F.; Gibbs, E. J.; Villafrance, J. J. *Biochemistry* **1983**, *22*, 2406–2414.

65. Imae, T.; Hayashi, S.; Ikeda, S.; Sakaki, T. *Int. J. Biol. Macromol.* **1981**, *3*, 259–266.

66. Bradley, D. F.; Wolf, M. K. *Chemistry* **1959**, *45*, 944–952.

67. Krauß, S.; Lysetska, M.; Würthner, F. *Lett. Org. Chem.* **2005**, *2*, 349–353.

68. Mei, H.; Barton, J. K. *J. Am. Chem. Soc.* **1986**, *108*, 7414–7416.

69. Barton, J. K.; Goldberg, J. M.; Kumar, C. V.; Turro, N. J. *J. Am. Chem. Soc.* **1986**, *108*, 2081–2088.

70. Erkkila, K. E.; Odom, R. T.; Barton, J. K. *Chem. Rev.* **1999**, *99*, 2777–2795.

71. Armitage, B. *Chem. Rev.* **1998**, *98*, 1171–1200.

72. The image has been reprinted from: *http://www.jonathanpmiller.com/intercalation/B-DNA.jpg*

73. The image has been reprinted from: *http://www.spirogen.com/media/images/products/pipeline_02.jpg*

74. The image has been reprinted from: *http://www.oru.se/oru-upload/Institutioner/Naturvetenskap/Kemi/Biofysikalisk%20kemi/Fig2_1.jpg*

75. Lohman, T. M.; deHaseth, P. L.; Record, M. T. *Biochemistry* **1980**, *19*, 3522–3530.

76. Dash, P. R.; Read, M. L.; Fisher, K. D.; Howard, K. A.; Wolfert, M.; Oupicky, D.; Subr, V.; Strohalm, J.; Ulbrich, K.; Seymour, L. W. *J. Biol. Chem.* **2000**, *275*, 3793–3802.

77. Stanic, V.; Arntz, Y.; Richard, D.; Affolter, C.; Nguyen, I.; Crucifix, C.; Schultz, P.; Baehr, C.; Frisch, B.; Ogier, J. *Biomacromolecules* **2008,** *9*, 2048-2055.

78. Gupta, K.; Singh, V. P.; Kurupati, R. K.; Mann, A.; Ganguli, M.; Gupta, Y. K.; Singh, Y.; Saleem, K.; Pasha, S.; Maiti, S. *Journal of Controlled Release* **2009**, *134*, 47–54.

79. Chan, C. K.; Senden, T.; Jans, D. A. *Gene Therapy* **2000**, *7*, 1690–1697.

80. Tang, M. X.; Szoka, F. C. *Gene Therapy* **1997**, *4*, 823–832.

81. Golan, R.; Pietrasanta, L. I.; Hsieh, W.; Hansma, H. G. *Biochemistry* **1999**, *38*, 14069–14076.

82. Liu, G.; Molas, M.; Grossmann, G. A.; Pasumarthy, M.; Perales, J. C.; Cooper, M. J.; Hanson, R. W. *J. Biol. Chem.* **2001**, *276*, 34379–34387.

83. Müller, M.; Reihs, T.; Ouyang, W. *Langmuir* **2005**, *21*, 465–469.

84. Müller, M.; Ouyang, W.; Keßler, B. *International Journal of Polymer Anal. Charact.* **2007**, *12*, 35–45.

85. Latt, S. A.; Sober, H. A. *Biochemistry* **1967**, *6*, 3293–3306.

86. Giancotti, V.; Cesaro, A.; Crescenzi, V. *Biopolymers* **1975**, *14*, 676–677.

87. Wadhwa, M. S.; Collard, W. T.; Adami, R. C.; McKenzie, D. L.; Rice, K. G. *Bioconjugate Chem.* **1997**, *8*, 81–88.

88. Nayvelt, I.; Thomas, T.; Thomas, T. J. *Biomacromolecules* **2007,** *8*, 477-484.

89. Förster, S.; Schmidt, M.; Antonietti, M. *Polymer* **1990,** *31*, 781-792.

90. Drifford, M; Dalbiez, JP. *Biopolymers* **1985,** *24*, 1501-1514.

91. Schmidt, M. *Macromol. Chem. Rapid Commun.* **1989**, *10*, 89–96

92. Förster, S.; Schmidt, M.; Antonietti, M. *J. Phys. Chem.* **1992**, *96*, 4008-4014.

93. Sedlak, M.; Amis, E. J. *J. Chem. Phy.* **1992**, *96*, 826-834.

94. Kratochvil, P. *Classical Light Scattering from Polymer Solutions,* Elserier Science Publishers B. V., **1987**.

95. Gröhn, F. *Polymer Characterization-Lecture Notes,* University of Mainz, **2007**.

96. Brown, W. *Light Scattering,* Clarendon Press, Oxford, **1996**.

97. Pecora, R. *Dynamic Light Scattering,* Plenum Press, London, **1985**.

98. Brown, W. *Dynamic Light Scattering,* Clarendon Press, Oxford, **1993**.

99. The image has been reprinted from: Harding, S. E.; Jumel, K. *Current Protocols in Protein Science,* John Wiley & Sons, Inc., **1998**.

100. Morita, S; Wiesendanger, R.; Meyer, E. *Noncontact Atomic Force Microscopy,* Springer, 2002.

101. Sarid, D. *Scanning Force Microscopy,* Oxford University Press, Inc., **1991**.

102. Ding, K. *Dissertation*, University of Mainz, **2006**.

103. The image has been reprinted from: *http://www.npl.co.uk/upload//img_400/S2.2.1_-_afm_contact.jpg*

104. Chrambach, A. *The Practice of Quantitative Gel Electrophoresis,* VCH, **1985**.

105. The image has been reprinted from: *http://www.cbs.dtu.dk/staff/dave/roanoke/fig5_33.jpg*

106. Hunter, R. J. *Zeta Potential in Colloid Science*, Academic Press Inc., New York, **1981**.

107. Kohl, C.; Weil, T.; Qu, J. Q.; Müllen, K. *Chem.Eur. J.* **2004**, *10*, 5297–5310.

108. Abdalla, M. A.; Bayer, J.; Rädler, J. O.; Müllen, K. *Angew. Chem. Int. Ed.* **2004**, *43*, 3967–3970.

109. Wang, D.; Wang, J.; Moses, D.; Bazan, G. C.; Heeger, A. J. *Langmuir* **2001**, *17*, 1262–1266. (36)

110. Fan, C. H.; Hirasa, T.; Plaxco, K. W.; Heeger, A. J. *Langmuir* **2003**, *19*, 3554–3556.

111. Wang, D.; Wang, J.; Moses, D.; Bazan, G. C.; Heeger, A. J.; Park, J. H.; Park, Y. W. *Synth. Met.* **2001**, *119*, 587–588.

112. Fromherz, P.; Rieger, B. *J. Am. Chem. Soc.* **1986**, *108*, 5361–5362.

113. Langowski, J. *Biophys. Chem.* **1987**, *27*, 263–271.

114. Schmitz, K. S.; Pecora, R. *Biopolymers* **1975**, *14*, 521–542.

115. Berne, B. J.; Pecora, R. *Dynamic Light Scattering*; John Wiley & Sons, Inc.: Canada, **1976**, Chapter 7.

116. Arutyunyan, A. V.; Ivanova, M. A.; Kurlyand, D. I.; Noskin, V. A. *Molecular Biology* **1993**, *27*, 705-712.

117. Dawson, J. R.; Harpst, J. A. *Biopolymers* **1971**, *10*, 2499–2508.

118. Becker, A.; Köhler, W.; Müller, B. *Ber. Bunsen-Ges. Phys. Chem.* **1995**, *99*, 600.

119. Fishman, D. M; Patterson, G. D. *Biopolymers* **1996**, *38*, 535–552.

120. Störkle, D.; Duschner, S.; Heimann, N.; Maskos, M.; Schmidt, M. *Macromolecules* **2007**, *40*, 7998–8006.

121. Xie, D. H.; Xu, K.; Bai, R. K.; Zhang, G. Z. *J. Phys. Chem. B* **2007**, *111*, 778-781.

122. Bantle, S.; Schmidt, M.; Burchard, W.; *Macromolecules*, **1982**, *15*, 1604-1609.

123. Zhang, L. F.; Liang, Y.; Meng, L. Z.; Wang, C. *Polym. Adv. Technol.* **2009**, *20*, 410–415.

124. Balagurumoorthy, P.; Adelstein, S. J.; Kassis, A. I. *Analytical Biochemistry* **2008**, *381*, 172–174.

125. Seils, J.; Dorfmüller, T. H. *Biopolymers* **1991**, *31*, 813–825.

126. Sorlie, S. S.; Pecora, R. *Macromolecules* **1988,** 21, 1437-1449.

127. Vinogradova, O. L.; Lebedeva, O. V.; Vasilev, K.; Gong, H. F.; Garcia-Turiel, J.; Kim, B. S. *Biomacromolecules* **2005**, *6*, 1495–1502.

128. Dubrovin, E. V.; Staritsyn, S. N.; Yakovenko, S. A.; Yaminsky, I. V. *Biomacromolecules* **2007**, *8*, 2258–2261.

129. Maurstad, G.; Stokke, B. T. *Biopolymers* **2004**, *74*, 199–213.

130. Tanigawa, M.; Okada, T. *Anal. Chim. Acta* **1998**, *365*, 19–25.

131. Ding, K.; Alemdaroglu, F. E.; Börsch, M.; Berger, R.; Herrmann, A. *Angew. Chem. Int. Ed.* **2007**, *46*, 1172-1175.

132. Pope, L. H.; Davies, M. C.; Laughton, C. A.; Roberts, C. J.; Tendler, S. J. B.; Williams, P. M. *Journal of Microscopy* **2000**, *199*, 68-78.

133. Liu, Z.; Li, Z.; Zhou, H.; Wei, G.; Song, Y.; Wang, L. *Microsc. Res. Tech.* **2005**, *66*, 179–185.

134. Liu, Z.; Li, Z.; Zhou, H.; Wei, G.; Song, Y.; Wang, L. *J. Microsc.* **2005**, *218*, 233–239.

135. Bezanilla, M.; Manne, S.; Laney, D. E.; Lyubchenko, Y. L.; Hansma, H. G. *Langmuir* **1995**, *11*, 655–659.

136. Fang, Y.; Hoh, J. H. *Nucl. Acid Res.* **1998**, *26*, 588–593.

137. Besteman, K.; Eijk, K. V.; Vilfan, I. D.; Ziese, U.; Lemay, S. G. *Biopolymers* **2007**, *87*, 141–148.

138. B-DNA is the biologically predominated DNA form in nature with strand diameter of 2 nm

139. Rippe, K.; Mücke, N.; Langowski, J. *Nucl. Acid Res.* **1997**, *25*, 1736–1744.

140. Zhang, C.; Su, M.; He, Y.; Zhao, X.; Fang, P.; Ribbe, A. E.; Jiang, W.; Mao, C. *PNAS* **2008**, *105*, 10665–10669.

141. Safak, M.; Alemdaroglu, F. E.; Li, Y.; Ergen, E.; Herrmann A. *Adv. Mater.* **2007**, *19*, 1499–1505.

142. Ma, C. L.; Bloomfield, V. A. *Biopolymers* **1995**, *35*, 211–216.

143. Hansma, H. G.; Golan, R.; Hsieh, W.; Lollo, C. P.; Mullen-Ley, P.; Kwoh, D. *Nucl. Acid Res.* **1998**, *26*, 2481–2487.

144. Maurstad, G.; Danielsen, S.; Stokke, B. T. *Biomacromolecules* **2007**, *8*, 1124-1130.

145. Maret, G.; Weill, G. *Biopolymers*, **1983**, *22*, 2727-2744.

146. Thünemann, A. F.; Müller, M.; Dautzenberg, H.; Joanny, J. F. O.; Löwen, H. *Adv. Polym. Sci.* **2004**, *166*, 113–171.

147. Schwarz, G.; Klose, S.; Balthasar, W. *Eur. J. Biochem.* **1970**, *12*, 454–460.

148. Horn, D. *Prog. Colloid Polym. Sci.* **1978**, *65*, 251–264.

149. Yamakawa, N.; Ishikawa, Y.; Uno, T. *Chem. Pharm. Bull.* **2001**, *49*, 1531–1540.

150. Pasternack, R. F.; Garrity, P.; Ehrlich, B.; Davis, C. B.; Gibbs, E. J.; Orloff, G.; Giartosio, A.; Turano, C. *Nucl. Acid Res.* **1986**, *14*, 5919–5931.

151. Huang, C. Z.; Li, K. A.; Tong, S. Y. *Anal. Chem.* **1996**, *68*, 2259–2263.

152. Takatoh, C.; Matsumoto, T.; Kawai, T.; Saitoh, T.; Takeda, K. *Chem. Lett.* **2006**, *35*, 88–89.

153. An, W. T.; Guo, X. L.; Shuang, S. M.; Dong, C. *J. Photochem. Photobiol., A* **2005**, *173*, 36–41.

154. Qiu, W. G.; Li, Z. F.; Bai, G. M.; Meng, S. N.; Dai, H. X.; He, H. *Spectrochimica Acta Part A* **2007**, *68*, 1164-1169.

155. Jian T.; Anastasiadis S. H.; Semenov A. N.; Fytas G.; Adachi K.; Kotaka T. *Macromolecules* **1994**, *27*, 4762-4773.

156. Lai, G. H.; Coridan, R.; Zribi, O. V.; Golestanian, R.; Wong, G. C. L. *Phys. Rev. Lett.* **2007**, *98*, 187802.

157. Tang, J. X.; Wong, S.; Tran, P. T.; Janmey, P. A. *Ber. Bunsen-Ges. Phys. Chem.* **1996**, *100*, 796–806.

158. Lyubartsev, A. P.; Tang, J. X.; Janmey, P. A.; Nordenskiöld, L. *Phys. Rev. Lett.* **1998**, *81*, 5465–5468.

159. Bloomfield, V. A. *Biopolymers* **1991**, *31*, 1471–1481.

160. Henle, M. L.; Pincus, P. A. *Phys. Rev. E: Stat., Nonlinear, Soft Matter Phys.* **2005**, *71*, 060801.

161. Deserno, M. *Eur. Phys. J. E* **2001**, *6*, 163–168.

162. Sayar, M.; Holm, C. *Europhys. Lett.* **2007**, *77*, 16001.

163. Förster, S.; Hermsdorf, N.; Leube, W.; Schnablegger, H.; Regenbrecht, M.; Akari, S. *J. Phys. Chem. B* **1999**, *103*, 6657–6668.

164. Newton, G. L.; Ly, A.; Tran, N. Q.; Ward, J. F.; Milligan, J. R. *Int. J. Radiat. Biol.* **2004**, *80*, 643–651.

165. Voet, D.; Voet, J. G. *Biochemistry (3rd Edition),* John Wiley & Sons, Inc., **2004**.

166. Chou, P. Y.; Scheraga, H. A. *Biopolymers* **1971,** *10*, 657-680.

167. Koene, R. S.; Mandel, M. *Macromolecules* **1983**, *16*, 220–227.

168. Koene, R. S.; Nicolai, T.; Mandel, M. *Macromolecules* **1983**, *16*, 227–231.

169. Zhao, F.; Du, Y. K.; Yang, P.; Tang, J.; Li, X. C. *Colloid Polym. Sci.* **2005**, *283*, 1361–1365.

170. Minko, S.; Kiriy, A.; Gorodyska, G.; Stamm, M. *J. Am. Chem. Soc.* **2002**, *124*, 3218.

171. Sato, H; Nakajima, A. *Colloid and Polymer Sci.* **1974**, *252*, 294-297.

172. Regenbrecht, M.; Akari, S.; Förster, S.; Möhwald, H. *Surf. Interface Anal.* **1999**, *27*, 418.

173. Yang, J. C.; Jablonsky, M. J.; Mays, J. W. *Polymer* **2002**, *43*, 5125–5132.

174. Roddick-Lanzilotta, A. D.; McQuillan, A. J. *Journal of Colloid and Interface Science* **1999**, *217*, 194-202.

175. Susi, H.; Timasheff, N.; Stevens, L. *The Journal of Biological Chemistry* **1967**, *242*, 5460-5466.

176. Eker, F.; Griebenow, K.; Cao, X. L.; Nafie, L. A.; Schweitzer-Stennert, R. *Biochemistry* **2004**, *4*3, 613-621.

177. Eker, F.; Cao, X. L.; Nafie, L.; Schweitzer-Stenner, R. *J. Am. Chem. Soc.* **2002**, *124*, 14330-14341.

178. Bellamy, L. J. *The Infrared Spectra of Complex Molecules (2nd Edition)*, Chapman and Hall, **1980**.

179. Jeffrey, G. A.; Saenger, W. *Hydrogen Bonding in Biological Strucutres,* Springer-Verlag, **1991**.

180. Ou, Z. Y.; Muthukuma, M. *The Journal of Chemical Physics* **2006**, *124*, 154902.

181. Sinn, C. G.; Dimova, R.; Antonietti, M. *Macromolecules* **2004**, *37*, 3444–3450.

182. Rialdi, G.; Hermans, J. *J. Am. Chem. Soc.* **1966**, *88*, 5719-5720.

183. Scholtz, J. M.; Marqusee, S.; Baldwin, R. L.; York, E. J.; Stewart, J. M.; Santoro, M. Bolen, D. W. *Proc. Natl. Acad. Sci.* **1991**, *88*, 2854-2858.

184. Matulis, D.; Rouzina, I.; Bloomfield V. A. *J. Mol. Biol.* **2000**, *296,* 1053-1063.

185. Limanskaya, L. A.; Limanskii, A. P. *Russian Journal of Bioorganic Chemistry* **2006**, *32*, 444-459.

186. Lyubchenko, Y. L.; Shlyakhtenko, L. S. *Proc. Natl. Acad. Sci. USA* **1997**, *94*, 496-501.

187. Pastre, D.; Hamon, L.; Landousy, F.; Sorel, I.; David, M. O.; Zozime, A.; Cam, E. L.; Pietrement, O. *Langmuir* **2006**, *22*, 6651-6660.

188. Klinov, D. V.; Martynkina, L. P.; Yurchenko, V. Y.; Demin, V. V.; Streltsov, S. A.; Gerasimov, Y. A.; Vengerov, Y. Y. *Russian Journal of Bioorganic Chemistry* **2003**, *29*, 363-367.

189. The image has been reprinted from: Willerich, I.; Ritter, H.; Gröhn, F. *J. Phys. Chem. B* **2009**, *113*, 3339-3354.

190. Verilhac, J. M.; LeBlevennec, G.; Djurado, D.; Rieutord, F.; Chouiki, M.; Travers, J. P.; Pron, A. *Synthetic Metals* **2006**, *156*, 815-823.

191. Filippini, P.; Rainaldi, G.; Ferrante, A.; Mecheri, B.; Gabrielli, G.; Bombace, M.; Indovina, P. L.; Santini, M. T. *Journal of Biomedical Materials Research* **2001**, *55,* 338-349.

192. Su, P. G.; Cheng, K. H. *Sensors and Actuators* **2009**, *137*, 555-560.